

# **INAUGURAL DISSERTATION**

zur

**Erlangung der Doktorwürde**

der

**Naturwissenschaftlich-Mathematischen**

**Gesamtfakultät**

**der Ruprecht-Karls-Universität**

**Heidelberg**

**vorgelegt von**

**Michael Walther, MSc**

aus

**Bad Soden am Taunus**

**Tag der mündlichen Prüfung: 18.10.2018**



**Doctoral Thesis**

**Monitoring Thermal Evolution in the  
Intergalactic Medium over 12 Billion  
Years**

Michael WALTHER

October 2018

Universität Heidelberg

Supervisor & First Referee: Prof. Dr. Joseph F. HENNAWI

Second Referee: Prof. Dr. Björn M. SCHÄFER



## Abstract

The thermal state of the intergalactic medium (IGM) is an important probe of physical properties for the bulk of gas in the universe. Here, we perform a new measurement of the thermal state for redshift  $z \lesssim 5.4$  covering 12 billion years from the endstage of reionization to the present day. For this purpose we measure the Lyman- $\alpha$  forest flux power spectrum based on high resolution quasar spectra from different ground- and space-based spectrographs, combine this analysis with archival measurements of percent level precision, analyze hydrodynamical simulations, use powerful statistical techniques for interpolation, and perform Bayesian inference via Markov chain monte carlo. We observe a rise in the temperature at mean density from 6000 K at  $z = 5.4$  towards 14 000 K at  $z = 3.4$  followed by a cooldown phase reaching 6000 K at  $z = 0.03$ . This evolution provides conclusive evidence for photoionization heating due to reionization of He II, as well as the subsequent cooling of the IGM due to an expanding universe in concordance with model predictions. The agreement with previous measurements is good as well, but our analysis supercedes those by accounting for additional parameters that we marginalize over, and by the vast cosmological timespan our measurement spans. At the highest redshifts  $z > 5$  we infer lower temperatures than expected from the standard picture of IGM heating allowing leaving little room for additional smoothing due to warm dark matter free streaming. Additionally, our measurement for  $z < 0.5$  allows additional constraints on the ultraviolet background in contradiction to previous claims of a UV underproduction crisis.

## Zusammenfassung

Die thermische Entwicklung des intergalaktischen Mediums (IGM) ist eine wichtige Möglichkeit physikalische Eigenschaften vom Großteil des Gases im Universum zu bestimmen. In dieser Arbeit führen wir eine Messung der thermischen Entwicklung über 12 Milliarden Jahre durch, welche die gesamte Zeitspanne von Rotverschiebung  $z \sim 5.4$  in der Endphase des Zeitalters der Reionisation bis heute umfasst. Zu diesem Zweck bestimmen wir das Modenspektrum des Flusses im Lyman- $\alpha$  Wald mithilfe existierender spektroskopischer Daten diverser weltraum- und bodengebundener Instrumente, vereinigen dieses mit prozentgenauen Messungen aus dem Archiv, analysieren hydrodynamische Simulationen, nutzen mächtige statistische Werkzeuge zur Interpolation, und ermitteln physikalische Parameter mittels Markov-Ketten-Monte-Carlo Verfahren. Wir beobachten einen Anstieg der Temperatur bei mittlerer Dichte  $T_0$  von 6000 K bei  $z = 5.4$  zu 14 000 K bei  $z = 3.4$ . Darauf folgt eine Abkühlungsphase, sodass  $T_0$  bei  $z = 0.03$  einen Wert von 6000 K erreicht. Aus dieser Entwicklung lässt sich ein klarer Beleg für die Erwärmung des IGMs durch Photoionisation während der Reionisation von He II. Die Abkühlung erfolgt aufgrund der Expansion des Universums und ist im Einklang mit Modellvorhersagen. Die Übereinstimmung mit vorherigen Messungen der thermischen Entwicklung ist ebenfalls gut, unsere Messung geht aber insbesondere durch Berücksichtigung weiterer Parameter und Marginalisierung über selbige sowie durch den erweiterten abgedeckten Zeitraum darüber hinaus. Für die höchsten Rotverschiebungen  $z > 5$  messen wir niedrigere Temperaturen als im üblichen Modell für das IGM erwartet werden. Dadurch bleibt wenig Platz für die weitere Verwischung von Strukturen, z.B. durch warme Dunkle Materie. Schließlich ermöglicht unsere Messung bei kleinen Rotverschiebungen  $z < 0.5$  Rückschlüsse auf den metagalaktischen UV Hintergrund. Dies widerspricht früheren Messungen, welche einen Mangel an UV Photonen schlussfolgerten und ist im Einklang mit den neuesten Ergebnissen, welche diesen Mangel widerlegen.

## Eidesstattliche Versicherung

Bei der vorliegenden Dissertation handelt es sich um meine eigenständig erbrachte Leistung.

Ich habe nur die angegebenen Quellen und Hilfsmittel benutzt und mich keiner unzulässigen Hilfe Dritter bedient. Insbesondere habe ich wörtlich oder sinngemäß aus anderen Werken übernommene Inhalte als solche kenntlich gemacht.

Die Arbeit oder Teile davon habe ich bislang nicht an einer Hochschule des In- oder Auslands als Bestandteil einer Prüfungs- oder Qualifikationsleistung vorgelegt.

Die Richtigkeit der vorstehenden Erklärungen bestätige ich.

Die Bedeutung der eidesstattlichen Versicherung und die strafrechtlichen Folgen einer unrichtigen oder unvollständigen eidesstattlichen Versicherung sind mir bekannt.

Ich versichere an Eides statt, dass ich nach bestem Wissen die reine Wahrheit erklärt und nichts verschwiegen habe.

.....

Ort und Datum

.....

Unterschrift



# Preface

The present thesis contains the bulk of the work I conducted for my PhD project at both the Max-Planck-Institute for Astronomy and the University of California, Santa Barbara which was supervised by Prof. Joseph F. Hennawi starting 2012.

The scientific goal of the project is to perform a measurement of thermal evolution in the IGM covering the time from the epoch of reionization to the present. The original motivation for this was that, although many measurements had been performed in the past, at the start of the project those results have been strongly discrepant with each other, resulting in claims for the need of non-standard sources of IGM heating to explain thermal measurements. But in the meantime there had been significant progress concerning both the size of datasets for these kinds of analyses available in the archives as well as on the accuracy of numerical simulations due to the increase in computational resources.

The general picture for thermal evolution of the IGM in the timeframe analyzed in this work is a period of heat injection due to He II reionization followed by a cooling trend dominated by the expansion of the Universe. While the detection of the heating signature has been claimed before, the latter has never been conclusively observed. Coincidentally, this timeframe includes the peak of galaxy and quasar formation at  $z \sim 2$  and measurements of cosmological parameters based on spectroscopic surveys of the Lyman Alpha ( $\text{Ly}\alpha$ ) forest fall in this range.

The project is divided into three parts. First, we measure the  $\text{Ly}\alpha$  forest flux power spectrum at redshifts  $1.8 \leq z \leq 3.4$ . This statistical property is sensitive on the thermal state of the IGM as well as on e.g. the nature of dark matter, or the mass of neutrinos

## *Preface*

and thus is of general interest independent of our conclusions on thermal evolution. We discuss the most important properties of the Ly $\alpha$  forest regarding this work in chapter 2. In chapter 3 we measure the power spectrum from archival high-resolution quasar spectra. While this has in principle been done before, we used a significantly larger dataset than any previous study based on high resolution data. The main challenges for this measurement have been discrepancies with existing data based on large scale structure surveys delivering two percent precision. These discrepancies were tracked down to at least partly originate in contaminations inside the spectra due to e.g. metal absorption lines, which led us to mask large parts of the data and develop a full forward modeling pipeline for our measurement. In this part we also develop a Bayesian inference pipeline, in principle allowing to measure the thermal state of the IGM. However, during the project we figured out that the accuracy of the numerical simulations we used at the time was not sufficient for the task.

In the second part, we performed a Bayesian measurement of thermal evolution for  $1.8 \leq z \leq 5.4$  (chapter 4). For this purpose, we combined our newly measured power spectrum with recent measurements of the same quantity performed by different groups at different redshifts and with different instruments. We switched from a relatively cheap simulational approach based on dark matter simulations to using grids of computationally expensive hydrodynamical simulations. The high computation costs for those models also required running less models than before and tuning our inference pipeline to handle this.

Finally, in the last six months of this project, we analyzed archival datasets at later cosmic times (chapter 5). These data have to be taken with space based UV spectrographs, which required additional treatment of peculiarities of the Hubble space telescope. However, due to those complications precise thermal state measurements at these times have never been performed before. These new measurements increase our baseline in cosmic time from  $\sim 3$  Gyr to  $> 12$  Gyr allowing to test if models of the IGM still agree with the data after the peak of Galaxy formation.

The work included in chapter 3 is adapted from a published paper of mine (Walther et

al., 2018a). The thermal evolution measurement in chapter 4 is adapted from a paper that was recently submitted to ApJ as Walther et al. (2018c). The low redshift measurement in chapter 5 was conducted in strong collaboration with Vikram Khaire, part of this work (the power spectrum measurement and a preliminary analysis of the ultraviolet background) has been submitted as Khaire, Walther, et al. (2018). The thermal evolution constraint (together with a better measurement of the UV background) is planned to be submitted as Walther et al. (2018b) after inclusion of further redshifts from this sample. All contributions to the modeling of the power spectrum including the characterization of the window function for these works are my own work. The data preparation was performed mostly by Vikram Khaire, who also performed the power spectrum measurement using an updated version of the analysis pipeline we developed for the high-redshift analysis.



# Contents

<b>Preface</b>	<b>i</b>
<b>1. Introduction</b>	<b>1</b>
1.1. The Current Model of Cosmological Structure Formation . . . . .	1
1.2. The Epoch of Reionization . . . . .	5
1.3. The Thermal State of the IGM . . . . .	7
<b>2. The Ly<math>\alpha</math> Forest as a Cosmological and Astrophysical Tool</b>	<b>11</b>
2.1. What is the Ly $\alpha$ Forest? . . . . .	11
2.2. Observability and Datasets . . . . .	14
2.3. The Ly $\alpha$ Forest Flux Power Spectrum . . . . .	15
2.4. Connection to the Thermal State of the IGM . . . . .	16
2.5. Constraining the Thermal State using Other Statistics of the Ly $\alpha$ Forest Flux . . . . .	22
<b>3. A New Measurement of the IGM Power Spectrum</b>	<b>25</b>
3.1. High-Resolution Quasar Dataset . . . . .	25
3.1.1. Dataset . . . . .	26
3.1.2. Spectral Masking Procedure . . . . .	29
3.1.3. Mean Flux Regulation and Continuum Uncertainties . . . . .	34
3.2. Power Spectrum Measurement and Forward Modeling Procedure . . . . .	38
3.2.1. Measuring the Power Spectrum . . . . .	39
3.2.2. The Window Function Resulting from Masking . . . . .	40

*Contents*

3.2.3.	Simulations and Mock Spectra . . . . .	41
3.2.4.	Forward Modeling Approach . . . . .	43
3.2.5.	Covariance Matrix Estimation . . . . .	44
3.2.6.	Fast Emulation of Model Power Spectra . . . . .	47
3.2.7.	Parameter Exploration . . . . .	48
3.2.8.	The Raw Power Spectrum and Window Function Correction . .	50
3.3.	A New Power Spectrum Measurement . . . . .	52
3.3.1.	The Final Power Spectrum Measurement and the Effect of Metals on the Data . . . . .	53
3.3.2.	Comparison to Previous Low and Medium Resolution Measure- ments . . . . .	55
3.3.3.	Comparison to Previous High-Resolution Measurements . . . .	61
3.4.	Summary . . . . .	63
<b>4.</b>	<b>A New Measurement of IGM Thermal Evolution at <math>1.8 &lt; z &lt; 5.4</math></b>	<b>67</b>
4.1.	Power Spectrum Datasets for Studying IGM Thermal Evolution . . . . .	68
4.2.	The THERMAL Suite of Hydrodynamical Simulations . . . . .	70
4.3.	Measuring the Thermal State of the IGM . . . . .	76
4.3.1.	Forward Modeling . . . . .	76
4.3.2.	Emulation of the Power Spectrum . . . . .	77
4.3.3.	Inference . . . . .	80
4.3.4.	Parameters and Priors . . . . .	81
4.4.	Thermal Evolution of the IGM . . . . .	85
4.4.1.	Measurements and Degeneracies . . . . .	85
4.4.2.	Analyzing the Discrepancies in $\gamma$ and $\bar{F}$ . . . . .	90
4.4.3.	Measuring Thermal Evolution in the IGM using a Gaussian Prior on the Mean Transmission . . . . .	95
4.4.4.	Comparison to Previous Measurements . . . . .	100

4.4.5. Comparing to Thermal Evolution Models for Different He II Reionization Scenarios . . . . .	105
4.5. Systematic Effects on the Measured Thermal Evolution . . . . .	109
4.6. Summary . . . . .	114
<b>5. Extending Thermal Evolution Measurements to Low Redshifts</b>	<b>117</b>
5.1. Dataset . . . . .	118
5.2. Adjustments in Methodology due to COS Peculiarities . . . . .	121
5.3. Power Spectrum Measurement . . . . .	123
5.4. Measuring the Thermal State at $z < 0.5$ . . . . .	125
5.4.1. Changes in our Measurement Approach Compared to the High Redshift Analysis . . . . .	125
5.4.2. Thermal Evolution at Low Redshifts . . . . .	129
5.4.3. Constraints on the Low Redshift UV Background . . . . .	131
5.5. Summary . . . . .	134
<b>6. Conclusions and Outlook</b>	<b>135</b>
<b>Appendix</b>	<b>139</b>
A. Impacts of seeing on power spectrum measurements . . . . .	139
B. Slit resolution of the X-SHOOTER spectrograph . . . . .	140
C. Normalization Conventions for the Power Spectrum . . . . .	142
D. Data Products for the Power Spectrum Measurement . . . . .	143
E. Tables of the Measured Thermal Evolutions . . . . .	144



# 1. Introduction

## 1.1. The Current Model of Cosmological Structure Formation

Our current model of cosmology and structure formation is based on the fundamental assumptions that the universe is (mostly) isotropic and homogeneous, and it's evolution is described by the framework of General Relativity. From these assumptions follows a simple theoretical description (Friedmann, 1922; Lemaître, 1927) of the Universe whose overall evolution is governed by the change in relative importance of different forms of energy as well as an overall expansion:

$$\frac{\dot{a}^2 + k}{a^2} = \frac{8\pi G\rho + \Lambda c^2}{3} \quad (1.1)$$

$$\frac{\ddot{a}}{a} = -\frac{4\pi G}{3} \left( \rho + \frac{3p}{c^2} \right) + \frac{\Lambda c^2}{3}, \quad (1.2)$$

with the scale factor  $a$ , the curvature parameter  $k$ , the gravitational constant  $G$ , the speed of light  $c$ , the density  $\rho$  and pressure  $p$ . Hubble (1929) first detected an expansion (i.e. increase of  $a$ ) by measuring the line-of-sight velocity of distant Galaxies  $v = zc$ , with the redshift  $z = \Delta\lambda/\lambda$  being connected to the scale factor as  $a = (1 + z)^{-1}$ , and compared them to their distances (measured from Cepheid variables). He then derived Hubble's law  $v = Hd$  and measured the Hubble parameter  $H^{1.1}$  (although with a value far away

---

<sup>1.1</sup>This is only true for small redshifts, i.e. recent times, as  $H$  is evolving with time and the concept of distance is not uniquely defined for larger redshifts (see e.g. Hogg, 1999).

## 1. Introduction

from the current constraints) allowing to obtain the distance of an object by measuring its redshift.

Since its foundations this theory proved tremendously successful. One of the most constraining probes of this model is the cosmic microwave background (CMB) radiation which was predicted by Alpher, & Herman (1948) and was first detected by Penzias, & Wilson (1965). More recent observations of it have delivered percent level constraints on cosmological parameters, deducing that the universe is flat (i.e.  $k = 0$  in eqn. (1.2)). While it is mostly homogeneous at early times, shows tiny but measurable inhomogeneities ( $\Delta T/T \sim 10^{-5}$ ) are theoretically expected and were measured with the Cosmic Background Explorer (COBE) (Smoot et al., 1992), the Wilkinson Microwave Anisotropy Probe (WMAP) (Bennett et al., 2013), and Planck (Planck Collaboration et al., 2018).

At the same time, observations of virial masses of clusters (Zwicky, 1933) and galaxy rotation curves (Rubin, & Ford, 1970) ultimately led to the postulation of collisionless cold dark matter with overwhelming evidence now coming from many other observations as well, e.g. lensing in clusters (e.g. the Bullet Cluster, Clowe et al., 2004), and from SNe we learned that its expansion needs to be accelerated (Schmidt et al., 1998; Riess et al., 1998; Perlmutter et al., 1998) demanding for some kind of Dark Energy<sup>1,2</sup>. Together these observations led to the current standard model of cosmology ( $\Lambda$ CDM), consisting of a cosmological constant  $\Lambda$  as well as cold dark matter (CDM). However, many questions are still not answered, e.g.: What is Dark Energy? What is Dark Matter? When and how did reionization happen? What is the mass of neutrinos?

The thermal evolution of the Universe is dictated its expansion history. At the beginning the Universe is seeded by quantum fluctuations that are amplified to macroscopic scales during inflation and provide the seeds for all structures we see today. After this process the Universe is still extremely hot and subsequently cools due to adiabatic expansion. During this cooling particles of decreasing mass freeze out of thermal equilibrium as their interaction rate becomes smaller than the expansion rate. This leads to the release of the cosmic neutrino background, Baryon nucleosynthesis, and finally the

---

<sup>1,2</sup>Note that both Dark Matter and Energy are required to explain the current CMB results as well.

### 1.1. *The Current Model of Cosmological Structure Formation*

”recombination” of atoms (which was delayed due to a large photon to baryon ratio) and release of the CMB photons (Alpher et al., 1948; Penzias, & Wilson, 1965; Planck Collaboration et al., 2018). At this point ( $z \sim 1100$ ) the temperature of the Universe had a temperature of  $\sim 3000$  K and was nearly 400 000 yr old.

After recombination, evolution is supposed to be relatively uneventful as the universe is cooling down further and there is (nearly) no interaction between matter and radiation, making these ”dark ages” essentially unobservable. In principle there are 21 cm emission and absorption by HI gas in this epoch (see Pritchard, & Loeb, 2012, for a review of the processes), but these have never been conclusively observed<sup>1,3</sup>.

But during the dark ages bound structures start to form due to gravitational collapse in overdense regions with the first galaxies being formed at  $z \gtrsim 11$ <sup>1,4</sup>. In these galaxies the first stars formed, finally providing new photons generated via nuclear fusion processes and thus starting the ”cosmic dawn”. Those photons then reionize the intergalactic medium (IGM) which we’ll discuss in more detail in § 1.2.

We show the evolution of baryonic structures after reionization based on our hydrodynamical simulations (which we discuss in § 4.2) in Figure 1.1. Here we see the concentration of gas forming a filamentary cosmic web which then collapse into halos at late times. Note that while baryonic structure follows dark matter, collisions will broaden its features relative to the extremely thin filaments formed by dark matter due to finite pressure support.

This work aims to put constraints on thermal evolution at the end and after this ”Epoch of Reionization”. We perform this measurement by studying the small scale structure of the IGM (see § 1.3) probed by the Ly $\alpha$  forest power spectrum (see chapter 2).

---

<sup>1,3</sup>While a detection of the global absorption feature has been claimed (Bowman et al., 2018), possibly this result is based on a fluke in the data analysis (Hills et al., 2018). Current measurements of the power spectrum of 21cm emission are performed by several groups (e.g. HERA, PAPER, LOFAR, MWA), but currently foreground emission dominates the measurements (see e.g. Ali et al., 2015; Kohn et al., 2018).

<sup>1,4</sup>The currently highest redshift galaxy observation was presented in Oesch et al. 2016, but the James Webb Space Telescope (JWST) is expected to find galaxies at earlier times, see e.g. Mason et al. 2015 for predictions

## 1. Introduction

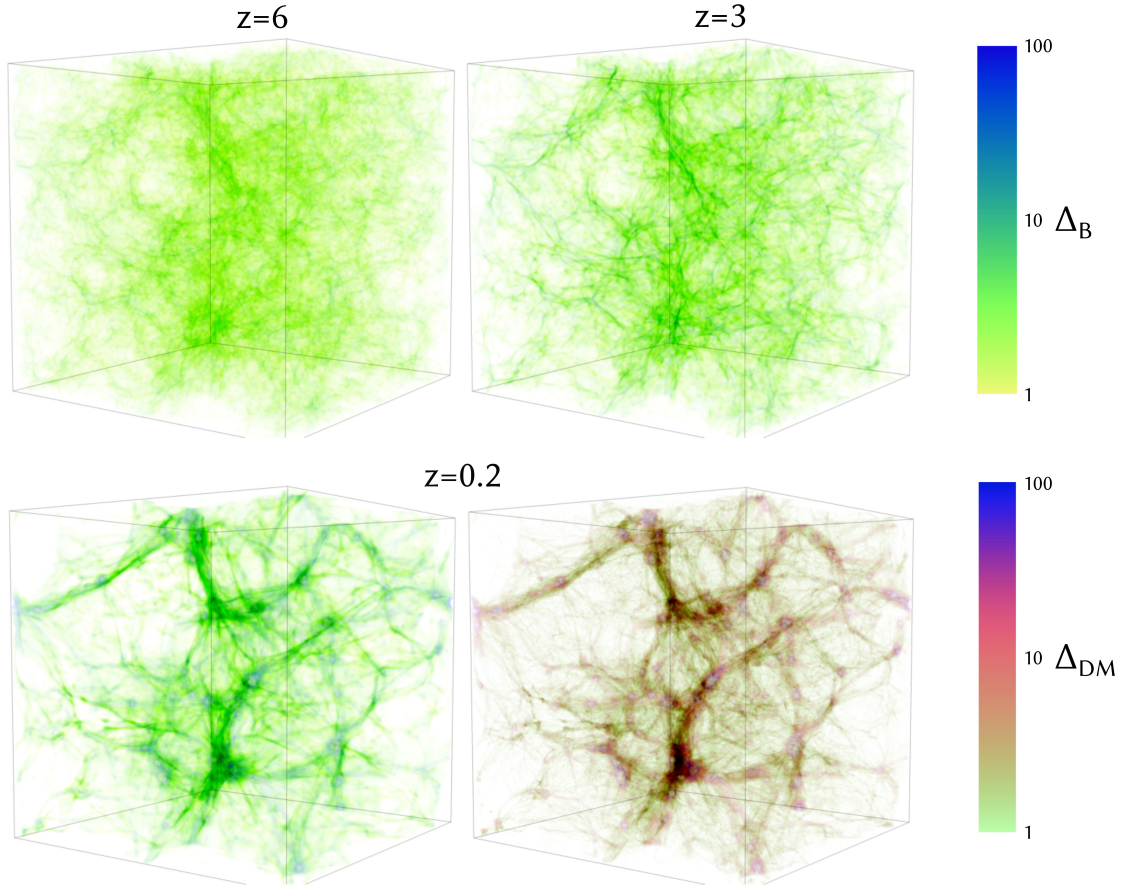


**Figure 1.1.:** Evolution of Baryonic structure from  $z = 6$  to  $z = 0.2$  (top boxes and bottom left). We can see that while most of the overdense gas (underdensities are colored in white) at  $z = 6$  is close to mean density and large parts of the volume are filled by this gas (light green color), until  $z = 3$  more and more gas moved to filaments showing overdensities of a few, and at  $z = 0.2$  some fraction of the gas mass is actually at halos with overdensities larger than 100. For  $z = 0.2$  we also show the distribution of dark matter (bottom right). Here we can see that baryons mostly follow the dark matter distribution, but the latter produces finer filamentary structures because it is collisionless (see Figure 2.3 for a rendering from the center of the box showing this more clearly). The side length of the box is  $20 h^{-1}$  Mpc.

## 1.2. The Epoch of Reionization

The Epoch of Reionization ends the dark ages as new sources of HI ionizing photons, i.e. photons with  $E > 13.6$  eV, emerge which ionize bubbles of HII around themselves (for general reviews about this epoch, see e.g. Barkana, & Loeb, 2001; Mesinger, 2016). These sources are typically expected to be stars inside the first galaxies (e.g. Robertson et al., 2013; Finkelstein et al., 2015; Oesch et al., 2014; Bouwens et al., 2015)<sup>1.5</sup>. As the ionized bubbles grow in time, they eventually overlap, thus filling the entire universe, and leave an almost completely ionized IGM behind.

Our currently strongest constraints of this process are coming from 2 sources. First, CMB photons are Thomson scattered inside an ionized medium both dampening and polarizing CMB fluctuations. The most recent constraints of these effects were obtained by the Planck Collaboration et al. (2018) and lead to  $z_{\text{reion},50} = 7.67 \pm 0.73$ <sup>1.6</sup>.

Additionally, as the fraction of neutral gas in the IGM increases it becomes less transparent for Ly $\alpha$  photons and eventually turns completely opaque (see chapter 2 for a more rigorous description). Measurements of the Ly $\alpha$  forest optical depth put this time close to  $z = 6$  (Fan et al., 2006a; Becker et al., 2015a; Bosman et al., 2018; Eilers et al., 2018) revealing that reionization has to end by  $z \sim 6$ . Recently, measurements based on damping wings of the IGM in spectra of the highest redshift quasars (Bañados et al., 2018; Davies et al., 2018a) and based on the equivalent width distribution of Ly $\alpha$  emission in Lyman break galaxies (Mason et al., 2018) also revealed that the IGM at  $z \sim 7$  has to be significantly neutral.

As the photons reionizing the universe come from individual sources, the process of reionization is intrinsically inhomogeneous (see e.g. Becker et al., 2015b; Davies, & Furlanetto, 2016; D’Aloisio et al., 2016, for evidence of this). Fully simulating the formation of ionized bubbles in the IGM requires expensive simulations as radiative

---

<sup>1.5</sup>Note that some groups claim that quasars provide a significant or even dominant (Giallongo et al., 2015; Madau, & Haardt, 2015) contribution to this (but see Onoue et al., 2017; Parsa et al., 2018, for strong arguments against the measurements resulting in this scenario)

<sup>1.6</sup> $z_{\text{reion},50}$  is the redshift at which  $x_{\text{HI}} = 0.50$ .

## 1. Introduction

transfer (RT) needs to be performed on Baryons that evolve due to hydrodynamics (see, e.g. Gnedin, 2014; Ocvirk et al., 2016, for examples)<sup>1.7</sup>. After reionization is complete photons can travel freely, leading to a nearly homogeneous radiation field called the metagalactic ultraviolet background (UVB) (Haardt, & Madau, 2012). The ionization state of the IGM<sup>1.8</sup> can be fully described by photoionization equilibrium in this homogeneous background, enormously simplifying the modeling (Haardt, & Madau, 2012; Oñorbe et al., 2017b; Khaire, & Srianand, 2018; Puchwein et al., 2018).

However, this is not the whole story and while by  $z = 6$  most of the Hydrogen gas has become ionized, Helium is not fully ionized, yet. Stripping the first electron of an Helium atom, i.e. forming He II, has an ionization threshold of 24.6 eV. Photons of this energy are provided by the same sources reionizing H I. However, further ionizing He II requires 54.4 eV photons which are not produced in most stars (Stanway et al., 2016; Topping, & Shull, 2015). Therefore this process is delayed until  $z \sim 4$  when luminous quasars which provide the required hard photons become abundant enough (Furlanetto, & Oh, 2008; McQuinn et al., 2009). Indeed, observations of the He II Ly $\alpha$  forest indicate He II had to be fully reionized by  $z = 2.7$  (Worseck et al., 2011) with measurements of ionized patches in the IGM existing at redshifts as high as  $z = 3.8$  (Worseck et al., 2016; 2018). However, the limited number of observational constraints due to the observational challenges of working in the ultraviolet (UV)<sup>1.9</sup> imply that the exact timing remains largely uncertain.

---

<sup>1.7</sup>This is due to the different timescales of the problems as the RT needs to resolve the time between scatterings of photons and the hydrodynamics need to resolve movements inside the gas. Note that there are ways to simplify the treatment of radiation, e.g. see Mesinger, & Furlanetto (2007), and the option to not fully self-consistently treat both effects, i.e. ignoring the evolution of the IGM when performing the RT thus allowing to post-process hydrodynamical simulations.

<sup>1.8</sup>This is only true far away from any strong source of radiation, e.g. luminous quasars, that would dominate the number of ionizing photons locally, leading to the so-called proximity effect

<sup>1.9</sup>The He II Ly $\alpha$  transition falls at  $\lambda_{\text{rest}} \approx 304 \text{ \AA}$ , i.e. is still in the far UV even at  $z = 4$ . Direct observations of He II at higher redshifts therefore have to wait until the next generation of UV space telescopes. Those are currently only in their concept stage and will likely not be available within the next two decades, e.g. the Large Ultraviolet/Optical/Infrared Surveyor (LUVOIR) (Roberge, & Moustakas, 2018) currently proposes a launch around the late 2030s.

However, while it is observationally tricky to obtain direct higher redshift constraints on He II reionization, we can indirectly constrain it via its imprint on the thermal state of the IGM.

### 1.3. The Thermal State of the IGM

In the standard picture of thermal evolution, cold IGM gas (few K) is strongly heated during H I and He I reionization (by few times 10 000 K), subsequently cools and then experiences additional heating during He II reionization (McQuinn et al., 2009; Compostella et al., 2013; Puchwein et al., 2015; Greig et al., 2015; Upton Sanderbeck et al., 2016; McQuinn, & Upton Sanderbeck, 2016; Oñorbe et al., 2017b; Puchwein et al., 2018). The combined effects of photoionization heating (and in principle also shock heating which is subdominant for most of the redshifts of interest), Compton cooling, and adiabatic cooling due to the expansion of the universe lead to a tight power law temperature density relation (TDR) for most of the IGM gas (Hui, & Gnedin, 1997; Puchwein et al., 2015; McQuinn, & Upton Sanderbeck, 2016) about  $\Delta z \approx 1-2$  after the impulsive heating from a reionization event:

$$T(\Delta) = T_0 \Delta^{\gamma-1}, \quad (1.3)$$

where  $\Delta = \rho/\bar{\rho}$  is the overdensity,  $T_0$  is the temperature at mean density  $T_0$ , and the index  $\gamma$  is expected to asymptotically approach  $\sim 1.65$ .

During reionization events this index is expected to be shallower due to the additional photoionization heating which may also result in a large scatter and a more complicated density dependence (Compostella et al., 2013; McQuinn, & Upton Sanderbeck, 2016). This would be mostly caused by reionization not occurring uniformly, but being intrinsically patchy and therefore leading to significant fluctuations in the UVB (Davies, & Furlanetto, 2016; Suarez, & Pontzen, 2017) as well as temperatures (D'Aloisio et al., 2015). Hydrodynamical simulations show that within several hundred Myr the gas relaxes to the tight power law relation of eqn. (1.3) with the exact thermal evolution solely depending on the shape of the UVB spectral energy distribution (SED).

## 1. Introduction

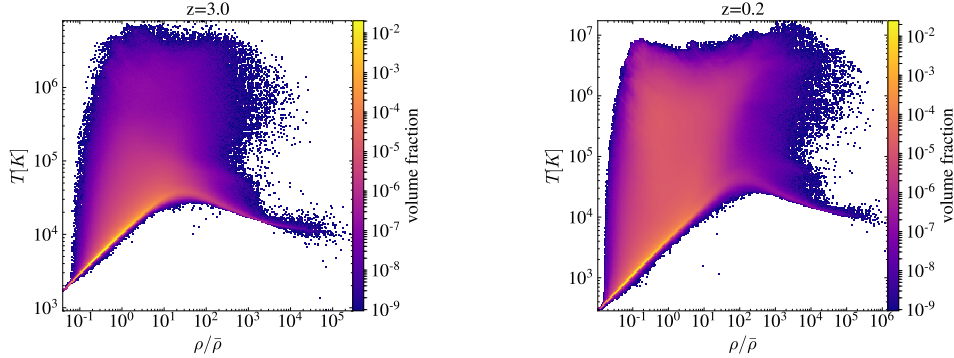


**Figure 1.2.:** The volume weighted TDR of the IGM at redshifts 3 (left) and 0.2 (right) from one of our simulations. The image shows a 2d histogram of  $T$  vs  $\rho$ . Note that the colorbar is logarithmic and the axis ranges are not matched between panels, i.e. the  $z = 0.2$  panel has a wider range in both directions. We can clearly see that most of the volume of the simulation follows a very tight power law TDR (bright yellow region) in both cases. Also note that the fraction of the gas in a hot shock heated state (WHIM) strongly increases from  $z = 3$  to  $z = 0.2$  (orange region in the upper left of the diagram). Finally, we can see that gas on the main power law relation has cooled down from  $z = 3$  to  $z = 0.2$ .

After reionization events the cooling terms are supposed to dominate over photoionization heating, resulting in a net cooling of intergalactic gas between and after the reionization phases which has so far not been conclusively observed (McQuinn, & Upton Sanderbeck, 2016). Unfortunately, there is currently no consensus about the thermal evolution of the IGM during and after He II reionization, although many measurements have been performed. Finally, at late times  $z \lesssim 1$  a significant fraction of the gas is also shock heated to high temperatures  $T > 1 \times 10^5$  K forming the so called Warm-Hot Intergalactic Medium (WHIM) (Cen, & Ostriker, 1999; Davé et al., 2001) and is expected to contain  $\sim 30\%$  of the total Baryon budget of the universe today<sup>1.10</sup> (Shull et al., 2012).

In Figure 1.2 we show the thermal state of the gas obtained in an hydrodynamical

<sup>1.10</sup>The problems in finding signatures for this component were dubbed the "missing baryon problem" which was recently claimed to be resolved through observations of the thermal Sunyaev-Zeldovich effect (de Graaff et al., 2017; Tanimura et al., 2017) as well as by direct observations of O VII in X-Ray quasar spectra (Nicastro et al., 2018)

### 1.3. *The Thermal State of the IGM*

simulation (see § 4.2 for details about the simulation). This simulation contained cooling via inverse Compton and expansion, as well as heating via photo- and collisional ionization in the IGM, but assumes homogeneous ionization and thus does not show the effects expected due to the patchiness of reionization. We show two different redshifts for comparison. At  $z = 3.0$  reionization of He II is about to finish, i.e. the gas in the IGM reaches its maximum temperature at around this time while  $z = 0.2$  is far after reionization and the IGM had about nine Gigayears of time to cool down. We can roughly subdivide this TDR into four different regimes with boundaries at  $T = 100\,000$  K and  $\rho = 100\bar{\rho}$ . While gas above the density cut is bound gas, coming from the hot halo or cold condensed gas phase (e.g. Davé et al., 2010), in this work we are most interested in the low-density gas forming the IGM. For both redshifts we can see that the photoionized low temperature, low density gas (the so called "diffuse IGM") is indeed dominated by a power law TDR as in eqn. (1.3). We note, that this power law component is cooling from  $T_0 \sim 10\,000$  K at  $z = 3$  to  $\sim 4000$  K at  $z = 0.2$  for the simulation shown. There is also a hot, low density component (the WHIM) visible at both redshifts due to shock heating which gets more prominent in the lower redshift. For the bulk of this work this component will be subdominant, and we thus neglect it. At the end of this thesis, however, we measure the thermal state of the low-redshift IGM and need to be careful regarding the WHIM.

In this work we put new constraints on the thermal state of the diffuse IGM from  $z = 5.4$  to  $z = 0.2$ . This component of IGM gas can be observed as the Ly $\alpha$  forest on distant background sources. In chapter 2 we introduce the statistical properties of the IGM that are important for the rest of this work. This is followed by a new high-resolution, high-precision measurement of the Ly $\alpha$  forest power spectrum at  $1.8 < z < 3.4$  in chapter 3. To find the imprint of heating and cooling on the IGM during and after He II reionization, we conduct a Bayesian analysis of thermal evolution at  $1.8 < z < 5.4$  taking into account degeneracies between the different thermal parameters in chapter 4. In chapter 5 we extend the measurements of the IGM thermal state to low redshifts to test if the predictions of a cooldown in the IGM holds over timescales of several billion years.

## *1. Introduction*

chapter 6 summarizes this work and gives an outlook for the future.

## 2. The Ly $\alpha$ Forest as a Cosmological and Astrophysical Tool

### 2.1. What is the Ly $\alpha$ Forest?

The so-called Ly $\alpha$  forest is a series of Ly $\alpha$  absorption lines, i.e. the  $n = 1 \rightarrow n = 2$  transition of the hydrogen atom<sup>2.1</sup>, which is typically observed blueward of the Ly $\alpha$  emission line at  $\lambda_{\text{rest}} = 1215.67 \text{ \AA}$  in high-redshift quasar spectra (where it has first been observed by Lynds 1971), but also in spectra of other distant sources, like e.g. gamma ray bursts (GRBs) (Selsing et al., 2018), background galaxies (Lee et al., 2014), or supernovae (Cooke et al., 2012). We show a spectrum of a quasar at  $z = 2.66$  in Figure 2.1. We highlight both the Ly $\alpha$  and Ly $\beta$  emission lines and can clearly see a dense structure of absorption lines bluewards of the Ly $\alpha$  emission, which is the Ly $\alpha$  forest.

The Ly $\alpha$  forest is formed by neutral gas in the mostly ionized intervening IGM along the quasar line-of-sight. As the universe expands, the source spectrum redshifts and thus the Ly $\alpha$  absorption line in the restframe of intervening gas falls on different positions of the source spectrum.<sup>2.2</sup> Even if a tiny fraction of the IGM  $x_{\text{HI}} \gtrsim 0.001$  were neutral, complete absorption of the spectrum by intervening gas would be expected. However, the existence of flux blueward of Ly $\alpha$  provides strong evidence that the IGM is highly

---

<sup>2.1</sup>The term is generally used for hydrogen like ions, i.e. ions with one electron such as He II which has this transition at  $\lambda = 304 \text{ \AA}$ . In this work we mean HI as long as the element is not stated explicitly.

<sup>2.2</sup>Note that the forest extends also beyond the Ly $\beta$  emission line, but is then superimposed on a forest of Ly $\beta$  absorption from higher redshift gas. The equivalent is true for higher order Lyman series lines.

## 2. The Ly $\alpha$ Forest as a Cosmological and Astrophysical Tool

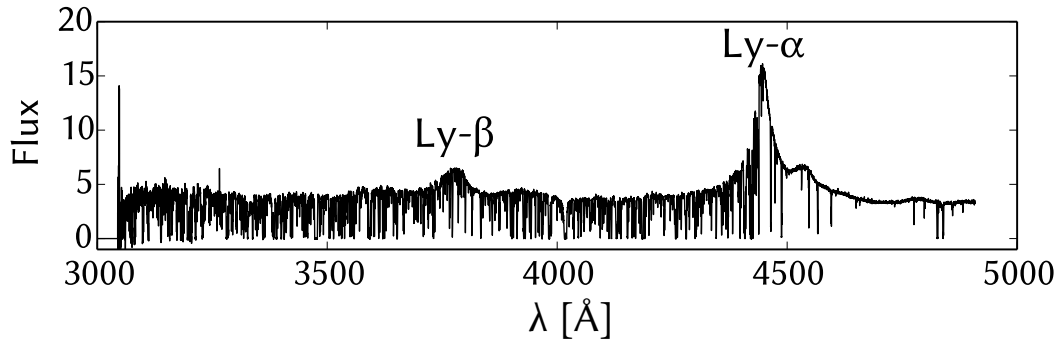


**Figure 2.1.:** Spectrum of the Quasar Q0453-423 at  $z = 2.66$  observed with the UVES spectrograph at the VLT. We can see the Ly $\alpha$  emission line at  $\lambda \sim 4450 \text{ \AA}$  and the Ly $\beta$  emission line at  $\lambda \sim 3800 \text{ \AA}$ , which are part of the intrinsic quasar continuum. The region between both is called the Ly $\alpha$  forest. Bluewards of Ly $\beta$  it is superimposed by higher order Lyman-series lines and redwards of Ly $\alpha$  there is no HI absorption so all visible absorption lines are due to intervening metal systems.

ionized (as first noted by Gunn, & Peterson 1965).

The Ly $\alpha$  forest is a unique probe of the high-redshift universe in the sense that the observation of e.g. a single quasar can be used to probe gas at a large range of redshifts<sup>2,3</sup>, equivalent to  $\Delta v \sim 40\,000 \text{ km s}^{-1}$  of Doppler motions (after removal of the so-called Quasar proximity zone, areas with enhanced photoionization close to the source quasar, resulting in reduced absorption) or e.g.  $\Delta z \sim 0.8$  at for a  $z = 6$  quasar.

Ly $\alpha$  forest fluctuations can be accurately described in the current  $\Lambda$ CDM framework. As the ionization state of the post-reionization IGM is well described by ionization equilibrium, i.e. there are as many ionizations (in principle due to photons and collisions, but dominated by the first) as recombinations:

$$n_{\text{HI}}\Gamma_{\text{tot}} = \alpha n_{\text{HII}}n_e \quad (2.1)$$

<sup>2,3</sup>Note that extensions to higher order Lyman lines (e.g. Iršič, & Viel, 2014; Boera et al., 2016; Davies et al., 2018b), or equivalent forests for He II (e.g. Jakobsen et al., 1994; Worseck et al., 2016) or metal transitions, e.g. C IV (e.g. D’Odorico et al., 2016) are also possible.

## 2.1. What is the Ly $\alpha$ Forest?

with the case A recombination coefficient  $\alpha \propto T^{-0.7}$ , the total ionization rate  $\Gamma_{\text{tot}}$ , and the number densities  $n_e$ ,  $n_{\text{HI}}$ , and  $n_{\text{HII}}$  of electrons, neutral, and ionized Hydrogen. In a highly ionized IGM (and for simplicity ignoring that any non-Hydrogen gas exists)  $n_e = n_{\text{HII}} \approx n_{\text{H}}$  and eqn. (2.1) simplifies to:

$$n_{\text{HI}} \propto \frac{n_{\text{H}}^2 \alpha}{\Gamma_{\text{tot}}} \quad (2.2)$$

which together with the TDR from eqn. (1.3) yields a simple relation between the optical depth  $\tau$  of Ly $\alpha$  absorption and gas densities  $\rho$  sometimes called the fluctuating Gunn-Peterson absorption (FGPA):

$$\tau \propto \frac{\rho^{2-0.7(\gamma-1)}}{\Gamma_{\text{tot}} T_0^{0.7}}. \quad (2.3)$$

Therefore, in principle the Ly $\alpha$  forest transmission  $F = \exp(-\tau)$  directly probes a degenerate combinations of the underlying matter, ionization and temperature fields. However, this connection is complicated in several ways. First, lines are shifted due to relative motions between different gas clouds leading to redshift space distortions (RSDs). Additionally, absorption lines are broadened relative to the underlying matter field due to two thermal effects: Doppler broadening due to thermal motions and pressure smoothing (see § 2.4). However, line broadening mostly affects the distribution of absorption lines on scales comparable to thermal gas velocities, i.e. a few tens of  $\text{km s}^{-1}$ , far shorter than a typical Ly $\alpha$  forest spectrum, similarly pressure broadening affects gas on scales of  $\sim 100$  kpc. Therefore, on large scales the Ly $\alpha$  forest fluctuations are mostly sensitive to cosmology and structure formation, on small scales they are primarily used to probe astrophysical properties of the IGM. Note that in principle there are other effects that could affect the IGM on small scales, e.g. free streaming of warm dark matter would erase small scale structure compared to a cold dark matter scenario, constraints on this are strongly degenerate with the thermal state of the IGM (see e.g. Viel et al., 2013b, for a measurement of this).

## 2.2. Observability and Datasets

The observable redshift range for the Ly $\alpha$  forest is limited by two effects. For high redshifts  $z \gtrsim 5.5$ , extended parts of the spectra are indeed completely opaque (e.g. in Fan et al., 2006b) as both densities and neutral fraction increase. These fully absorbed patches are called Gunn-Peterson troughs. As these troughs increase in size and at some point ( $z \sim 6$ ) fill the complete Ly $\alpha$  forest range of the quasar spectrum, observations of IGM properties based on the forest become increasingly harder. Additionally, high-redshift quasars tend to be fainter (due to their larger distance), making night-sky emission a larger issue demanding for longer integration times and telluric lines in the atmosphere become more abundant for  $\lambda_{\text{obs}} > 6000 \text{ \AA}$  (roughly equivalent to Ly $\alpha$  absorption at  $z = 5$ ) increasing the demands on data-reduction.

On the other hand, for smaller wavelength  $\lambda_{\text{obs}} \lesssim 3200 \text{ \AA}$  (corresponding to  $z < 1.6$ ) the atmosphere is opaque, making observations from the ground impossible. To observe the Ly $\alpha$  forest at these redshifts one therefore has to use spectrographs on UV space telescopes. This requirement limits the options on telescopes to the Hubble Space Telescope (HST) for the foreseeable future which is far more costly compared to the ground based facilities used at higher redshifts.

The largest currently available datasets for Ly $\alpha$  forest studies from the Sloan Digital Sky Survey (SDSS) and the Baryon Oscillation Spectroscopic Survey (BOSS), containing  $\gtrsim 100000$  medium-resolution (resolving power  $R \sim 2300$ ) Ly $\alpha$  spectra, therefore cover redshifts of  $2 \lesssim z \lesssim 4.2$ . From those datasets high-precision cosmological constraints have been obtained by measuring the baryon acoustic oscillation (BAO) scale at  $z \sim 2.5$  (Font-Ribera et al., 2014; Bautista et al., 2017). These surveys therefore provide excellent possibilities for cosmological parameter analyses. At the same time smaller datasets of higher quality spectra have been used to constrain the physical properties of the IGM and the nature of dark matter. For this work we will use both, survey data for large scale information and archival datasets of high quality spectra for small scales.

## 2.3. The Ly $\alpha$ Forest Flux Power Spectrum

A premier tracer of the fluctuations in the Ly $\alpha$  forest flux field is the line-of-sight flux power spectrum (first described by Croft et al., 1998). Early measurements of the power spectrum (McDonald et al., 2000; Croft et al., 2002) were computed directly from the transmission in the Ly $\alpha$  forest which relies heavily on good measurements of the intrinsic spectrum of the source, i.e. the quasar continuum. To (partly) circumvent this issue subsequent studies (Kim et al., 2004; McDonald et al., 2006; Viel et al., 2008; 2013b; Palanque-Delabrouille et al., 2013; Iršič et al., 2017a; Yèche et al., 2017), including the present work, instead use the power of the flux contrast

$$\delta_F = \frac{F - \bar{F}}{\bar{F}}. \quad (2.4)$$

which is defined as

$$P_F(k) = \langle \tilde{\delta}_F^2(k) \rangle, \quad (2.5)$$

i.e. it is the variance of the Fourier transformed flux contrast  $\tilde{\delta}_F(k)$  over an ensemble of observations, e.g. a set of spectra or bins in  $k$ . Fluctuations on small scales are characterized by a large wavenumber  $k$ , whereas large scale fluctuations are represented with small  $k$ .

There are several observational effects that play a role in the determination of the power spectrum. First, spectra have finite resolution which depends on the spectrograph used for the data acquisition and which generally can be expressed by a line spread function (LSF). Additionally, the spectrum gets discretized on a finite pixel size  $\Delta v$  when it is recorded by the detector. Also, the measured flux will contain some noise  $\mathcal{N}$ , which depends on the intrinsic flux of the source (due to photon counting), but also can depend on e.g. sky background, its subtraction, or detector read-out noise if those are limiting factors. Finally, the spectrum is a product of the source continuum  $C_{\text{true}}$  with the transmission in the IGM  $F_{\text{true}}$  which is estimated as  $C_{\text{estim}}$  and divided out.

In total, the measured transmission  $F$  could therefore be described as:

$$F = \frac{(C_{\text{true}} F_{\text{true}}) \otimes \text{LSF} \otimes \text{rect}(\Delta v) + \mathcal{N}}{C_{\text{estim}}} \quad (2.6)$$

## 2. The Ly $\alpha$ Forest as a Cosmological and Astrophysical Tool

where  $\otimes$  denotes convolution and  $\text{rect}$  is a tophat function. As we take the power in  $\delta_F$ , effects of wrongly estimating the overall continuum will cancel out, but misestimating the wavelength dependence of the continuum might in principle be important (we further discuss how we deal with those in § 3.1.3). The other terms will be Fourier transformed when computing the power. Thus, the noise contribution will (mostly) lead to a constant floor in  $P(k)$ , the convolutions can be replaced by multiplications in Fourier space. Thus, the measured power spectrum becomes:

$$P_{\text{raw}}(k) = P_{\text{true}}(k)W^2(R, \Delta\lambda) + P_{\text{noise}} \quad (2.7)$$

$$W(R, \Delta\lambda) = \exp\left(-\frac{1}{2}(kR)^2\right) \text{sinc}\left(\frac{k\Delta\nu}{2}\right) \quad (2.8)$$

where we used the window function  $W$  which is the product of Fourier transforms for the Gaussian LSF assuming a resolution  $R$  and the pixelization boxcar. In this case the main effect of finite spectroscopic resolution is a Gaussian cutoff in the observed power spectrum for small scales (large  $k$ ). Note that while the assumption of a Gaussian LSF is good for most instruments, in some cases it is not valid, e.g. for the Cosmic Origins Spectrograph (COS) instrument on HST that is used for low redshift Ly $\alpha$  forest studies (see chapter 5). We correct for the mentioned effects when we measure the power (see § 3.2.1).

In the following section we will show how the power spectrum relates to the thermal state of the IGM and illustrate that the cutoff due to resolution can be a major limitations for the analysis.

## 2.4. Connection to the Thermal State of the IGM

The major effect of the thermal state on the Ly $\alpha$  forest is a broadening of absorption lines. Doppler broadening of absorption lines occurs due to thermal motions based on the instantaneous temperatures of the gas. Where the intrinsic line-profile of an absorption line is a Lorentzian distribution only dependent on quantum mechanical properties of the transition, thermal motions inside the absorption systems will convolve the intrinsic

## 2.4. Connection to the Thermal State of the IGM

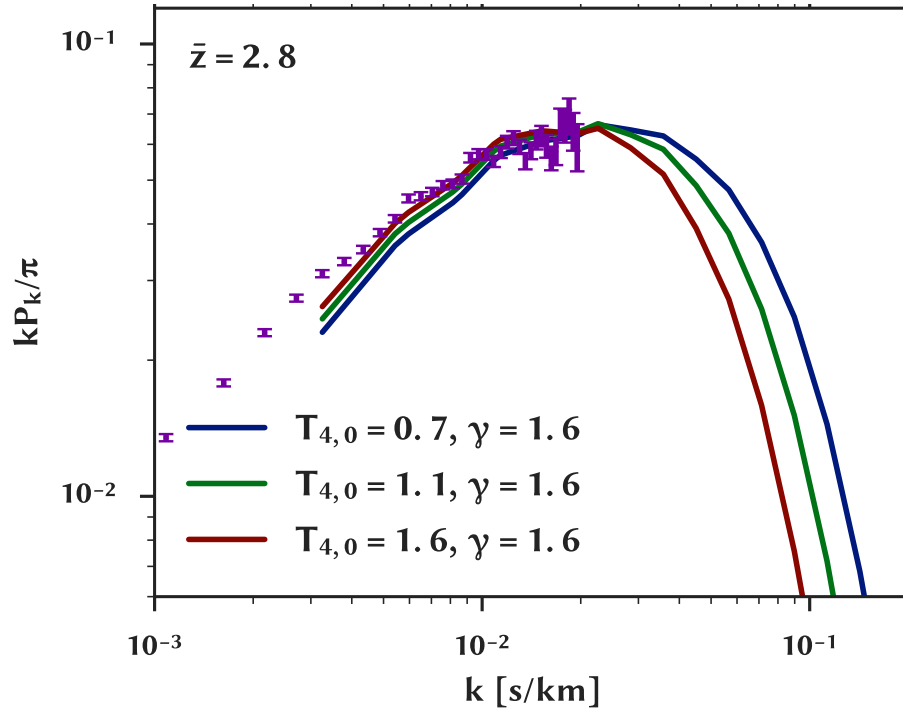


**Figure 2.2.:** The power spectrum measurement from the BOSS survey from Palanque-Delabrouille et al. (2013) as purple points compared to models with 3 different thermal states (colored lines). We can see that the effect of thermal properties on the power spectrum is dominated by a cutoff of the power spectrum with larger  $T$  leading to a cutoff position at larger scales/lower  $k$ ). We can also see that the scales interesting for measuring the thermal state are not covered by the BOSS data which is due to BOSS's limited spectroscopic resolution. The changes on the largest scales, however, are strongly degenerate with the mean transmission  $\bar{F}$  of the Ly $\alpha$  forest as changes of  $\bar{F}$  essentially shift the whole power spectrum up and down.

## 2. The Ly $\alpha$ Forest as a Cosmological and Astrophysical Tool

line profile with a Gaussian, leading to a Voigt profile. For realistic velocities in the IGM of few tens of km s<sup>-1</sup> this Gaussian part dominates, i.e. the optical depth of an absorption line is given by (Draine, 2011; Dijkstra, 2017):

$$\tau = \tau_0 \exp\left(-\left[\frac{(v - v_0)c}{v_0 b}\right]^2\right) \quad (2.9)$$

$$\tau_0 \propto \frac{N_{\text{HI}}}{b} \quad (2.10)$$

$$b = \sqrt{\frac{2k_{\text{B}}T}{m_{\text{H}}}} \quad (2.11)$$

with the optical depth at line center  $\tau_0$ , the observed frequency  $\nu$ , the central frequency of the line  $\nu_0$ , the column density of the line  $N_{\text{HI}}$ , and  $b$  being the Doppler parameter, specifying the thermal width of the line. Note that the constants of proportionality only depend on quantum mechanical properties of the transition.

Absorption lines can fall into three different regimes: unsaturated, saturated or saturated with damping wings. The dependency of their equivalent width  $EW$  to the column density is described by the curve of growth. While for unsaturated lines ( $N_{\text{HI}} \lesssim 10^{14} \text{ cm}^{-2}$ , with the exact transition point being dependent on  $b$ ) this relation is linear, for saturated lines  $EW$  only increases logarithmically with  $N_{\text{HI}}$ . For high column densities ( $N_{\text{HI}} \gtrsim 1 \times 10^{19} \text{ cm}^{-2}$ , so called damped Ly $\alpha$  absorption system (DLA) and sub-DLA systems produced if the line-of-sight comes close to a galaxy, see e.g. Fumagalli et al. 2010) even parts of the line profile dominated by the Lorentzian component produce a measurable absorption and can thus not be ignored as in eqn. (2.9). Those lines exhibit strong damping wings and  $EW \propto \sqrt{N_{\text{HI}}}$  in this regime. For this work the *DLA* systems are a contaminant as it is hard to produce them correctly in simulations, we therefore mask all the lines with visible damping wings in our dataset.

Given the TDR from eqn. (1.3) an increase in  $T_0$  will lead to broader lines, an increase in  $\gamma$  will however broaden lines in overdense regions and decrease the width of lines in underdense regions. For the power spectrum this translates to an approximately Gaussian cutoff with a characteristic scale  $k_{\text{therm}} \propto b^{-1}$ . Note that this is a very similar behaviour

#### 2.4. Connection to the Thermal State of the IGM

compared to the effect of finite spectroscopic resolution from eqn. (2.8). Therefore spectroscopic observations with higher resolution than the thermal broadening are needed to obtain good constraints on the thermal state of the IGM, and the effects of spectroscopic resolution on the power need to be corrected.

We show the effect of varying  $T_0$  on the power spectrum in Figure 2.2. We can see the most precise ( $\sim 2\%$ ) measurement of the large scale power by Palanque-Delabrouille et al. (2013) shown as purple errorbars compared to lines based on hydrodynamical simulations (details for the simulational approach can be found in § 4.2) resulting in different values of  $T_0$ , bracketing the expected range of temperatures at  $z = 2.8^{2.4}$ . Indeed the major effect of changing  $T_0$  is a change in the position of the cutoff. While we also note an effect on the power on large scales, this effect is highly degenerate with the the slope  $\gamma$  of the TDR<sup>2.5</sup> as well as the mean transmission of the Ly $\alpha$  forest and these large scales are most strongly influenced by systematics in the simulation (see § 4.5 for details about those).

Note that the highest-precision measurements (McDonald et al., 2006; Palanque-Delabrouille et al., 2013) currently available based on spectroscopic surveys are not probing the thermal cutoff even for the hottest model shown as they lack the spectroscopic resolution needed to measure the small-scale cutoff of the IGM flux power spectrum and due to the aforementioned degeneracies even 2% measurements of the large scale power cannot be used to obtain a precision constraint of the IGMs thermal state. Existing measurements of the small scale power (McDonald et al., 2000; Croft et al., 2002; Kim et al., 2004; Viel et al., 2008; 2013b), however, have only been performed on  $\sim 20$  spectra, which didn't allow a dense sampling in redshift to constrain thermal evolution and lead to a lacking precision especially on large scale modes, but have been used to set early constraints on the IGM thermal state (Zaldarriaga et al., 2001) in wide redshift bins. There have also been recent measurements using medium resolution X-SHOOTER data

---

<sup>2.4</sup>Note that these models also vary in their pressure smoothing scale  $\lambda_p$  as thermal evolution is continuous and thus higher instantaneous temperatures imply hotter thermal histories.

<sup>2.5</sup>This changes the overall shape of the power spectrum in the cutoff region, but extending to larger scales.

## 2. The Ly $\alpha$ Forest as a Cosmological and Astrophysical Tool

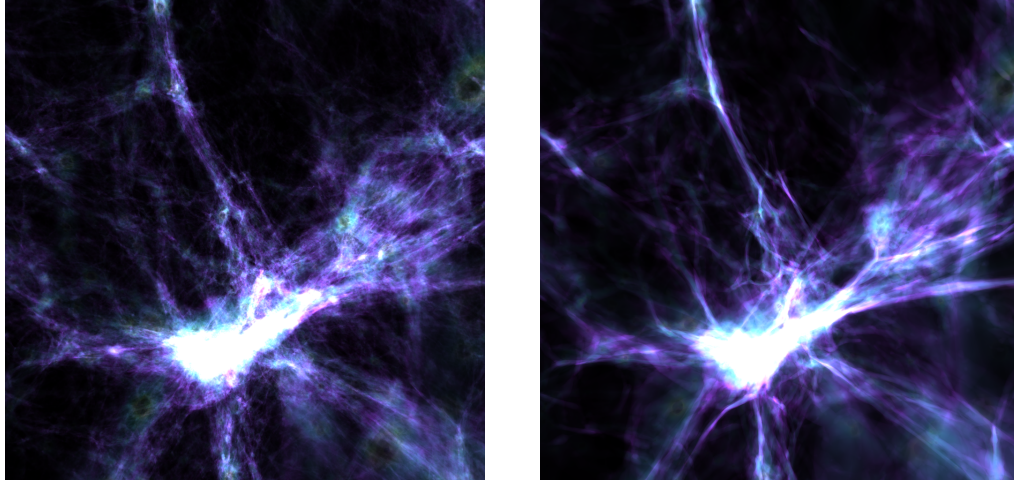


**Figure 2.3.:** Volume renderings of the same box at  $z = 0.2$  as in Figure 1.1 showing dark matter (left) and baryon (right) density fields, but now seen from the center of the box. The color scale is matched between both fields and saturates at mean density (black) to 100 times that value (white). We can clearly see the effect of pressure smoothing erasing small scale structure in the baryons relative to the dark matter.

(Iršič et al., 2017a; Yèche et al., 2017) at  $3 < z < 4.2$  that in principle probe the IGM small scale power, but as we'll see later suffer from uncertainties in the resolution of the X-SHOOTER instrument. Therefore, in chapter 3 we perform our own measurement of the small scale power spectrum based on a large dataset of 74 high-resolution quasar spectra.

In addition to the instantaneous thermal state leading to Doppler broadening there is another important thermal property affecting the absorption lines. In contrast to dark matter, Baryons interact with each other and therefore observe a finite pressure. This leads to the Baryon distribution being smoother than the dark matter distribution. The evolution of this pressure smoothing has been studied in linear theory by Gnedin, & Hui (1998) who found a dependence of the so-called filtering scale  $\lambda_F$  on the full thermal history of the gas as (see also Hui, & Haiman, 2003):

$$\lambda_F^2(t) = \frac{1}{D_+(t)} \int_0^t dt' \lambda_j^2(t') \left( \ddot{D}_+(t') + 2H(t')\dot{D}_+(t') \right) \int_{t'}^t \frac{dt''}{a^2(t'')} \quad (2.12)$$

## 2.4. Connection to the Thermal State of the IGM

with  $D_+$  being the linear growth function,  $H$  the Hubble parameter, and  $\lambda_J^2 = \pi c_s^2 / G\rho \propto T$  being the classical Jeans scale below which gas is pressure supported against gravitational collapse. In the past (Meiksin, & White, 2001; Gnedin et al., 2003; Rorai et al., 2013, e.g. in) the effect of pressure smoothing has been mimicked in simulations by smoothing the dark matter field with a kernel of size  $\lambda_F$ , which in Fourier space results in a multiplication of the 3d matter power spectrum with a cutoff, e.g.  $W = \exp(-k^2 \lambda_F^2 / 2)$ . However, as the filtering scale is already highly nonlinear at the redshifts of interest for IGM thermal evolution studies, full hydrodynamical simulations are needed to correctly account for the effect. Kulkarni et al. (2015) quantified the fully nonlinear pressure smoothing scale  $\lambda_P$  by fitting a cutoff to the 3d power of the real space flux, i.e. the flux obtained from simulations neglecting any redshift space effects.<sup>2.6</sup>

Note again that pressure smoothing depends on the whole thermal history of the gas, i.e. it retains memory of thermal evolution in the past, and is intrinsically a 3d effect, i.e. a 1d measurement like the line-of-sight power spectrum will only see the projected effect of pressure smoothing which is degenerate with Doppler broadening, while a 3d measurement based on e.g. correlations between spectra of close quasar pairs (e.g. Rorai et al., 2017b) can be used to get an independent constraint. We visualized the effect of pressure smoothing on the density field in Figure 2.3 by comparing the baryonic structure to the dark matter structure. In this figure we can clearly notice that the baryon density has far less substructure than the dark matter field. The effect of finite pressure smoothing on the power spectrum is a cutoff similar to the one expected from Doppler broadening, but is governed by the length scale of the smoothing, i.e. appears at scales  $k \gtrsim 1/\lambda_P$ . Thus, a degenerate combination of both effects leads to the cutoff in the power spectrum.

---

<sup>2.6</sup>Note that the accuracy of this approximation is not good enough to be applicable for this study (see Sorini et al., 2016), and e.g. can lead to biased constraints on the pressure smoothing (Rorai et al., 2017b) that need to be corrected by simulations.

## 2.5. Constraining the Thermal State using Other Statistics of the Ly $\alpha$ Forest Flux

Several other statistical properties of the Ly $\alpha$  forest can be used to characterize the thermal state of the IGM. The conceptually simplest way to obtain these constraints is based on fitting a Voigt profile to each absorption line in the Ly $\alpha$  forest, thus obtaining the joint distribution of  $b$  and  $N_{\text{HI}}$ . By assuming that the narrowest lines with a given  $N_{\text{HI}}$  are only thermally broadened, one can obtain constraints of the thermal state (Haehnelt, & Steinmetz, 1998; Schaye et al., 2000; Bryan, & Machacek, 2000; Ricotti et al., 2000; McDonald et al., 2001; Davé, & Tripp, 2001; Rudie et al., 2012; Bolton et al., 2014; Rorai et al., 2018; Hiss et al., 2018). However, this approach becomes complicated by the need of automatic line fitting tools for simulations, blending between several absorption lines, or the definition of the "narrowest" lines especially if spurious noise spikes were identified as a line or metal absorption lines were fit as Ly $\alpha$ . Note that in Hiss et al. (2018), we also performed a measurement based on this approach, based on the same spectral dataset we used in this work.

There have also been measurements based on several other statistical properties of the continuous Ly $\alpha$  flux, e.g. the flux probability density function (PDF) (Bolton et al., 2008; Viel et al., 2009; Lee et al., 2015; Rorai et al., 2017a; a), i.e. the distribution of flux values inside observed spectra, and wavelet decompositions of the forest (Theuns et al., 2002; Lidz et al., 2010; Garzilli et al., 2012) have been used. Some of those constraints (Bolton et al., 2008; Viel et al., 2009; Lidz et al., 2010) led to strongly discrepant results compared to the rest with temperatures at mean density being a factor of  $\sim 2$  higher or values of  $\gamma < 1^{2.7}$  in contrast to the  $\gamma \sim 1.6$  expected from simulations.

The formally most precise measurements of the thermal state are based on the curvature, i.e. the second derivative, of the smoothed transmission (Becker et al., 2011; Boera et al., 2014). However, this method so far only provided measurements of the temperature at characteristic overdensities  $\Delta_*$ , but is insensitive to  $\gamma$  (but see Boera et al.,

---

<sup>2.7</sup>A so-called inverted TDR that might need new physics to be explained (Puchwein et al., 2012)

## 2.5. Constraining the Thermal State using Other Statistics of the Ly $\alpha$ Forest Flux

2016, for an updated approach). Therefore it needs to rely on external measurements of  $\gamma$  to assess  $T_0$ , and is harder to interpret on its own.

Finally, the quasar pair phase angle distribution (Rorai et al., 2013; 2017b), has been used to obtain constraints on the pressure smoothing scale independent of line-of-sight effects such as Doppler broadening.

The different approaches, differences in methodological treatment, e.g. marginalization of nuisance parameters and propagation of uncertainties, as well as precision of numerical simulations, impede the comparison of these measurements and therefore complicate obtaining physical conclusions based on these data. Overcoming these issues was a main motivation for this project and required homogeneous treatment of the data, inference in more than five dimensions to allow for proper marginalization over hyperparameters, hydrodynamical simulations, and fast interpolation techniques to allow inference based on relatively few simulation runs. We obtain a new self-consistent measurement of thermal evolution in the IGM in chapter 4 which is then extended to lower redshifts that have previously not been studied for this purpose in chapter 5.



# 3. A New Measurement of the IGM Power Spectrum

In this chapter, we measure the Ly $\alpha$  forest flux power spectrum from high resolution data to determine its thermal cutoff and thus enable measurements of the thermal state of the IGM in chapter 4. Note that while the thermal history of the IGM has a strong effect on the cutoff scale the small scale power is also sensitive to the nature of dark matter (Viel et al., 2013b; Iršič et al., 2017b). The power spectrum in general can also be used to deduce constraints for a variety of cosmological parameters, e.g. the mass of neutrinos (Palanque-Delabrouille et al., 2015; Yèche et al., 2017; Baur et al., 2017) leading to additional usecases for our analysis outside the main scope of this thesis.

In this chapter we perform a new power spectrum analysis on a large sample of archival high-resolution spectra which we'll combine with the existing low- and medium-resolution measurements to enable an accurate measurement of thermal evolution in the IGM in chapter 4.

## 3.1. High-Resolution Quasar Dataset

In this section we will describe the dataset we used for our measurement. First we explain how our quasar sample was constructed. Then we describe which parts of the selected data were used and how we masked regions of the data to remove contaminants like e.g. metals or DLAs Finally we will explain how we regulate the mean flux of our spectra.

### 3. A New Measurement of the IGM Power Spectrum

#### 3.1.1. Dataset

Our measurement of the power spectrum was performed using 38 high-resolution quasar spectra (see Table 3.1) from Dall’Aglia et al. (2008) observed with the Ultraviolet and Visual Echelle Spectrograph (UVES) at the Very Large Telescope (VLT) (Dekker et al., 2000), and 36 spectra (see Table 3.2) from the Keck Observatory Database of Ionized Absorption toward Quasars (KODIAQ) project (Lehner et al., 2014) observed with the High Resolution Echelle Spectrometer (HIRES) at Keck (Vogt et al., 1994). For the latter we used the highest S/N part of DR1 (O’Meara et al., 2015) and additional data beyond DR1 (mostly early reductions of objects in DR2 O’Meara et al., 2017) reduced in the same way. Reduced and continuum fitted spectra of all UVES and KODIAQ DR1 data used here are available in the `igmspec` package (Prochaska, 2017), KODIAQ DR2 data will be available in future `igmspec` releases and on the KODIAQ database webpage<sup>3.1</sup>.

Most of the UVES spectra have full coverage between the atmospheric cutoff at  $\lambda_{\text{obs}} \approx 3100 \text{ \AA}$  and  $\lambda_{\text{obs}} \approx 1 \mu\text{m}$ . This allows us to use a large range of spectrum redward of the Ly $\alpha$  forest to search for metal lines as well as enabling us to search for Lyman Limit Systems (LLSs) using higher order Lyman series transitions, in many cases even exploiting coverage of the Lyman-limit. For the KODIAQ data the typical red spectral coverage ends at  $\lambda_{\text{obs}} \sim 6000 \text{ \AA}$ , while the blue spectral cutoff is comparable to UVES  $\lambda_{\text{obs}} \sim 3100 \text{ \AA}$ . For a few cases in both datasets, however, even the Ly $\alpha$  forest was not fully covered.

The objects used in our analysis were chosen to have a median S/N  $> 20$  per  $6 \text{ km s}^{-1}$  interval inside the Ly $\alpha$  forest region covered by the spectra. We also chose to omit spectra with known broad absorption lines (BALs). Finally we omitted sightlines with  $3.0 < z < 3.5$  that were color selected to avoid potential biases due to their increased abundance of LLSs (Worseck, & Prochaska, 2011).

The distribution of S/N for the dataset used in our analysis is shown in Figure 3.1. Many objects have a much larger S/N than our cut (up to about a median S/N of  $150$  per  $6 \text{ km s}^{-1}$

---

<sup>3.1</sup><https://koa.ipac.caltech.edu/applications/KODIAQ/>

### 3.1. High-Resolution Quasar Dataset

**Table 3.1.:** UVES spectra from Dall’Aglío et al. (2008) used for our analysis

Object	$z_{\text{QSO}}$	median S/N per 6 km s <sup>-1</sup>
HE1341–1020	2.137	58.1
Q0122–380	2.192	56.4
PKS1448–232	2.222	57.4
PKS0237–23	2.224	102.4
HE0001–2340	2.278	65.9
Q0109–3518	2.406	70.0
HE1122–1648	2.407	171.6
HE2217–2818	2.414	93.6
Q0329–385	2.437	58.4
HE1158–1843	2.459	66.7
Q2206–1958	2.567	74.5
Q1232+0815	2.575	45.8
HE1347–2457	2.615	62.0
HS1140+2711	2.628	88.9
Q0453–423	2.663	77.6
PKS0329–255	2.705	48.0
Q1151+068	2.758	49.1
Q0002–422	2.768	75.0
HE0151–4326	2.787	98.1
Q0913+0715	2.788	54.4
Q1409+095	2.843	24.7
HE2347–4342	2.886	152.3
Q1223+178	2.955	33.4
Q0216+08	2.996	36.8
HE2243–6031	3.011	118.8
CTQ247	3.026	69.1
HE0940–1050	3.089	69.6
Q0420–388	3.120	116.2
CTQ460	3.141	40.9
Q2139–4434	3.208	31.2
Q0347–3819	3.229	83.9
PKS2126–158	3.285	63.6
Q1209+0919	3.291	30.2
Q0055–269	3.665	75.7
Q1249–0159	3.668	69.7
Q1621–0042	3.708	77.7
Q1317–0507	3.719	42.0
PKS2000–330	3.786	150.8

**Table 3.2.:** HIRES spectra from KODIAQ (O’Meara et al., 2015) used for our analysis

Object	$z_{\text{QSO}}$	median S/N per 6 km s <sup>-1</sup>
J122824+312837	2.200	87.3
J110610+640009	2.203	58.5
J162645+642655	2.320	103.7
J141906+592312	2.321	36.7
J005814+011530 <sup>3</sup>	2.495	36.2
J162548+264658 <sup>3</sup>	2.518	43.9
J121117+042222	2.526	33.6
J101723–204658	2.545	70.3
J234628+124859	2.573	75.1
J101155+294141 <sup>1</sup>	2.620	129.9
J082107+310751	2.625	64.0
J121930+494052	2.633	90.3
J143500+535953	2.635	65.0
J144453+291905	2.669	133.7
J081240+320808	2.712	48.8
J014516–094517A	2.730	76.8
J170100+641209 <sup>3</sup>	2.735	81.8
J155152+191104	2.830	30.2
J012156+144820	2.870	54.5
Q0805+046 <sup>2</sup>	2.877	26.8
J143316+313126	2.940	53.8
J134544+262506	2.941	34.7
J073621+651313	3.038	25.7
J194455+770552 <sup>1</sup>	3.051	30.4
J120917+113830	3.105	31.4
J114308+345222 <sup>1</sup>	3.146	31.9
J102009+104002	3.168	35.9
J1201+0116 <sup>2</sup>	3.233	30.1
J080117+521034 <sup>1</sup>	3.236	43.2
J095852+120245 <sup>1</sup>	3.298	44.8
J025905+001126	3.365	26.3
Q2355+0108 <sup>2</sup>	3.400	58.3
J173352+540030	3.425	57.3
J144516+095836 <sup>1</sup>	3.530	24.6
J142438+225600 <sup>1</sup>	3.630	29.3
J193957–100241	3.787	65.5

<sup>1</sup>objects are part of DR2, but a pre-DR2 reduction has been used

<sup>2</sup>objects are not part of DR1 or DR2, but reduced in the same way

<sup>3</sup>objects are part of DR1, but a pre-DR1 reduction has been used

### 3. A New Measurement of the IGM Power Spectrum

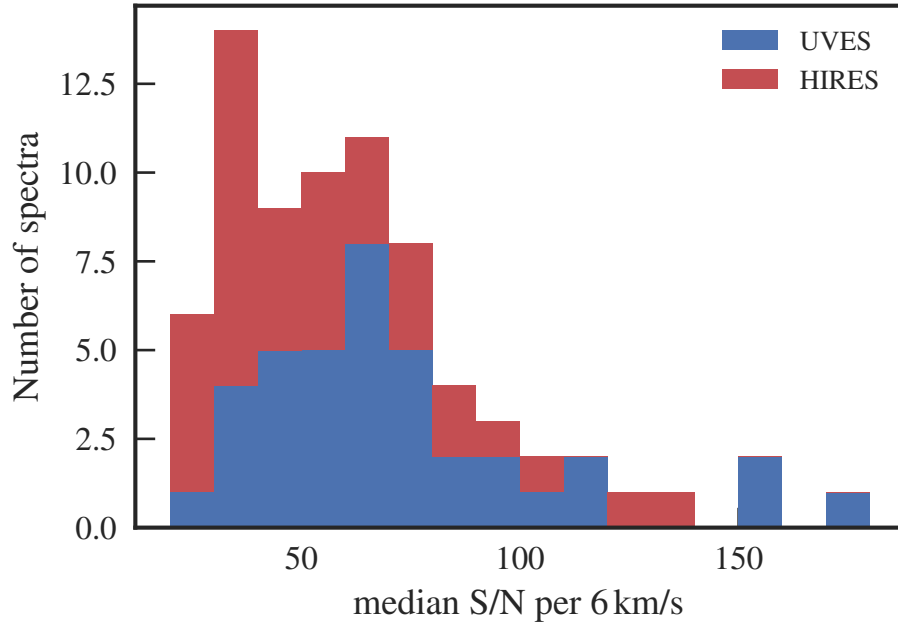


**Figure 3.1.:** Histogram of the median S/N per  $6 \text{ km s}^{-1}$  in the  $\text{Ly}\alpha$  forest region used divided by dataset. Note that we only used spectra with S/N > 20 in the dataset

inside the  $\text{Ly}\alpha$  forest in a sightline). This very high S/N enables us to perform the measurement without strong systematics due to the limited accuracy of our noise model affecting our measurement at the scales of interest.

The nominal FWHM spectral resolution of the data varies between  $3.1 \text{ km s}^{-1}$  and  $6.3 \text{ km s}^{-1}$  with a typical value around  $6 \text{ km s}^{-1}$ . Therefore all  $\text{Ly}\alpha$  absorption lines are resolved and we expect thermal broadening and broadening due to pressure smoothing to be the effects determining the smoothness of lines, and not smoothing due to finite spectroscopic resolution (see e.g. Bolton et al., 2014, for a measurement of line width for thermally broadened lines).

The data was already reduced and continuum fit, and we briefly summarize the details here. The UVES data were fit with both a global power law in non-absorbed regions and local cubic splines fitted automatically with spline point separations depending on continuum slope. Systematic biases in this technique were estimated and corrected using

### 3.1. High-Resolution Quasar Dataset

a Monte Carlo analysis on mock data by Dall’Aglio et al. (2008). The HIRES continua were hand-fitted by John O’Meara one echelle order at a time by placing Legendre polynomial anchor points at non-absorbed positions (for estimates of continuum fitting errors, see Kirkman et al., 2005; Faucher-Giguère et al., 2008b). Afterwards a 4th to 12th order polynomial was fit through the anchors. Further details about the reduction and continuum fitting techniques can be found in the respective data papers (Dall’Aglio et al., 2008; O’Meara et al., 2015).

We will use this high-resolution dataset to measure the small scale power spectrum of the Ly $\alpha$  forest in redshift bins of size  $\Delta z = 0.2$  with central redshifts between  $\bar{z} = 1.8$  and  $\bar{z} = 3.4$ . Each of the bins contains at least eight quasar spectra, with the majority (all but the low and high redshift edges of our sample) containing more than 14 quasar spectra. The datasets also contain eight spectra that cover higher redshifts which we did not analyze due to the small amount of data available (two spectra cover  $z \gtrsim 4.0$ , the rest only cover the forest for  $z < 3.6$  just half a bin further than our analysis).

In this work, we compare our power spectrum measurements to measurements from lower spectral resolution data from BOSS (Palanque-Delabrouille et al. 2013, hereafter PD+13)) and from the XQ-100 survey (Iršič et al., 2017a) based on X-SHOOTER data, and also conduct joint model fits. To facilitate this comparison we use the same binning in redshift from  $\bar{z} = 2.2$  to  $\bar{z} = 3.4$ .

#### 3.1.2. Spectral Masking Procedure

To prepare the data for the power spectrum computation we restrict our attention to the restframe wavelength range of  $1050 \text{ \AA} < \lambda_r < 1180 \text{ \AA}$ . This was done to exclude the Ly $\alpha$  proximity zone, also accounting for possibly large redshift errors, as well as to exclude the Ly $\beta$  and O VI  $\lambda 1035$  emission lines and possible blueshifted absorption from these and increased continuum fitting errors close to emission lines. This is the same range used in PD+13 and is considered a conservative choice for the Ly $\alpha$  forest region.

We masked parts of the spectrum to reduce contaminations due to low-quality data,

### 3. A New Measurement of the IGM Power Spectrum

high-column density absorbers such as DLAs, and metal lines. If a pixel is already masked during the reduction (due to e.g. cosmic rays or gaps in spectral coverage) it stays masked. According to McDonald et al. (2005a) excluding DLAs and LLSs from power spectrum calculation only changes the power by  $< 2\%$  on the scales of interest for our analysis. We nevertheless excluded absorbers with clearly visible damping wings, i.e. DLAs and super-LLSs, from our spectra to make sure those do not influence the result. We masked the core and wings of these strong absorbers by eye until the wings are below the noise level of the spectra. In most cases this leads to the exclusion of big continuous spectral regions at the boundary of a redshift bin or the whole data of this object falling inside a redshift bin. Where a DLA mask removed only the bin center we used the longer of the two remaining spectral regions at the bin boundaries to compute the power. Therefore, spectra with DLAs are only shorter, but with no additional large gaps in the data. Finally, we removed spectra that were shorter than 10% of a redshift bin corresponding to a minimum length of  $\Delta z \sim 0.02$  (or  $3500 \text{ km s}^{-1}$ ) to avoid noisy contributions from short spectra that consist of only few absorption lines.

Metal lines in the Ly $\alpha$  forest are expected to increase the power primarily on small scales ( $k \gtrsim 0.1 \text{ s km}^{-1}$ , see McDonald et al., 2000; Lidz et al., 2010) due to their narrower widths compared to Ly $\alpha$ , but due to correlations induced by the rest-frame velocity separations of different transitions (e.g. between Si III and H I-Ly $\alpha$  or between the C IV doublet lines) there is contamination on larger scales as well (Croft et al., 1999; McDonald et al., 2006).

To reduce the impact of metal absorption inside our sightlines we masked metal lines in the forest region. We identified metal absorption lines in the Ly $\alpha$  forest by having two of the authors (H. Hiss and M. Walther) visually inspect the spectra and mask metal contamination in several ways. We started by look masking all strong metal absorption lines corresponding to the redshifts of identified DLAs. For this purpose, we used all metal transitions in Table 3.3 and masked a region of  $60 \text{ km s}^{-1}$  in each direction around each identified absorber. Then we search for absorption from common doublet transitions (Si IV, C IV, Mg II, Al III, Fe II) redwards of the forest where the spectrum is mostly clean

### 3.1. High-Resolution Quasar Dataset

**Table 3.3:** List of metal transitions that were masked

Ion	$\lambda_{\text{rest}}/\text{\AA}$	Metal transition	$\lambda_{\text{rest}}/\text{\AA}$
O VI <sup>a</sup>	1031.9261	Si IV <sup>a</sup>	1402.770
C II	1036.3367	Si II	1526.7066
O VI	1037.6167	C IV <sup>a</sup>	1548.195
N II	1083.990	C IV <sup>a</sup>	1550.770
Fe III	1122.526	Fe II	1608.4511
Fe II	1144.9379	Al II	1670.7874
Si II	1190.4158	Al III	1854.7164
Si II	1193.2897	Al III	1862.7895
N I	1200.7098	Fe II	2344.214
Si III <sup>a</sup>	1206.500	Fe II	2374.4612
N V	1238.821	Fe II	2382.765
N V	1242.804	Fe II	2586.6500
Si II <sup>a</sup>	1260.4221	Fe II	2600.1729
O I	1302.1685	Mg II	2796.352
Si II	1304.3702	Mg II	2803.531
C II	1334.5323	Mg I	2852.9642
C II*	1335.7077	Ca I	3934.777
Si IV <sup>a</sup>	1393.755	Ca I	3969.591

<sup>a</sup>strongest transitions, therefore used for all the masking techniques

### 3. A New Measurement of the IGM Power Spectrum

and mask all associated metal lines analogous to our procedure for DLAs (using the same metal catalog and mask width), until there are no doublet features left redward of the forest. We also masked out a region of  $200 \text{ km s}^{-1}$  in each direction around redshift zero to get rid of metal contamination from the Milky Way (in this case the only relevant transition is Ca I for  $2.33 < z_{\text{QSO}} < 2.78$ ).

Additionally, we used an automated partial LLS (pLLS) finder written by John O’Meara to identify strong absorption systems. This finder works by searching for pixels with zero flux (within some threshold) at the corresponding positions of Ly $\alpha$ ,  $\beta$ ,  $\gamma$  and higher Lyman transitions if available and grouping them into systems of LLS candidates. The candidates were then visually inspected by one of the authors (John O’Meara) and compared to theoretical line profiles of absorbers with  $\log(N_{\text{HI}}) = 15, 16, 17$  in Ly $\alpha$  to Ly $\gamma$ , and systems which appeared consistent were positively identified as pLLSs. For these systems, associated metal absorbers from a reduced line list (see Table 3.3 absorbers marked with a) were masked with the same velocity window size as above. Note that the hydrogen absorption arising from the pLLSs identified in this way was not masked regardless of their  $N_{\text{HI}}$ .

Lastly we perform a line-fitting analysis (see Hiss et al., 2018) using a semi-automatic wrapper around VPFIT (Carswell, & Webb, 2014) on the same set of Ly $\alpha$  spectra. The result of this is a distribution of line widths  $b$  and column density  $N_{\text{HI}}$  for all fitted lines assuming that all absorption is due to hydrogen. For HI gas at a given column density lines are broadened both thermally (due to finite pressure broadening and instantaneous temperature Doppler broadening) and hydrodynamically due to local gas motions. There is a minimum broadening  $b_{\text{cut}}(N_{\text{HI}})$  populated by absorbers with zero line-of-sight peculiar velocity which are purely thermally broadened (see e.g. Schaye et al., 2000; Hiss et al., 2018, for more details). Therefore  $b(N_{\text{HI}})$  should cut off for  $b < b_{\text{cut}}(N_{\text{HI}})$  and all remaining lines narrower than this cutoff can be attributed to fitting artifacts at the edges of strong absorbers, noise fluctuations, or narrow metal absorption lines. This cutoff is fit using an iterative procedure similar to the one used in Rudie et al. (2012). We identified all the lines in previously unmasked spectral regions fulfilling

### 3.1. High-Resolution Quasar Dataset

$b < 11 \text{ km s}^{-1} (N_{\text{HI}}/10^{12.95} \text{ cm}^{-2})^{0.15}$  as these are narrower than the thermal cutoff (see Hiss et al., 2018, for details). For each of these lines (that are in the Ly $\alpha$  forest region) we checked if they could be identified using a second metal transition clearly lining up at the same redshift. In practice, these identifications were most easily made when both metal transitions form a doublet. Given a positive identification, masking was then performed as for metal absorbers that we identified redward of the Ly $\alpha$  forest, i.e. determining the redshift of the absorber and using the full list of metal lines in Table 3.3.

Neither of these techniques produces a fully metal free Ly $\alpha$  forest, and we briefly elaborate on these limitations. The search for metals redwards of the forest only finds transitions if both doublet counterparts are visible at redder wavelength than the Ly $\alpha$  emission line. If the doublet counterpart of a line falls into a spectral region that was not covered or is blended with a different line (from either a different absorber redshift or e.g. a telluric absorption feature) the contaminating system will often go undetected. For example, for a C IV  $\lambda$ 1548/1550 system at  $z > 2.5$  that might contaminate the forest, the Mg II  $\lambda$ 2796/2803 doublet would land at  $\lambda_{\text{obs}} > 1 \mu\text{m}$  and hence outside of the spectral coverage of our spectra, so only if the absorber shows Fe II or Al III doublets would this C IV absorber be masked. On the other hand especially for the higher redshift bins a large fraction of the spectral range redwards of the forest is contaminated by telluric absorption making doublet identification very challenging. The largest problem for this method is therefore limited usable spectral coverage in the red.

For the automated pLLS finder at least Ly $\alpha$  to Ly $\gamma$  need to be detectable to identify a pLLS. This leads to a minimal redshift of  $z \gtrsim 2.1$  for absorbers that can be identified as they need to be at observed wavelength higher than the atmospheric cutoff  $\lambda_{\text{obs}} \approx 3000 \text{ \AA}$ . For reduced spectral coverage in the blue this minimal redshift is correspondingly higher.

The last of our metal masking procedures only recognizes metal absorption lines significantly narrower than the cutoff in the  $b(N_{\text{HI}})$  distribution and requires a second metal transition for identification. Therefore singlet lines are not masked by this technique unless another transition from a different metal species clearly lines up with them. Also metal absorbers were not removed if all components are broadened above the  $b(N_{\text{HI}})$

### 3. A New Measurement of the IGM Power Spectrum

threshold adopted, and are therefore not recognized as metal candidates.

In Figure 3.2 we show an example to illustrate how much of a typical spectrum is masked. The black line shows the non-masked part of the spectrum while the red line shows parts that are masked due to possible metal contamination. One can see that many narrow lines in the spectrum are masked, but also that many regions of the forest coincidentally overlap with positions where metal lines associated with our identified absorbers could lie, but that don't actually contain any visible metal absorption.

In Figure 3.3 we present an overview of the dataset. For each quasar spectrum the emission redshift is shown as well as the full coverage of the spectrum after masking pre-existing gaps in the data and DLAs (which therefore appear as white gaps). The remaining spectrum is divided into the data used (dark colors), masked data due to possible metal contamination (bright colors), and spectra not used due to failing our requirement of spectral extent (yellow). We also show the usable Ly $\alpha$  forest pathlength after applying the full masking procedure compared to the available pathlength when not masking metals in Figure 3.4. Up to  $\sim 40\%$  of the forest gets removed by applying our metal masking procedure strongly reducing our dataset size and therefore the precision of our measurement results. Although not perfect, our procedure significantly reduces the metal line contamination in our spectra, which decreases the amount of small-scale power compared with an unmasked dataset as we will see in § 3.3.1. However, this masking also changes the power spectrum due to the application of a complex window function in configuration space. To correct for this effect we forward model the masking (see § 3.2.4).

#### 3.1.3. Mean Flux Regulation and Continuum Uncertainties

In principle the estimation of quasar continua in the data is subject to errors as well. We perform our power spectrum measurement on the flux contrast

$$\delta_F = \frac{F - \bar{F}}{\bar{F}}, \quad (3.1)$$

### 3.1. High-Resolution Quasar Dataset

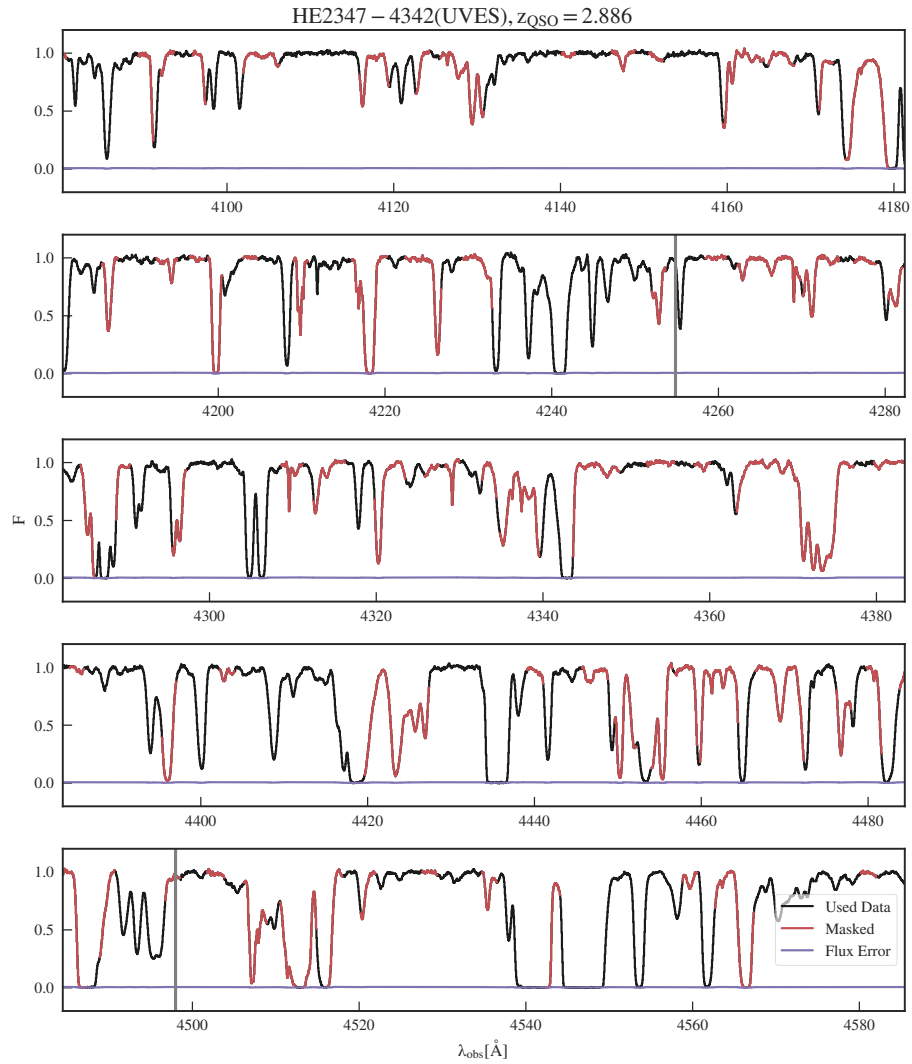


**Figure 3.2.:** The Ly $\alpha$  forest region for one of our spectra (HE2347-4342) with regions masked due to possible metal contamination in red. The purple line shows the error level of the spectrum. Gray vertical lines show the boundaries of our redshift bins. Note that due to our approach not only metals are masked, but also coincidental pieces of the Ly $\alpha$  forest.

### 3. A New Measurement of the IGM Power Spectrum

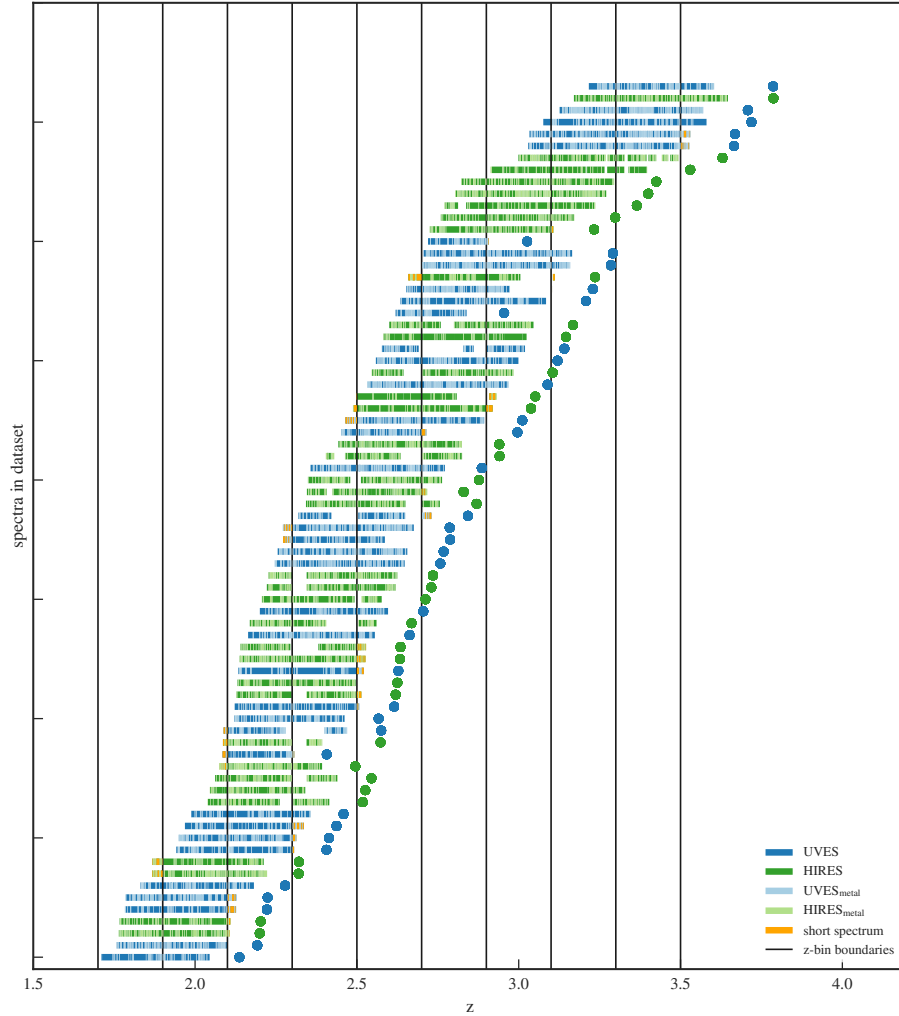


**Figure 3.3.:** Redshift coverage of the dataset used colored by spectrograph. Blue (green) lines show the spectral coverage of each used spectrum in the Ly $\alpha$  forest for the UVES (HIRES) subset. Circles mark the corresponding quasar redshifts. Most of the long gaps in this figure are due to missing data between e.g. non-overlapping echelle orders or masked out DLAs while the light colored parts show masks due to possible metal contamination (see § 3.1.2). Orange lines show regions that were ultimately rejected because of limited forest coverage. Vertical lines mark boundaries of the redshift bins used in the analysis.

### 3.1. High-Resolution Quasar Dataset

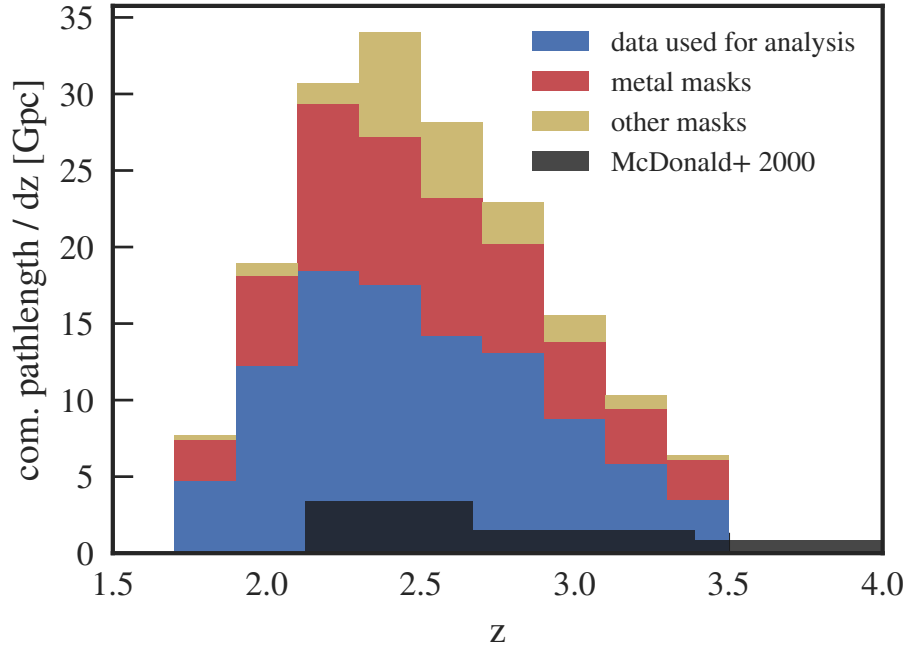


**Figure 3.4.:** The pathlength of used data in our analysis compared to the pathlength of spectra masked due to several reasons (metals: red, other: yellow). About 30%-40% of each redshift bin were masked due to possible metal contamination. Far less due to other things, e.g. DLAs, bad reductions or only short available pathlength. As a comparison the amount of data in McDonald et al. (2000) is shown in black for their redshift binning. Normalization is such that the area (and not the height) of each bar corresponds to the total path inside it.

with  $\bar{F}$  being the mean transmission of the Ly $\alpha$  forest (see also chapter 2). Because of this, any global misplacement of the continuum will be divided out as long as the mean transmission measurement we divide by is measured on the same spectrum. In addition, incorrect placement of the continuum could lead to gradients or wiggles in the data that could source additional large scale power (on scales  $k < 0.001 \text{ s km}^{-1}$ ). However, this will not strongly impact the small scale power measurement we want to perform in this work<sup>3.2</sup>(Lee et al., 2012).

<sup>3.2</sup>We performed tests on model simulations at  $z = 3$  including quasar continua. Comparing the power spectrum using the true continuum vs. a hand-fitted continuum showed that only the very largest scales (smallest  $k$ ) were affected by the procedure.

### 3. A New Measurement of the IGM Power Spectrum

Nevertheless, we perform a mean flux regulation on the dataset using the technique of Lee et al. (2012) which enables us to easily divide out the mean transmission as well as possible gradients in the continuum fits. For this the transmission of the Ly $\alpha$  forest region (excluding masked pixels as well as possible proximity regions as discussed earlier) of each quasar sightline is first fit by a linear relation  $f(z)$  times the mean transmission function  $\bar{F} = \exp(-\tau_{\text{eff}})$  with

$$\tau_{\text{eff}} = C + \tau_0 \left( \frac{1+z}{1+z_0} \right)^\beta \quad (3.2)$$

following the functional form and parameters from Becker et al. (2013). Afterwards  $f(z)$  is divided out so that the mean flux evolution of each spectrum follows the same relationship.

The flux contrast  $\delta_F$  is now easily obtained by using eqn. (3.1) on mean flux regulated spectra using eqn. (3.2) for the mean flux evolution instead of dividing each spectrum by a mean transmission estimate for this spectrum. This allows us to divide out the mean flux at each pixel analytically based on the fit of the mean flux evolution across each spectrum. While this in principle leads to a reduced large-scale power (Lee et al., 2012), we are not measuring the affected scales in this work.

The resulting spectra are finally divided into our redshift bins of  $\Delta z_{\text{chunk}} = 0.2$  (with the first bin starting at  $z = 1.7$ ) to increase redshift resolution to a level where we could closely monitor thermal evolution. We will henceforth call these pieces of spectra "spectral chunks".

## 3.2. Power Spectrum Measurement and Forward Modeling Procedure

In this section we describe our procedure for measuring the flux power spectrum. First we explain how we measure the raw power spectrum. Next we discuss the impact of our masking (especially the masking of metal contaminants) on this measurement. After this

### 3.2. Power Spectrum Measurement and Forward Modeling Procedure

we discuss the models we use in most of this work, how we generate mock spectra from them, and approximate the data covariance matrix by combining information from both data and models. Finally, we discuss how we create a fast emulator of our model power spectra, and use this to fit models to our data, allowing us to correct for the masking.

#### 3.2.1. Measuring the Power Spectrum

We calculate the power spectrum from the flux contrast  $\delta_F$  defined in eqn. (3.1). As our spectra are not periodic and are not regularly sampled because of masking, we Fourier transform  $\delta_F$  using a Lomb-Scargle periodogram (Lomb, 1976; Scargle, 1982), allowing us to compute the raw power  $P_{\text{raw}}(k)$  of each spectrum for a linearly spaced set of modes from the fundamental mode given by the length of the spectral chunk to the Nyquist limit. We subtract the noise power  $P_{\text{noise}}(k)$  from this raw power, and divide the difference by the window function  $W_R$  resulting from finite spectroscopic resolution  $R$ , following the FFT method described in PD+13:

$$P_{\text{data}}(k) = \left\langle \frac{P_{\text{raw}}(k) - P_{\text{noise}}(k)}{W_R^2(k, R, \Delta v)} \right\rangle, \quad (3.3)$$

with

$$W_R(k, R, \Delta v) = \exp\left(-\frac{1}{2}(kR)^2\right) \frac{\sin(k\Delta v/2)}{(k\Delta v/2)}, \quad (3.4)$$

and  $\Delta v$  refers to the pixel scale of the spectra in velocity units.

The noise power  $P_{\text{noise}}$  is measured by creating 100 realizations of Gaussian random noise generated from the  $1\sigma$  error vector of each quasar spectrum. The resolution assumed for the window function correction is the nominal slit-resolution of the spectrograph which is different from the actual spectral resolution of the data, which also depends on the seeing of the observations. For the typical resolution in our dataset (so a resolving power of 50,000 or equivalently  $R = 2.55 \text{ km s}^{-1}$ ) we get  $W_R^2(0.1 \text{ s km}^{-1}) \sim 0.94$ . Given this small correction, even  $\sim 20\%$  error in our knowledge of the resolution (due to the unknown seeing), would only lead to a small  $\lesssim 4\%$  correction of the power at  $k < 0.1 \text{ s km}^{-1}$  (for further discussion of this point see § 3.3.2 and Appendix A). Therefore,

### 3. A New Measurement of the IGM Power Spectrum

the resolution uncertainty does not significantly affect our measurement of the  $k$ -modes we consider.

We chose to use the same logarithmically spaced  $k$ -bins<sup>3.3</sup> as in McDonald et al. (2000), i.e. using 10 bins per decade, for our analysis. Note that this is different from the linear spacing adopted by PD+13 and Iršič et al. (2017b).

We adopt the same Fourier normalization convention as the BOSS measurement (PD+13), such that the variance in flux contrast is  $\sigma_{\delta_F}^2 = \sigma_F^2 / \bar{F}^2 = \int_{-\infty}^{\infty} P(k) dk / (2\pi)$ . Note that this differs from the conventions used by some older high-resolution measurements (see Appendix C) leading to additional normalization factors needed when comparing to those results.

#### 3.2.2. The Window Function Resulting from Masking

As described in § 3.1.2 we masked out parts of the data in real space due to metal contamination. This is a different approach than the one used by PD+13 who estimated the metal power from transitions with  $\lambda > \lambda_{\text{Ly}\alpha, \text{rest}}$  by measuring the power redwards of the forest in lower redshift quasar spectra. The power measured in this way was then subtracted from the measurement, but this method can never account for transitions with  $\lambda < \lambda_{\text{Ly}\alpha, \text{rest}}$  which always fall into the forest (e.g. the Si III  $\lambda 1206$  line that leads to the Si III correlation feature in those measurements, see McDonald et al. 2006).

Masking spectra in configuration space with a window function  $W_m$  leads to the measured  $P_{\text{masked}}$  for each spectrum being effectively a convolution of the true power  $P_{\text{true}}$  with the square of the Fourier transform  $\tilde{W}_m$  of this window function:

$$P_{\text{masked}} = P_{\text{true}} \otimes \tilde{W}_m^2. \quad (3.5)$$

---

<sup>3.3</sup>The averaging  $\langle \dots \rangle$  is performed over the individual periodograms of all spectral chunks inside a redshift bin, and also the average over all modes  $k$  inside logarithmic bins in  $k$ , where equal weights are given to each individual mode from any spectrum. As the fundamental mode of a shorter spectrum is at larger  $k$ , there are less modes available in a given band power for shorter spectra and they are therefore effectively downweighted by performing the average over modes.

### 3.2. Power Spectrum Measurement and Forward Modeling Procedure

Determining the true power thus requires deconvolving the window function or adopting a different technique to measure the power taking into account the windowing (like the minimum variance estimator used in McDonald et al., 2006). In this work we opt to use a simpler approach by generating forward models of the data with and without the windowing applied to be able to determine the effect this window function has on our data. In the end, we correct our data for those effects by dividing the measurement by a correction function based on these models. In the remainder of this section we describe how our forward models are generated, how we estimate the data covariance matrix based on those models, and how we fit the data using those models.

#### 3.2.3. Simulations and Mock Spectra

We use simulations of the Ly $\alpha$  forest for two reasons. First, we need to simulate the effect of noise, resolution and the window function due to masking on the power spectrum. Second, we want to connect the information encoded in the power spectrum to a thermal history of the IGM (parametrized by the temperature at mean density  $T_0$ , the slope of the temperature-density relation  $\gamma$  and the pressure smoothing scale  $\lambda_p$ ). For this purpose, one generally needs to run hydrodynamical simulations with different thermal histories. However, these are computationally expensive and at least for the first point we only need a model that is flexible enough to provide a good fit to the observed power spectra, but it need not necessarily provide the correct thermal parameters. Because dark matter (DM) only simulations of the Ly $\alpha$  forest are more flexible and computationally inexpensive to generate, for all the forward modeling in this chapter, we use approximate DM only simulations (a single box with different thermal parameters generated in post-processing) with a semi-numerical approach to paint on the thermal state of the IGM (Croft et al., 1998; Meiksin, & White, 2001; Hui, & Gnedin, 1997; Gnedin, & Hui, 1998; Gnedin et al., 2003; Rorai et al., 2013) This fast simulation scheme allows us to generate a grid of  $\sim 500$  combinations of thermal parameters in a reasonable amount of time.

These DM-based simulations are however, not sufficiently accurate to infer the thermal

### 3. A New Measurement of the IGM Power Spectrum

state of the IGM, as they produce significant biases in thermal parameters when fitted to mock data based on hydrodynamical simulations (see e.g. Sorini et al., 2016, for a detailed comparison between hydrodynamical and dark matter only simulations). They do, however, provide a good fit to the data (compare lines and same color errorbars in Figure 3.6 which we'll discuss in more detail later) and we therefore use them to correct for the window function in our measurement as well as testing our analysis procedure and our fast power spectrum emulator (interpolation scheme, see § 3.2.6). For inference of IGM thermal parameters a grid of hydrodynamical simulations will be used in chapter 4.

For the DM only simulations we use an updated version of the TreePM code described in White (2002) to simulate the evolution of dark matter particles from initial conditions at  $z = 150$  up to  $z = 1.8$ . We use a simulation with  $L_{\text{box}} = 30 h^{-1} \text{ Mpc}$  and  $2048^3$  particles with a Plummer equivalent smoothing of  $1.2 h^{-1} \text{ kpc}$  based on a Planck Collaboration et al. (2014) cosmology with  $\Omega_{\text{m}} = 0.30851$ ,  $\Omega_{\text{b}} h^2 = 0.022161$ ,  $h = 0.6777$ ,  $n_s = 0.9611$  and  $\sigma_8 = 0.8288$ . We do not include uncertainties in cosmological parameters in our models as CMB measurement errors on these parameters (Hinshaw et al., 2013; Planck Collaboration et al., 2016b) are much smaller than current constraints on thermal parameters.

The model is generated for snapshots with  $z$  between 1.8 and 3.4 with a separation of 0.2, the same as our power spectrum measurements, and provides a dark matter density and velocity field. However, the relevant quantities for absorption in the IGM are baryonic density and temperature fields. The results of previous hydrodynamic simulations suggested a computation of the relevant baryonic fields using scaling relations on the dark matter quantities (Hui, & Gnedin, 1997; Gnedin, & Hui, 1998; Gnedin et al., 2003). This basically consists of smoothing the DM density field with a Gaussian kernel to mimic pressure support as well as rescaling the densities to get the right  $\Omega_{\text{b}}$ . Temperatures are then introduced by applying the power law temperature-density relation from eqn. (1.3) to the density field (see Rorai et al., 2013, section 2.2 for the exact procedure).

Given that the UVB is not known perfectly, we created a sequence of models with

### 3.2. Power Spectrum Measurement and Forward Modeling Procedure

different mean transmissions  $\bar{F}$  spanning an  $\sim 5\sigma$  range around the current observational constraints by Becker et al. (2013), Faucher-Giguère et al. (2008b) and Kirkman et al. (2005). This was done by rescaling the optical depths of the full set of skewers to match the desired  $\bar{F}$ . In total we have a parameter grid of  $\sim 500$  different thermal parameter combinations  $(T_0, \lambda_P, \gamma)$  with each of those evaluated for 5 different values of  $\bar{F}$

#### 3.2.4. Forward Modeling Approach

As the observed spectra are much longer than the simulation box we first divided each spectral chunk of  $\Delta z = 0.2$  into regions smaller than our box and assigned a random simulated model skewer to each of the pieces. The skewers were then assumed to fall on the respective position of the spectrum and truncated to have the same length as the spectral chunk. A model of a single real spectrum therefore consists of 4 – 8 simulation skewers. We generated  $\sim 15,000$  skewers of the same length as the simulation box for each parameter combination, therefore we have the equivalent of  $\gtrsim 1900$  mock spectra (or equivalently  $\gtrsim 100$  times our whole dataset) available at each set of parameters. This step is required to enable us to add the wavelength dependent noise and masks to the models.

While the overall mean flux of the box is a free parameter of our models, we renormalize the flux in each pixel of the skewer again to account for the slight redshift evolution of the mean flux along the skewer with respect to the mean flux of the simulation snapshot. To do this the fluxes are converted back to optical depth by  $\tau = -\log(F)$ . We then use the best fit relation to the  $\tau$  evolution by Becker et al. (2013, see eqn. (3.2)) to compute the fractional change in  $\tau_{\text{eff}}$  between box redshift and the individual pixel redshifts and rescaled  $\tau$  at each pixel with the corresponding value. After this we convert back to fluxes. The same mean flux evolution function is then later taken out in the power spectrum computation when we, analogous to our procedure on the data, divide by the mean flux in order to compute the flux contrast. We then convolved these spectra with the respective instrument resolution, and interpolate them onto the same wavelength

### 3. A New Measurement of the IGM Power Spectrum

grid as the observed data. The result of these steps are mock Ly $\alpha$  forest spectra with the same noise properties, spectral coverage, and masking of our data. We henceforth call these the ‘forward models’.

We also compute the power spectrum of the same number of model skewers without any noise, masking, or degradation of resolution which we compare to the power spectrum of our mocks to validate our power spectrum pipeline, and to determine the window function correction. We will henceforth refer to these as ‘perfect models’.

For fitting the BOSS data, there is no need to create full forward models, because all the imperfections our forward model approach treats are already accounted for by the BOSS power spectrum pipeline, and therefore we simply compare the BOSS data to the perfect models.

#### 3.2.5. Covariance Matrix Estimation

In addition to measurements of power spectrum, our statistical analysis requires a covariance matrix. The full covariance matrix consists of  $n_{\text{bins}} \cdot (n_{\text{bins}} + 1)/2$  independent entries where  $n_{\text{bins}} \simeq 15$  is the number of band powers of the wavenumber  $k$ . For a dataset like ours that consists of only  $n_{\text{QSO}} \sim 10$  quasars, this estimate will be extremely noisy. McDonald et al. (2000) did tests on bootstrapped covariance matrices based on spectra that were subdivided into 5 spectral chunks (which then were treated as independent data in the same redshift bin) and concluded that there was still significant statistical uncertainties on the estimates of individual covariance matrix entries. Also Iršič et al. (2017a) tested the bootstrap covariance estimation technique on models with different amounts of skewers. When using only 100 model skewers, which is comparable to the size of their dataset, noise in their correlation matrix is still clearly visible. They also provide a correlation matrix of their measurement that looks similar to this model estimate. As our typical redshift bin has less data available than theirs and as our data is additionally masked for metal absorption, we do not believe that we can estimate reliable covariance matrices from our data (see Figure 3.5 and discussion below). To circumvent

### 3.2. Power Spectrum Measurement and Forward Modeling Procedure

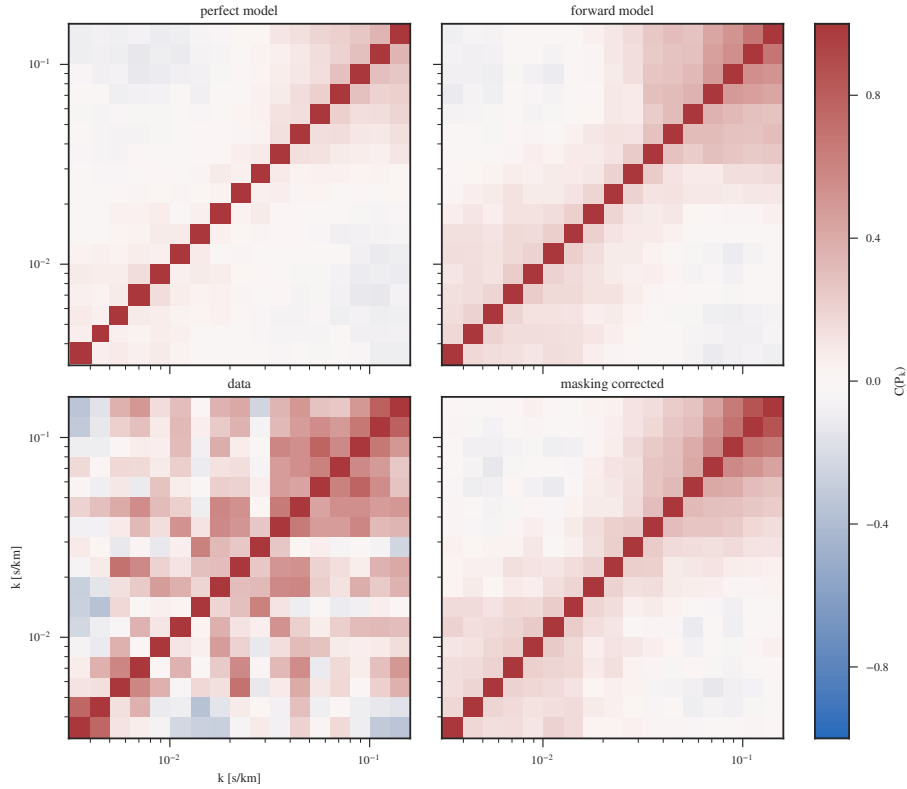


**Figure 3.5.:** The correlation matrices of the non-window corrected, metal-masked Ly $\alpha$ -forest flux power at  $z = 2.8$  as measured from our DM perfect model with parameters close to the best fit (upper left, see § 3.2.7 for how the fit was done), the forward model (upper right) at the same parameters, the data (lower left), and the final masking corrected measurement based on the forward model (lower right, see § 3.2.8 for an explanation about how this was obtained). We can see that the data correlation matrix is far noisier than the others due to the limited data sample size and therefore not usable for model fitting. For the forward model correlations we observe that  $k$ -bins that are close together are mildly correlated ( $\approx 20\%$ ) and bins on very different scales are mildly anticorrelated. For  $k \gtrsim 0.03$  correlations get far stronger due to the power spectrum cutoff as well as the stronger influence of contaminants, e.g. metals, noise and finite spectroscopic resolution. For the perfect model correlations are far weaker except for neighboring  $k$ -bins or bins in the cutoff region. As the exact position of this increase in correlation depends on the power spectrum cutoff position (and therefore e.g. on thermal parameters) we interpolate between correlation matrices when doing model fitting. The final masking corrected correlation matrix looks very similar to the forward model case except for additional correlations in the smallest scale bins due to the masking correction.

### 3. A New Measurement of the IGM Power Spectrum

this problem we use a hybrid approach (in a similar way as Lidz et al., 2006) and only measure the diagonal values  $\sigma_{\text{data}}^2$  of the covariance from the data itself while computing the off-diagonal correlations  $R_{ij}$  from simulations (see § 3.2.3) for which we can obtain sufficient statistics:

$$R_{ij} = \frac{\langle (P_{\text{m, single}}(k_i) - P_m(k_i))(P_{\text{m, single}}(k_j) - P_m(k_j)) \rangle}{\sigma_m(k_i)\sigma_m(k_j)} \quad (3.6)$$

where  $P_{\text{m, single}}$  is the power estimated from a single model skewer,  $P_m$  is its mean over all model skewers,  $\sigma_m$  its standard deviation and the average  $\langle \dots \rangle$  is performed over all model skewers. The covariance matrix is then computed as:

$$C_{ij} = \sigma_{\text{data}}(k_i)\sigma_{\text{data}}(k_j)R_{ij}. \quad (3.7)$$

To estimate the data uncertainties  $\sigma_{\text{data}}$  we use a bootstrapping technique resampling the data. We draw 1000 random sets of quasars with replacement from those contributing to any given redshift bin, and for each compute the power spectrum using eqn. (3.3). For the correlation matrix  $R$ , we use the same mock spectra generated with our forward modeling procedure (the ‘forward models’ in § 3.2.4) to determine the correlation matrix according to eqn. (3.6). No bootstrapping was performed, since for the mocks we have access to different forward modeling realizations of the same dataset. Note that we have a correlation matrix for each model, because the shape of the power spectrum impacts the correlations leading to stronger correlations for modes on scales smaller than the power spectrum cutoff.

In Figure 3.5 we show the correlation matrix for one of our redshift bins determined from the model with parameters closest to our best-fit at this redshift. The typical correlation between neighboring bins is  $\sim 15\%$  and decreases strongly for bins further apart. For comparison, we compute the correlation matrix from our dataset at this redshift as well. This correlation matrix is noisy, and is not used anywhere else in our analysis but is shown here for the sake of illustration. However, one sees that it qualitatively agrees well with our simulated correlation matrix, validating our approach. We also show the correlations of a perfect model and comparing to the forward model

### 3.2. Power Spectrum Measurement and Forward Modeling Procedure

we can see that the additional masking added significant correlations on the 20% level between non-neighboring  $k$ -bins.

We also tested our bootstrap estimation of the diagonal elements of the covariance using random simulated datasets with a size comparable to our measurement dataset that were drawn from our full set of models without replacement. We found that the variance of the power spectrum determined from the ensemble of simulated datasets was in good agreement with the bootstrap estimate obtained from a single mock dataset. Therefore we are confident that our bootstrap estimates of the diagonal elements of the covariance are converged and reflect the actual uncertainties of the power spectrum.

#### 3.2.6. Fast Emulation of Model Power Spectra

To be able to fit the power spectrum measurement we need to create a model for the power in the full region of interest for thermal parameters  $(T_0, \gamma, \lambda_p)$  and the mean transmission of the forest  $\bar{F}$ . As simulations are relatively expensive there is no way to run a full simulation for every combination of thermal parameters at which the power spectrum needs to be evaluated during the fitting process. Therefore we generate a grid of simulations with different thermal parameters (using our semi-numerical DM only simulations) and adopt a fast emulation procedure to compute the power spectrum for parameters between the grid points (in a similar way to what is used for the cosmic calibration framework by Heitmann et al., 2006; 2009; 2013; Habib et al., 2007). Following the procedure described in § 3.2.3, we generated Ly $\alpha$  forest skewers for a grid of thermal parameters  $(T_0, \gamma, \lambda_p)$  and mean flux values  $\bar{F}$ . We computed the power spectrum from perfect skewers generated from these models, as well as for mock data run through the forward modeling pipeline described in § 3.2.4.

For both sets of power spectra (perfect and forward-modeled) we perform a principal component analysis (PCA) of the full set of model power spectra. As result the power at any point  $\theta = \{T_0, \gamma, \lambda_p, \bar{F}\}$  in our model grid can be written:

$$P(k, \theta) = \sum_i \omega_i(\theta) \Phi_i(k), \quad (3.8)$$

### 3. A New Measurement of the IGM Power Spectrum

where both the eigenvectors  $\Phi_i(k)$  and the PCA weights  $\omega_i(\theta)$  are a result of the PCA decomposition. Note that the PCA weights depend on the gridpoints in our model parameter space, and given a suitable interpolation scheme, they can be used to generate model predictions at any point in this space. Along these lines, and following Habib et al. (2007), the PCA weights  $\omega_i$  are then used as an input to train a Gaussian process interpolation scheme. From this Gaussian process we can later evaluate new weights for parameter combinations that lie between or original gridpoints, allowing us to evaluate the power at any location. For more details on this approach see e.g. Rorai et al. (2013) and Habib et al. (2007). The Gaussian process interpolation uses a squared exponential kernel with smoothing lengths chosen to be larger than the separation between model grid points of the parameter space. To speed up computations only the first 9 principal components are actually used for the analysis. We found that the additional errors due to discarding the higher order components is less than 1%.

In general the same approach can be used to emulate models from hydrodynamical simulations, but this means that a separate hydrodynamical simulation must be run for each parameter combination in the grid which is far more costly than the approach we chose for this chapter in which we mostly use the simulation for our window correction. For inference of thermal parameters in chapter 4 we use an improved version of this emulator technique based on hydrodynamical simulations.

#### 3.2.7. Parameter Exploration

To explore the parameter space and fit the measured data power spectra from both BOSS and high-resolution datasets we use a Bayesian Markov Chain Monte Carlo (MCMC) approach with a Gaussian multivariate likelihood:

$$\begin{aligned}
 \mathcal{L} &\equiv P(\text{data}|\text{model}) & (3.9) \\
 &\propto \prod_{\text{datasets}} \frac{1}{\sqrt{\det(C)}} \exp\left(-\frac{\Delta^T C^{-1} \Delta}{2}\right) \\
 &= P_{\text{data}} - P_{\text{emu}}.
 \end{aligned}$$

### 3.2. Power Spectrum Measurement and Forward Modeling Procedure

where  $\mathbf{P}_{\text{data}}$  and  $C$  are the power spectrum and covariance matrix obtained for any dataset, and the product is over all datasets considered (i.e. BOSS and our high-resolution measurement, but including more than two datasets would just add factors to this product). For the high-resolution dataset  $C^{-1}$  is estimated using our hybrid approach (see § 3.2.5) for each model on the parameter grid and therefore is a model dependent quantity. Inside the likelihood computation we use nearest neighbor interpolation in model parameter space to obtain an inverse covariance estimate for each combination of model parameters (which is then just the matrix at the closest model grid point). For the covariance matrix of the BOSS dataset we use the tabulated values from PD+13 which are directly measured from the data, and are therefore model independent. The emulated model power  $P_{\text{emu}}$  is determined for any parameter combination using our emulation procedure. Note that we actually have two distinct emulators, one for the high-resolution data (using the full forward-modeling procedure), and one for the BOSS data (using our perfect simulation skewers).

It is well known that correlated absorption of hydrogen Ly $\alpha$  and Si III at 1206.5 Å leads to a bump in the Ly $\alpha$  forest flux correlation function  $\xi(\Delta v)$  at  $\Delta v = 2271 \text{ km s}^{-1}$  (McDonald et al. 2006; PD+13)<sup>3,4</sup>. This imprints wiggles on the power spectrum with separation  $\Delta k = 2\pi/\Delta v = 0.0028 \text{ s km}^{-1}$ . Following McDonald et al. (2006), we model this contamination with a multiplicative correction to the power

$$P(k) = (1 + a_{\text{Si III}}^2 + 2a \cos(\Delta v k))P_{\text{HI}}(k), \quad (3.10)$$

with  $a_{\text{Si III}}$  being a free nuisance parameter for the strength of the correlation. In previous works this was typically expressed as  $a_{\text{Si III}} = f_{\text{Si III}}/(1 - \bar{F})$  with  $f_{\text{Si III}}$  being a redshift independent quantity that was fit using the entire dataset. We adopt this same parameterization but opt to fit for a unique value of  $f_{\text{Si III}}$  at each redshift. Therefore we have five free parameters  $T_0, \gamma, \lambda_J, \bar{F}, f_{\text{Si III}}$  to fit to our power spectrum measurements in each redshift bin.

<sup>3,4</sup>Note that this correlation should generally be weaker in our high-resolution dataset as we masked some of the Si III absorption.

### 3. A New Measurement of the IGM Power Spectrum

We used the publicly available MCMC package `emcee` (Foreman-Mackey et al., 2013) based on an affine invariant ensemble sampler (Goodman, & Weare, 2010) to sample the posterior distribution:

$$P(\text{model}|\text{data}) = \frac{P(\text{data}|\text{model})P(\text{model})}{P(\text{data})} \quad (3.11)$$

with  $P(\text{data}|\text{model})$  being the combined likelihood of both datasets for a given set of model parameters, and  $P(\text{model})$  being the prior on that combination of parameters. We assume that the priors on parameters are independent, therefore  $P(\text{model})$  is just the product of the individual priors for each parameter. For the thermal parameters we adopt flat priors on  $\gamma$  in the range  $0.5 < \gamma < 2.1$ , on  $\log(\lambda_J)$  in the range  $22 \text{ ckpc} < \lambda_J < 150 \text{ ckpc}$  and on  $\log(T_0)$  in the range  $3000 \text{ K} < T_0 < 20\,000 \text{ K}$ . For the mean flux we adopt Gaussian priors based on the most recent measurements of Becker et al. (2013), Faucher-Giguère et al. (2008b) and Kirkman et al. (2005) (depending on redshift) for  $\bar{F}$ . For the Si III correlations we used a Gaussian prior defined by the best-fit value in  $f_{\text{Si III}}$  and  $1\sigma$  region of Palanque-Delabrouille et al. (2013). All priors for all redshifts are listed in Table 1. Note that as long as a good fit to the data can be obtained (i.e. the model is sufficiently flexible) the exact values of thermal parameters (and therefore also the exact priors chosen) don't matter in the context of this chapter as the fits are only used to correct for the window function as we discuss in the next subsection. Fits were always performed for individual redshifts and no correlation between thermal properties at different redshifts was assumed.

#### 3.2.8. The Raw Power Spectrum and Window Function Correction

The impact of masking on the power depends on the underlying shape of the power spectrum. We use the fits to the underlying power based on our DM models to determine the impact of the window function on this shape. We emphasize here that we use this window-function corrected power mainly for visualization purposes as the covariance

### 3.2. Power Spectrum Measurement and Forward Modeling Procedure

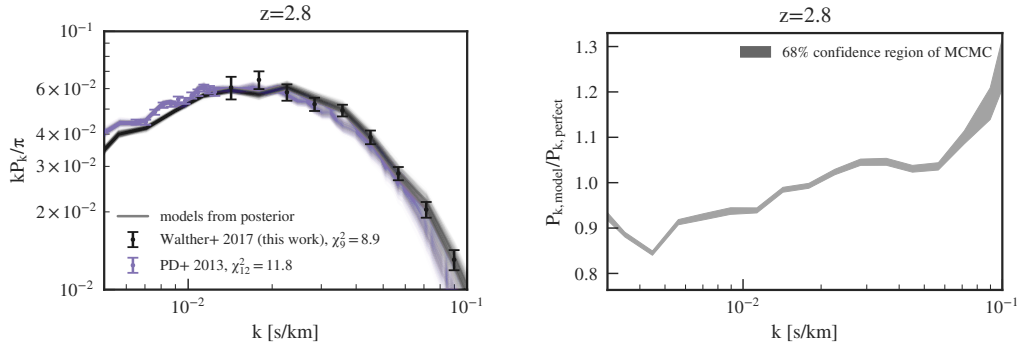


**Figure 3.6.:** Left: The measured power spectrum at redshift  $z = 2.8$  compared to the best-fit. The black points show the raw power of the high-resolution data and are fitted with mock observations including the same noise and masking as in the data. The purple points are showing the PD+13 measurement including their metal, noise and resolution corrections. These are then fitted with models generated from noiseless, non-masked skewers. Lines show models randomly drawn from the posterior MCMC-chain. Right: The window function estimate from a comparison between the power from noiseless, mask-free models and the full forward-modeled mock observations. The band shows the 68 % contour for models drawn from the posterior MCMC-chain. The median is applied as a correction factor to the raw data. The width of the band is propagated into the data errorbars.

in the measurement is subtly changed by the correction. While we do provide an approximate covariance matrix in Appendix D, ideally a full forward model of the power spectrum should be used when doing parameter estimations.

Our measurement, emulation, and window function procedure are illustrated in Figure 3.6. On the left side we show a comparison between our raw data power spectrum (i.e. before window function correction) and the BOSS measurement as points. After applying our fitting procedure we obtain an MCMC chain from which we can draw parameter combinations  $\Theta = \{T_0, \lambda_P, \gamma, \bar{F}, f_{\text{Si III}}\}$  that are compatible with the data. Feeding random draws from this chain into our emulator routines for both the forward model and the perfect model produces the black and purple bands. We can see that these provide good fits to our dataset and the BOSS dataset, respectively. For a single draw  $\Theta$  from the posterior, we can then measure a window function correction  $f_{\text{window}}$  using both

### 3. A New Measurement of the IGM Power Spectrum

emulators as:

$$f_{\text{window}}(k) = \frac{P_{\text{forward model}}(k, \Theta)}{P_{\text{perfect model}}(k, \Theta)}. \quad (3.12)$$

The gray bands on the right side of Figure 3.6 show the resulting 16% and 84% quantiles of this quantity. The dominant effect of windowing our data is a strong increase in power on the small scale ( $k \gtrsim 0.07 \text{ s km}^{-1}$ ) end of the measurement.

To extract the underlying (i.e. window function corrected) power spectrum from our raw measurement we proceed as follows. We generate 1000 random draws from a multivariate normal distribution with a mean given by the raw  $P(k)$  measurement (which includes the effect of the window function) and a covariance matrix defined in eqn. (3.6) (based on both the raw measurement and the best-fit model). We then obtain the window function correction  $f_{\text{window}}(k)$  for 1000 draws from the posterior. By multiplying each  $P(k)$  draw with each  $f_{\text{window}}(k)$  draw we obtain samples of the distribution describing the window corrected measurement. We take the mean of these samples to represent our window corrected power, and the covariance of these samples gives the respective window corrected covariance. We show the resulting correlation matrix applying this procedure at  $z = 2.8$  in Figure 3.5 (lower right panel). Compared to the uncorrected forward model we can see additional correlation at the smallest scales ( $k \gtrsim 0.07 \text{ s km}^{-1}$ ) where the influence of the window correction is strongest. The window function corrected measurements and correlation matrices are tabulated in Appendix D and can be used for comparison with other datasets as well as model fitting. We also provide MCMC chains of  $f_{\text{window}}$  based on our forward models to facilitate reproduction of our measurements.

### 3.3. A New Power Spectrum Measurement

In this section we present our final window-function corrected power spectrum measurements over the redshift range  $1.8 \leq z \leq 3.4$ . First, we discuss the impact of metal line contamination on the power spectrum measurement. Then we compare our power spectrum measurement to the lower- $k$  measurements from BOSS as well as the XQ-100

dataset, which represent the state-of-the-art from low- and medium-resolution data. Finally, we compare our results to previous high-resolution measurements.

#### 3.3.1. The Final Power Spectrum Measurement and the Effect of Metals on the Data

In previous work the effect of metals on the small scale power spectrum has been largely ignored. While McDonald et al. (2000) computed the power spectrum on a dataset with and without metals masked and also considered the effect of masking on the power spectrum, they did not combine both results to see the net-effect of metal contamination. However, they did note that especially for  $k > 0.1 \text{ s km}^{-1}$  the effect of metals as well as noise becomes too strong for their measurement to be usable. Motivated by this conclusion, later measurements by Croft et al. (2002), Kim et al. (2004) and Viel et al. (2008), 2013b also ignored these small scale (larger  $k$ ) modes. For lower resolution measurements using SDSS (McDonald et al., 2006) or BOSS (PD+13) spectra, these modes are well above the resolution limit of the data, and this has not been an issue. Instead, for those measurements the power in metals is estimated from lower redshift data (using a spectral range redwards of the Ly $\alpha$  forest). As this procedure cannot treat metal lines that are always inside the forest large scale correlations between Si III and Ly $\alpha$  are the dominant effect of metal contamination in this case.

In Figure 3.7 we show a comparison between our power spectrum measurement applying the metal masking procedure described in § 3.1.2 and performing the analysis without masking metals. Both measurements have been noise subtracted following the discussion in § 3.2 and corrected for their respective window functions according to § 3.2.8. We also show the BOSS measurement as a comparison, for  $z > 2.2$  where those measurements exist.

It is clear that particularly at small scales ( $k \gtrsim 0.1 \text{ s km}^{-1}$ ) metal lines significantly contribute to the measured power spectrum. This increase in small scale power in general leads to an underestimation of the small-scale thermal cutoff, and naively fitting this

### 3. A New Measurement of the IGM Power Spectrum

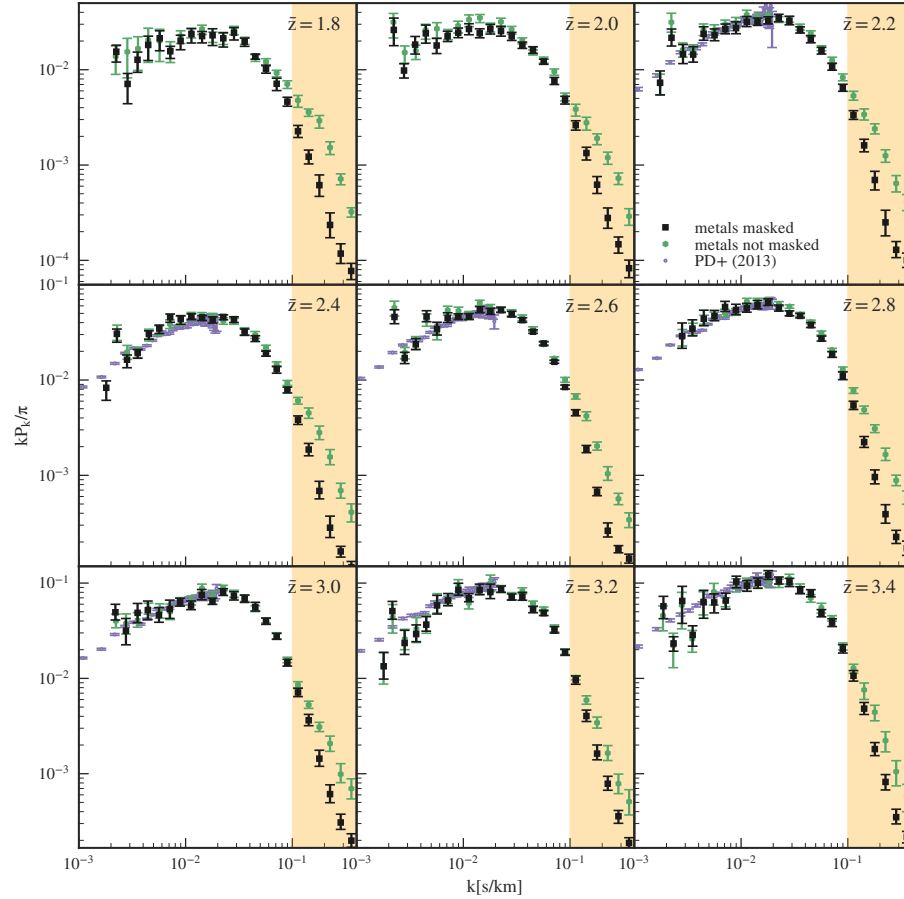


**Figure 3.7.:** Our power spectrum measurement of spectra with masked metals (black squares) and with metals left inside the forest (green hexagons) as well as the BOSS measurement (purple errorbars). Both high-resolution measurements are corrected for their respective window function. In most redshift bins contamination due to metal absorption clearly leads to an increased small scale (large  $k$ ) power which would bias a potential temperature measurement towards lower temperatures. The orange region shows the region excluded in our further analysis as this effect gets far larger than our statistical uncertainties. On larger scales power is removed as well when masking the metal lines leading to an overall better agreement with the BOSS measurement.

### 3.3. A New Power Spectrum Measurement

metal-contaminated power would result in lower overall IGM temperatures (i.e. more small-scale structure and hence less thermal broadening and/or pressure smoothing). For all further analysis we therefore use the metal-masked power (black dots in the figure), and our model fitting is conservatively restricted to modes with  $k < 0.1 \text{ s km}^{-1}$ , where the impact of metal line contamination is relatively weak, and hence our metal-masked power is relatively insensitive to the fact that we may not have masked all of the metals (see discussion in § 3.1.2).

Figure 3.7 also indicates that the impact of metal-line contamination is not restricted to small-scales. Multiple ionic metal-line transitions are typically associated with a given absorber redshift, and because the velocity separations are thousands of  $\text{km s}^{-1}$ , these large-scale velocity correlations can impact the power spectrum on large-scales (low- $k$ ) as well. Masking metals in the data at e.g.  $z=2.6$  decreases this effect lowering the power spectrum and therefore increases the agreement with the PD+13 measurement.

To summarize, metal-line contamination of the power spectrum does not significantly impact our results, given that we mask the metals and conservatively restrict our power spectrum fits to low  $k < 0.1 \text{ s km}^{-1}$  where the impact of residual (i.e. metals we missed in our masking) metal-line contamination should be negligible. In principle, a more careful treatment of metal-lines (i.e. via improved masking, or forward modeling the metals, or subtracting the red-side metal-line power) could allow one to access even smaller scales (higher  $k$ ), although this would also require a very careful treatment of the noise and instrumental resolution whose effect also increases for smaller scales (larger  $k$ ).

#### 3.3.2. Comparison to Previous Low and Medium Resolution Measurements

In Figure 3.8 we show our new metal and window corrected measurement of the high-resolution power spectrum compared to the BOSS measurement from PD+13. Note that different power spectrum bins are correlated and the errorbars only reflect the diagonal elements of the covariance matrix. Where both measurements overlap ( $k \lesssim 0.02 \text{ s km}^{-1}$ ,

### 3. A New Measurement of the IGM Power Spectrum

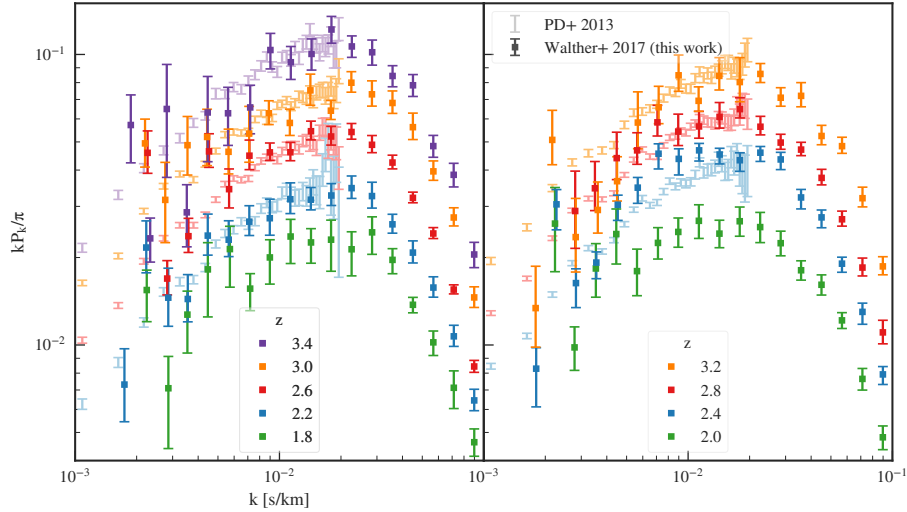


**Figure 3.8.:** Our new measurement of the power spectrum (dark squares) for  $1.8 \leq \bar{z} \leq 3.4$  (different colors), metal lines were masked our analysis and the power introduced by masking was removed using forward modeling of our measurement (see § 3.2.4). Also shown are the measurements of PD+13 (BOSS, bright errorbars on the left). We can see that at most overlapping redshifts there is good agreement except for a mild disagreement with BOSS on large scales (small  $k$ ) for  $z \sim 2.4$ .

$2.2 < z < 3.4$ ) we find good agreement with the high-precision BOSS power spectrum within our errors at modes  $k > 0.01 \text{ s km}^{-1}$  and the agreement is generally good for larger scale (lower- $k$ ) modes as well. The discrepancies at low- $k$  are most likely due to the fact that our measurements are rather noisy for small wavenumbers<sup>3.5</sup>.

We also compare to the recent results of Iršič et al. (2017a) and Yèche et al. (2017) based on the XQ-100 dataset (López et al., 2016). Specifically, Iršič et al. (2017a) measured the power at  $3.0 \leq z \leq 4.2$ , and their redshift bins at  $z = 3.0, 3.2$ , and  $3.4$  match those

<sup>3.5</sup>This is a result of two factors: 1) the density of modes for a one-dimensional power spectrum measurement is uniform, and so for linearly spaced bins there are equal numbers of modes at each  $k$ . However, our  $k$ -bins are logarithmically spaced, so in general our error bars are larger in a relative sense at lower- $k$ . 2) For some of our spectra either limited spectral coverage, or our masking procedure tend to reduce the amount of path length available for measuring the largest scale modes, making them more noisy.

### 3.3. A New Power Spectrum Measurement

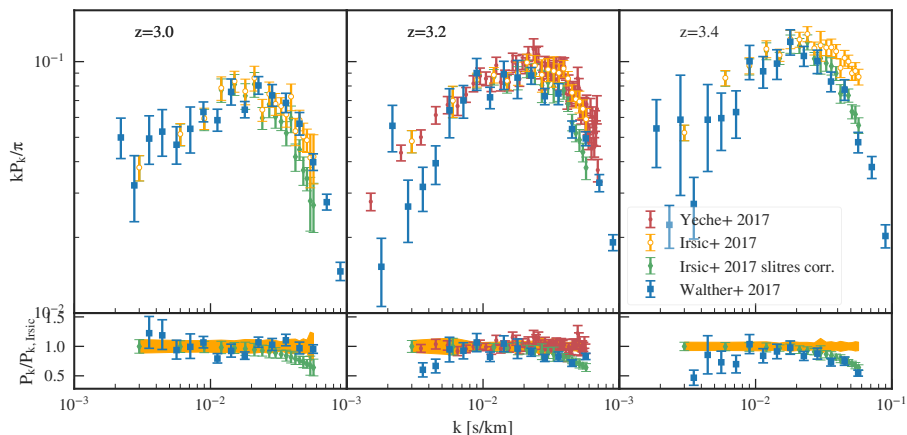


**Figure 3.9.:** Our new measurement of the power spectrum (blue squares) for  $3.0 \leq \bar{z} \leq 3.4$  as in Figure 3.8 compared to the measurements from XQ-100 by Iršič et al. (2017a) (orange open circles) and Yèche et al. (2017) (dark red dots). To address the disagreement at small scales (high  $k$ ) for  $z \geq 3.2$  between our high-resolution and the XQ-100 data, we also show the XQ-100 data of Iršič et al. (2017a) assuming a different resolution correction (see main text for details) by using a distribution of seeings and assuming an underestimation of the X-SHOOTER slit-resolution (green diamonds). The bottom panel shows the same comparison, but normalized by the (untreated) Irsic+2017 measurement. The quoted Iršič et al. (2017a) measurement errors are shown as an orange band.

used in our analysis (Yèche et al. (2017) chose to use broader bins and their  $z = 3.2$  bin can be compared to our results). Those are compared in Figure 3.9.

While the agreement between our measurements at  $z = 3$  is good, at  $z = 3.2$  and  $z = 3.4$  Iršič et al. (2017a) measures  $\sim 10\%$  to  $50\%$  higher power than we do at small scales  $k \gtrsim 0.02 \text{ s km}^{-1}$ , which is clearly statistically significant given the error bars for the respective datasets. Note however that this disagreement is restricted to high- $k$ , and we agree well with Iršič et al. (2017a) at intermediate  $k$  in all redshift bins.

While it is difficult to be certain about the source of this discrepancy, given the different methodology used for measuring the power, the  $k$  dependence of this disagreement provides a very important clue. Note that X-SHOOTER data is significantly lower resolution than the dataset presented here and the resolution corrections become significant at

### 3. A New Measurement of the IGM Power Spectrum

higher- $k$ .

Possible uncertainties of spectroscopic resolution can come from several sources: 1) as X-SHOOTER is a slit-spectrograph its resolution is seeing dependent, so the seeing itself needs to be accurately determined to get an accurate resolution, 2) seeing changes between different observations and correcting assuming a constant resolution across the dataset might bias the measurement (see Appendix A for more details on those points), 3) the UVB slit resolution quoted for X-SHOOTER might be significantly underestimated<sup>3,6</sup> (see Appendix B). Because of those problems, a correction based on the nominal slit resolution can overproduce small scale power in the data analysis. However, Iršič et al. (2017a) already used a higher resolution than provided in the XQ-100 data release paper when performing his corrections<sup>3,7</sup>. Using the Iršič et al. (2017a) value for the resolution leads to agreement between both the XQ-100 power spectrum analyses by Iršič et al. (2017a) and the independent determination of the power spectrum from the same dataset by Yèche et al. (2017). Yèche et al. (2017) determined the spectral resolution by assuming the XQ-100 resolution, and estimating the seeing on object by object basis analyzing the width of the Ly $\alpha$  forest in the spacial direction of the 2d-spectra. While this approach should remove the sensitivity towards seeing, it cannot tackle a potentially misestimated slit resolution or changes of this quantity along the spectral arm. Yèche et al. (2017) also chose to not combine the different spectral arms. Thereby, there shouldn't be a strong change of resolution when reaching the overlap region between both spectral arms. Thus, inside each redshift bin their data should be more homogeneous regarding resolution. Nevertheless, in the end both measurements seem to give essentially the same result.

The influence of resolution errors on the resolution correction factor  $W_R^2$  (see eqn. (3.4))

---

<sup>3,6</sup>Note that the resolution values quoted on the X-SHOOTER webpage were indeed increased since we published this analysis in (Walther et al., 2018a), making this the most likely cause.

<sup>3,7</sup>They used a FWHM resolution of  $50 \text{ km s}^{-1}$  instead of the nominal  $c/R = 69 \text{ km s}^{-1}$  where  $R$  is the quoted resolving power of the X-SHOOTER spectrograph. Communication with the main author revealed that this value was obtained by visual inspection of the raw science data before the official values were available in a similar procedure as in the Yèche et al. (2017) analysis.

### 3.3. A New Power Spectrum Measurement

can be found by simple error propagation:

$$\begin{aligned}\Delta \ln W_R^2 &= -k^2 \Delta(R^2) \\ &\simeq -2k^2 R^2 \Delta \ln(R)\end{aligned}\tag{3.13}$$

and propagates to an error on the estimated power spectrum  $P$  as:

$$\Delta \ln P = -\Delta \ln W_R^2.\tag{3.14}$$

Assuming the nominal resolving power of 4350 (according to López et al., 2016, listing a slightly higher value than the ESO Instrument description) using the X-SHOOTER 1" slit on the UVB arm as a worst case scenario a spectrum with 10% higher resolution than assumed when performing the correction will lead to a  $\sim 45\%$  (28% assuming a resolving power of 5350) overestimate of the power in the resolution corrected measurement. As our own power spectrum measurement is based on  $\sim 10$  times higher resolution data a comparable error in the knowledge of the resolution will have a  $\sim 100$  times smaller effect (so  $\sim 0.4\%$  at  $k = 0.05 \text{ s km}^{-1}$  and  $\sim 1.5\%$  at  $k = 0.1 \text{ s km}^{-1}$ ). Therefore lack of knowledge of the precise resolution of the spectrograph a significant concern for the X-SHOOTER measurement, but can be safely ignored for our study.

To determine the influence of possible errors in the resolution estimates due to points 1 and 2 we divided out the resolution correction from the Iršič et al. (2017a) power spectrum measurement and corrected using different assumptions. First, we used the nominal slit resolution  $R = 4350$  from the X-SHOOTER spectrograph, generated Gaussian distributed seeing values (with a mean of  $0.75''$  and FWHM of  $0.2''$  similar to the distribution shown in Yèche et al. 2017) for each we computed the resolution correction  $W_R^2$  according to eqn. (3.4) and obtained the mean correction which we then used as the new resolution correction. This gives basically identical results (that we don't show in our comparison figure for clarity) to the original Iršič et al. (2017a) measurement showing that the seeing estimate used for their measurement is in agreement with the distribution determined by Yèche et al. (2017) and cannot be the reason for the disagreement with our measurement. In addition we also generate a measurement assuming a higher slit resolution of  $R = 5350$

### 3. A New Measurement of the IGM Power Spectrum

(due to point 3 and in agreement with measurements based on calibration spectra, see Appendix B) and otherwise performing the same analysis. This comparison is shown as red diamonds in Figure 3.9 and we can see that the agreement between our high-resolution measurement and XQ-100 at  $z = 3.2$  and  $z = 3.4$  is good in this case. However, the agreement in the  $z = 3.0$  bin without assuming a different X-SHOOTER resolution correction is unclear, but might be due to possible variations in the resolution between Echelle orders. Note that for the other spectral arms (that cover the Ly $\alpha$  forest for  $z > 3.6$ ) this is a less severe problem as data from those is intrinsically higher resolution. Also note that for those arms one can in principle obtain the resolution of the science observation from the width of telluric absorption lines (see Bosman et al., 2017), but those are rare in the UVB arm. This can also explain the agreement between XQ-100 measurements and older high-resolution data by McDonald et al. (2000) at  $z \sim 3.8$  (but as the redshift bins of both measurements are significantly different, this comparison is tricky) and Viel et al. (2013b) at  $z = 4.2$ .

Because of the severe impact the resolution correction can have on the XQ-100 power spectrum measurement we caution against using the smallest scales ( $k > 0.02 \text{ s km}^{-1}$ ) of this measurement (at least for the lowest redshift bins) for parameter studies. This is especially true for measurements that rely on the accurate determination of the power spectrum cutoff, like e.g. determining the thermal state of the IGM, or the nature of dark matter (e.g. Iršič et al., 2017b; Iršič et al., 2017c; Baur et al., 2017). Although to be fair, for the latter most of the sensitivity comes from the higher redshift ( $z \gtrsim 4$ ) bins where the resolution of X-SHOOTER is higher and additionally high-resolution ( $R \simeq 50,000$ ) data from Viel et al. (2013b) are used.

In Figure 3.4 we can see, that our metal removal and masking correction techniques do not change the data hugely (the difference is covered by our error bars) at the redshifts and scales where we disagree with Iršič et al. (2017a). Additionally, the changes due to metal masking do not exhibit the same shape as the discrepancy. Finally, we also checked the raw power spectra not corrected for any masking and could not get a small-scale power as high as in the Iršič et al. (2017a) result. We are therefore confident of metal

### 3.3. A New Power Spectrum Measurement

masking and window correction not being the reason for the discrepancies.

Our measurements probe the small-scale cutoff in the power ( $0.02 \lesssim k \lesssim 0.1$ ) in all redshift bins with a typical precision of 5 – 15%. The position of this cutoff is still at far larger scales than the expected cutoff due to the spectroscopic resolution of our data and the observed cutoff in the power results from thermal and/or pressure broadening of the absorption lines (or e.g. warm/fuzzy dark matter). In the next subsection we also compare to previous high-resolution measurements to make sure our measurement agrees with existing data on small scales as well.

#### 3.3.3. Comparison to Previous High-Resolution Measurements

Previous power spectrum measurements based on high-resolution data were obtained by different groups using redshift bins of different size and location. They also differ in the Fourier normalization convention used (leading to factors of 2 between some measurements), the field of which the power is computed (flux contrast or transmission leading to additional factors of  $\bar{F}^2$  in the power) as well as whether metals were masked and noise was subtracted. We therefore show comparisons at the quoted redshifts for the old high-resolution measurements and linearly interpolate our results to those redshifts and renormalize the different measurements to the power spectrum convention that we use (see Appendix C).

For authors that chose to study the  $F$  field instead of  $\delta_F$ , there is ambiguity of the mean flux. While the mean flux of the IGM is clearly the same, the mean flux of the data is sensitive to where the continuum is placed. It is well known that hand continuum fits to high-resolution spectra are biased low (Faucher-Giguère et al., 2008a), and this systematic effect is a bigger issue at higher redshift. If one measures the power spectrum of  $F$ , and the continuum fits are biased low, then the power will be biased high. McDonald et al. (2000) provide measurements of their mean flux, and we can therefore easily correct this effect, whereas Croft et al. (2002) does not. Thus a direct comparison to Croft’s measurements is not straightforward, but we do our best by simply assuming their

### 3. A New Measurement of the IGM Power Spectrum

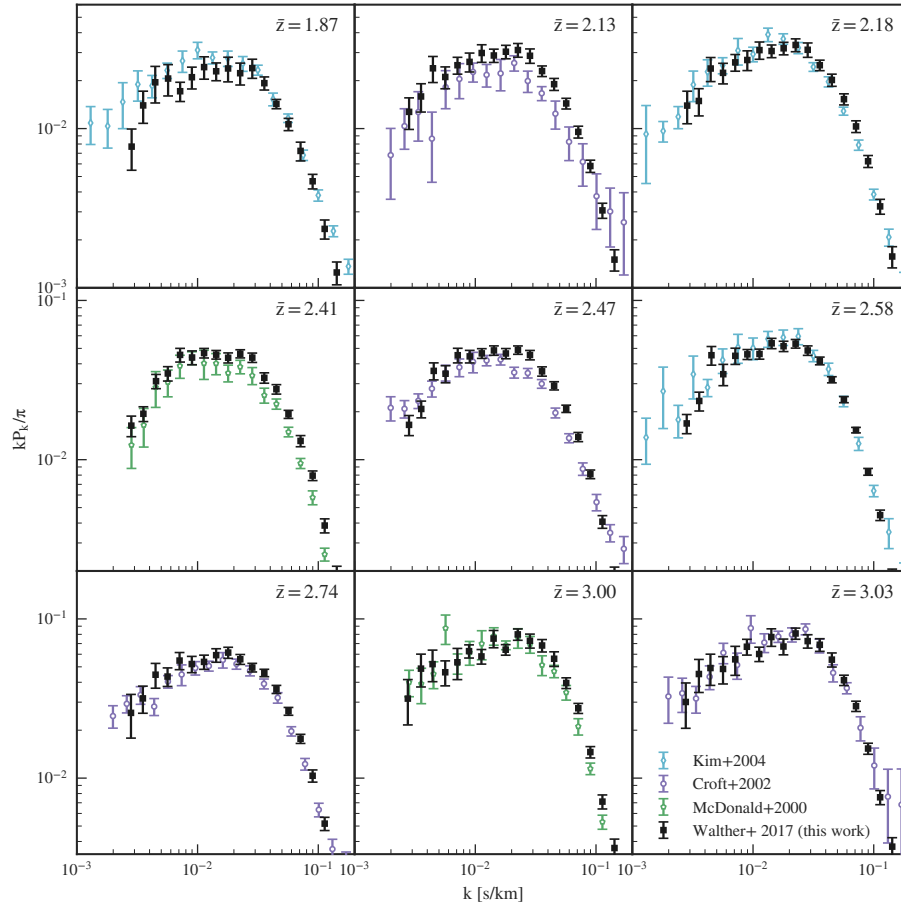


**Figure 3.10.:** Our new measurement of the power spectrum (black squares) compared to the existing measurements of McDonald et al. (2000), Croft et al. (2002) and Kim et al. (2004). Our measurement has been interpolated between the 2 neighboring redshift bins to the same mean redshift as the other datasets. The old measurements by McDonald et al. (2000) and Croft et al. (2002) have been rescaled by  $\bar{F}^2$  as they were obtained on the flux itself instead of the flux contrast  $\delta_F$  which is the cause for different overall normalizations in some bins. The Croft et al. (2002) measurement has been rescaled by an additional factor of two to match the Power spectrum normalization convention we use in this work. It is worth to remark that the older measurements were also performed in wider redshift bins ( $0.3 \lesssim \Delta z \lesssim 0.6$ ). Also Kim et al. (2004) performed their measurement on a subset of our dataset. Notice that the approaches to noise, metal and resolution correction vary between all 4 datasets as well.

continua are unbiased and multiplying in the mean flux of the IGM measured by (Becker et al., 2013) at the respective redshifts of their measurements. The differences between power spectrum conventions clearly limit the precision at which our measurements will agree with previous work.

The comparison between high-resolution measurements is shown in Figure 3.10. While overall agreement is good considering the different approaches, some comparisons show disagreement. The strongest mismatch is with (Croft et al., 2002) at  $z = 2.13$  on all scales. At similar redshifts we agree with both Kim et al. (2004) and PD+13 which hints toward an incorrect mean flux or a problem with the Croft et al. (2002) measurement at this redshift (which is not part of their fiducial sample). We can also see that the shape of the different measurements on scales smaller (larger  $k$ ) than the cutoff matches between the four high-resolution datasets for scales  $0.01 \lesssim k \lesssim 0.08$ . On smaller scales the difference in treatment of metals and S/N of the datasets as well as removal of noise power can probably explain the deviations between these measurements. We do note that our  $z = 3.0$  bin exhibits a cutoff at slightly smaller scales (larger  $k$ ) than the one of McDonald et al. (2000), but agree with Croft et al. (2002) at essentially the same redshift. This shows that there are clear limitations of comparisons to the previous measurements from high-resolution datasets due to the different conventions.

To summarize, we find reasonable agreement between our measurements and previous analyses. We will therefore use our new result for parameter estimations.

### 3.4. Summary

In this chapter we presented a new measurement of the Ly $\alpha$  forest power spectrum at  $1.8 \leq z \leq 3.4$  from archival high-resolution spectra obtained with the UVES and HIRES spectrographs. The pathlength of  $\sim 20$  cGpc covered by this dataset (see Figure 3.4) is several times larger than the previous measurements McDonald et al. (2000), Croft et al. (2002), and Kim et al. (2004). This allows us to measure the small scale cutoff in the power spectrum and its redshift evolution with unprecedented precision.

### 3. *A New Measurement of the IGM Power Spectrum*

We developed a custom pipeline to accurately measure the power spectrum and its uncertainty, which fully corrects finite resolution and noise. Some regions of quasar spectra must be masked because of missing data, DLAs, and metal absorption line contaminants, which we identify and mask using several methods. If left uncorrected, this masking alters the shape of the power spectrum, particularly on the small-scales (high- $k$ ) of interest for studying the thermal state of the IGM. To obtain unbiased estimates of the power spectrum and its associated noise, we adopt a forward modeling approach. We post-process a DM simulation (see § 3.2.3 and § 3.2.4) and generate a grid of different Ly $\alpha$  forest models with the same noise and resolution as our data. The same masks are applied to these mock spectra and we use a custom emulator (§ 3.2.6) to perform MCMC fits (§ 3.2.7) to our measurements. These models are sufficiently flexible that they provide a good fit to the data, although the resulting parameters are not physically meaningful. These model fits are then used to correct our power spectrum and its covariance for the impact of masking (§ 3.2.8). Our analysis shows that metal line contaminants significantly alter the shape of the raw power spectrum on small-scales  $k > 0.1 \text{ s km}^{-1}$ . Although our masking mitigates the effect of this contamination, we nevertheless restrict further analysis of the power spectrum to  $k < 0.1 \text{ s km}^{-1}$ . Our power spectrum measurements in 9 redshift bins covering  $1.8 < z < 3.4$  are tabulated in Appendix D.

We compared our new measurements to previous results from both low-/medium (§ 3.3.2) and high-resolution (§ 3.3.3) spectrographs. Our measurements agree well with the BOSS power spectrum (PD+13) for the low wavenumbers  $k < 0.02 \text{ s km}^{-1}$  probed by that low-resolution dataset. Given the extremely high  $\sim 2\%$  precision of the BOSS study, we consider this an important validation of our approach. Our measurements significantly disagree with the recent study of (Iršič et al., 2017a) based on the medium-resolution XQ-100 dataset. This disagreement is restricted to redshift  $z = 3.2$  and  $z = 3.4$  and is present only for the higher  $k \gtrsim 0.02 \text{ s km}^{-1}$  modes. Given the direction of the discrepancy, and the fact that only the highest  $k$  modes are affected, we argue that the disagreement most likely results from over-correcting the effect of spectral resolution on the power spectrum, which can ultimately be attributed to improper

### 3.4. Summary

characterization of the X-SHOOTER spectrograph's resolution. Comparing our results to previous high-resolution efforts (McDonald et al., 2000; Croft et al., 2002; Kim et al., 2004), we mostly find good agreement, although some combinations of dataset and redshift bin are discrepant at the 10 – 50% level. We do not believe these differences are a significant source of concern, as they likely arise from the challenges in comparing measurements covering significantly different redshift ranges, adopting different mean flux normalization conventions (Appendix C), and other systematics that may have plagued previous work.

In the next chapter we will use the present measurement and combine it with other power spectrum analyses from the literature. The data are then compared to hydrodynamical simulations to perform a measurement of thermal evolution in the IGM.



# 4. A New Measurement of IGM Thermal Evolution at $1.8 < z < 5.4$

In this chapter, we use the power spectrum of the Ly $\alpha$  forest to obtain an accurate self-consistent measurement of IGM thermal evolution over a large redshift range from  $z = 5.4$  to  $z = 1.8$ . As discussed in chapter 2, the power spectrum exhibits a cutoff at small scales (high  $k$ ) beyond which there is no structure left in the Ly $\alpha$  forest. The reason for this is both the smoothness in the baryon density resulting from the finite gas pressure (often called Jeans pressure smoothing) as well as thermal Doppler broadening. The great advantage of the power spectrum compared to other methods, is its sensitivity to structure on a multitude of scales. Specifically, whereas other methods like the curvature (Becker et al., 2011) and wavelets (Lidz et al., 2010) provide only a small-scale measurement of spectral smoothness, the overall shape of the power spectrum for scales between  $\sim 500$  kpc and  $\sim 10$  Mpc as well as small-scale (high- $k$ ) cutoff provides additional constraining power that breaks degeneracies between different thermal parameters<sup>4.1</sup>. For this work we consider  $T_0$ ,  $\gamma$  and the pressure smoothing scale  $\lambda_P$  as thermal parameters and the mean transmission  $\bar{F}$  as a further astrophysical parameter. We additionally marginalize over the strength of Si III correlations and the resolution of the X-SHOOTER spectrograph (see § 4.3.4 for more detailed information about our prior assumptions).

---

<sup>4.1</sup>Note that this property can also be used to break degeneracies with cosmological parameters, e.g. the nature of dark matter (Viel et al., 2013b; Iršič et al., 2017b; Armengaud et al., 2017) or the mass of neutrinos (Palanque-Delabrouille et al., 2015; Yèche et al., 2017; Baur et al., 2017).

#### 4. A New Measurement of IGM Thermal Evolution at $1.8 < z < 5.4$

Our analysis is based upon our recent high-precision measurements of the the small-scale (high wavenumber  $k$ ) the Ly $\alpha$  forest flux power spectrum in chapter 3 as well as other recent measurements from different instruments (Palanque-Delabrouille et al. 2013, hereafter PD+13; Viel et al. 2013b; and Iršič et al. 2017b) combined with the new Thermal History and Evolution in Reionization Models of Absorption Lines (THERMAL) grid<sup>4.2</sup> of hydrodynamical simulations. We then perform inference by employing fast interpolation of our model power spectra and performing an MCMC analysis with a Gaussian likelihood.

This chapter is organized as follows. The measurements we used in this work are summarized in § 4.1. In § 4.2 we present our grid of hydrodynamical simulations. We use modified versions of our forward modeling, interpolation and inference tools from chapter 3, which we present in § 4.3, to measure the thermal state of the IGM at each redshift. In § 4.4 we present these results and compare them to measurements from the literature as well as thermal evolution models. Finally, we discuss the results in § 4.5 and conclude with § 4.6.

### 4.1. Power Spectrum Datasets for Studying IGM Thermal Evolution

In chapter 3 we performed a new measurement of the Ly $\alpha$  forest power spectrum based on 74 archival high-resolution, high-S/N quasar spectra obtained with the VLT/UVES (from Dall’Aglio et al., 2008) and Keck/HIRES (from O’Meara et al., 2015; O’Meara et al., 2017) spectrographs covering a redshift range from  $z = 1.8$  to  $z = 3.4$ . This comprises a significant improvement in dataset size compared to previous measurements based on high-resolution spectra (McDonald et al., 2000; Croft et al., 2002; Kim et al., 2004; Viel et al., 2008) in this redshift range. We semi-automatically masked out possible metal contamination in our data based on several approaches, measured the power spectrum

---

<sup>4.2</sup>see [thermal.joseonorbe.com](http://thermal.joseonorbe.com)

#### 4.1. Power Spectrum Datasets for Studying IGM Thermal Evolution

**Table 4.1:** Different data sets used in this analysis

dataset	$z_{\min}$	$z_{\max}$	$\Delta z$	$N_{\text{qso}}$	$\sim R$	$k_{\max}[\text{s}/\text{km}]$
Palanque-Delabrouille et al. (2013)	2.2	4.2	0.2	11000	2200	0.02
Viel et al. (2013b)	4.2	5.4	0.4	15	60000	0.1
Iršič et al. (2017b)	3.0	4.2	0.2	100	6000–9000	0.05
Walther et al. (2018a)	1.8	3.4	0.2	74	60000	0.1

using a Lomb-Scargle Periodogram (Lomb, 1976; Scargle, 1982) on the flux contrast  $\delta_F = (F - \bar{F})/\bar{F}$ , and binned the resulting power in equidistant bins in  $\log k$ . Statistical uncertainties were estimated using a bootstrap method and are  $\lesssim 10\%$  for the small scale modes that are most sensitive to the thermal state of the IGM.

Additionally, data using the BOSS (Palanque-Delabrouille et al., 2013) or X-SHOOTER (Iršič et al., 2017a; Yèche et al., 2017) spectrographs are available with even smaller statistical uncertainties (e.g.  $\sim 2\%$  on large scales  $k < 0.01 \text{ s km}^{-1}$  for the BOSS dataset), but limited small scale power spectrum coverage due to the significantly lower spectroscopic resolutions of these instruments. As these analyses use the same redshift binning as we do, but extend to higher redshifts  $3.6 \leq z \leq 4.2$  a comparison to them is straightforward. In particular, the BOSS data provides a large scale anchor point thereby partially breaking degeneracies between the different parameters. However, the X-SHOOTER dataset may have significant uncertainty in its resolution estimates which we will take into account in our modeling procedure (see § 4.3.4)<sup>4.3</sup>.

To assess the thermal state at even higher redshifts  $4.2 \leq z \leq 5.4$  (where currently no large survey dataset exists) we use data from the previous high-resolution measurement by Viel et al. (2013b) based on Keck/HIRES and Magellan/MIKE data. This extension

<sup>4.3</sup>This issue was discussed in chapter 3. See also Selsing et al. (2018) who show the dependence of spectroscopic resolution on seeing for the VIS and NIR arms in their Fig. 2 and find both significant scatter as well as overall higher resolution than previously quoted on the ESO webpage.

#### 4. *A New Measurement of IGM Thermal Evolution at $1.8 < z < 5.4$*

allows us to cover a big part of the universes history ( $1.8 < z < 5.4$ ) from just after HI reionization to well after the He II reionization (according to Worseck et al., 2016) and the peak of the cosmic star formation history.

To summarize, our fiducial dataset consists of the data from chapter 3 for  $z \leq 3.4$ , the BOSS data by PD+13 at  $2.2 \leq z \leq 4.2$ , the data by Viel et al. (2013b) at  $z \geq 4.2$ , and the XQ-100 measurement by Iršič et al. (2017a) at  $3.6 \leq z \leq 4.2$  where the VIS arm was used (for  $z = 3.6$  jointly with data from the UVB arm) and except for  $z = 4.2$  no high-resolution dataset was available. A summary of the datasets can be found in Table 4.1.

## 4.2. The THERMAL Suite of Hydrodynamical Simulations

The hydrodynamical models we use in this chapter for comparison with our measurement are part of the publically available THERMAL suite of Nyx simulations (Almgren et al., 2013). Nyx follows the evolution of dark matter simulated as self-gravitating Lagrangian particles, and baryons modeled as an ideal gas on a uniform Cartesian grid. The Eulerian gas dynamics equations are solved using a second-order accurate piecewise parabolic method (PPM) to accurately capture shocks. For more details of these numerical methods and scaling behavior tests, see Almgren et al. (2013) and Lukić et al. (2015).

Besides solving for gravity and the Euler equations, we also include the main physical processes fundamental to model the Ly $\alpha$  forest. First we consider the chemistry of the gas as having a primordial composition with hydrogen and helium mass abundances of  $X_p$ , and  $Y_p$ , respectively. In addition, we include inverse Compton cooling off the microwave background and keep track of the net loss of thermal energy resulting from atomic collisional processes. We used the updated recombination, collision ionization, dielectric recombination rates, and cooling rates given in Lukić et al. (2015). All cells are assumed to be optically thin to ionizing radiation, and radiative feedback is accounted

#### 4.2. The THERMAL Suite of Hydrodynamical Simulations

for via a spatially uniform, but time-varying UVB radiation field given to the code as a list of photoionization and photoheating rates that vary with redshift (e.g. Katz et al., 1992).

The THERMAL suite consists of  $\sim 70$  simulations, each in  $L_{\text{box}} = 20 h^{-1}$  Mpc box and using  $N_{\text{cell}} = 1024^3$  Eulerian cells and  $1024^3$  dark matter particles which is a strong improvement with respect to previous studies of the thermal state which relied on smaller boxes with the same resolution (e.g. Becker et al., 2011). Cosmology is based on a Planck Collaboration et al. (2014) model ( $\Omega_m = 0.319181$ ,  $\Omega_b h^2 = 0.022312$ ,  $h = 0.670386$ ,  $n_s = 0.96$ ,  $\sigma_8 = 0.8288$ ). Comparisons of different resolutions and box sizes can be found in Lukić et al. (2015) and this box size was chosen as the best compromise between being able to run a large grid of models and the need to be converged at least to  $< 10\%$  on small scales (large  $k$ ). The power spectrum is even converged to the one percent level on all relevant scales for  $z \lesssim 3$  and all scales  $k \lesssim 0.05 \text{ s km}^{-1}$  at higher redshifts with respect to resolution. For boxsize, however, the power is converged to the  $\sim 5\%$  level, with the largest scales (smallest  $k < 0.01 \text{ s km}^{-1}$ ) being significantly influenced by poor mode sampling and therefore excluded from our analysis. We further discuss effects of numerical convergence in § 4.5.

For most simulations we generated different thermal histories in a similar way as in Becker et al. (2011) by changing the heating rates relative to a fiducial model at all redshifts and we'll henceforth call these our 'heating rate rescaling models'. The heating rates we used to construct different thermal histories have been constructed as:

$$\epsilon = A\Delta^B \epsilon_{\text{HM12}}, \quad (4.1)$$

where  $\epsilon_{\text{HM12}}$  are the heating rates tabulated in Haardt, & Madau (2012) and  $A$  and  $B$  are the parameters changed to get different thermal histories. Note that while long after any reionization event the instantaneous temperature is more or less independent of the redshift of reionization, the pressure smoothing scale  $\lambda_p$  retains a memory of this for a longer time (Gnedin et al., 2003; Kulkarni et al., 2015; Oñorbe et al., 2017b). As this type of modeling leads to changes in the thermal state at all redshifts, it is hard to disentangle

#### 4. A New Measurement of IGM Thermal Evolution at $1.8 < z < 5.4$

$\lambda_p$  from  $T_0$  and  $\gamma$  from just this approach.

Because of this and to better explore the parameter space we also use a second modeling approach providing completely distinct thermal histories. In this approach we self-consistently solve for the UV background as well as the heating during reionization following the approach laid out in Oñorbe et al. (2017b). Reionization models are parametrized by both a total heat input  $\Delta T$  during reionization and a redshift of reionization  $z_{\text{reion}}$  (at which a species is 99.9% ionized and assuming a fixed shape for the reionization history) for both H I and He II reionization. We also consider the thermal histories based on this approach to be more physically motivated and will later use them to study the implications of our measurements on reionization.

The values for thermal parameters  $T_0$  and  $\gamma$  were obtained from the simulation by fitting a power law TDR to the distribution of gas cells in  $\log \Delta$  and  $\log T$  using a linear least squares method as described in Lukić et al. (2015). To determine the pressure smoothing scale  $\lambda_p$  the cutoff in the power spectrum of the real-space Ly $\alpha$  flux  $F_{\text{real}}$  was fit as described in Kulkarni et al. (2015). Here,  $F_{\text{real}}$  is the flux each position in the simulation would produce (given its temperature and density), but neglecting redshift space effects.

The model parameters were chosen to bracket most current observational constraints on thermal parameters from curvature, wavelet, line-fitting and quasar-pair phase angle statistics. The set of all thermal evolution models used in this chapter as well as the current observational constraints are shown in Figure 4.1. The explicit reionization based models (red curves) show strongly different evolutionary behavior especially in  $T_0$  (most of them show a relatively narrow He II reionization peak around  $z = 3$ ) compared to a relatively smooth evolution for the heating rate rescaling approach (gray curves) and will also be used later as comparison models for our measured thermal evolution.

The combined set of models results in an irregular grid of thermal parameters at each individual redshift. This is shown in Figure 4.2 where each point in the  $T_0, \gamma, \lambda_p$  volume corresponds to one of our hydrodynamical simulations. We can see that a large range is spanned in each of the parameters and most of the 2 parameter combinations. As  $\lambda_p$

## 4.2. The THERMAL Suite of Hydrodynamical Simulations

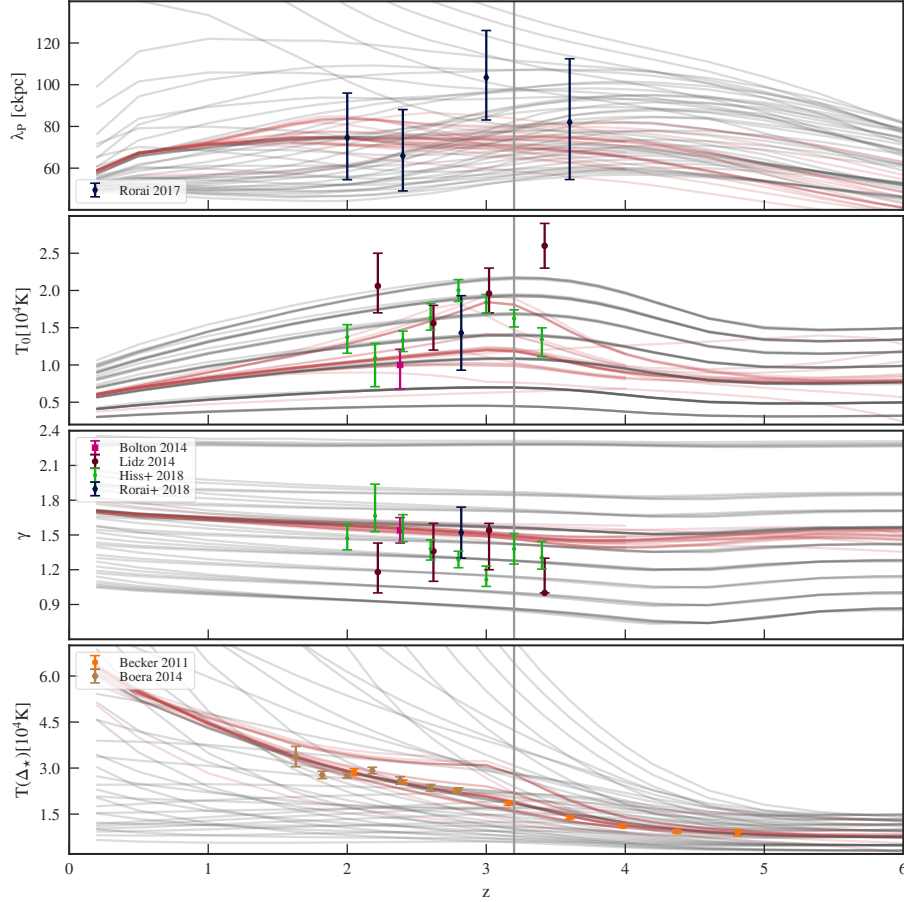


**Figure 4.1.:** Redshift evolution of different thermal evolution models (lines). Most of the different curves (gray) were obtained by changing the overall heating rates from (Haardt, & Madau, 2012) by a factor (changing  $T_0$  at all redshifts) as well as the exponent in their density dependence (changing  $\gamma$  at all redshifts) according to eqn. (4.1). As the pressure smoothing scale  $\lambda_p$  is dependent on the full thermal evolution of the IGM it changes accordingly in these cases. Additional models of thermal evolution (red) with different HI and He II reionization redshifts and heat inputs partially break those degeneracies. Also shown is the Temperature  $T(\Delta_*)$  (based on the values of  $\Delta_*$  by Becker et al., 2011) at the overdensity where constraints from curvature measurements are independent of  $\gamma$ . We compare to the measurements by Lidz et al. (2010), Becker et al. (2011), Bolton et al. (2014), Boera et al. (2014), Rorai et al. (2017b), Hiss et al. (2018) and Rorai et al. (2018) in the parameters constrained by the respective analysis. The Lidz et al. (2010), Bolton et al. (2014) and Rorai et al. (2018) data have been offset by 0.02 along the redshift axis for clarity.

4. A New Measurement of IGM Thermal Evolution at  $1.8 < z < 5.4$

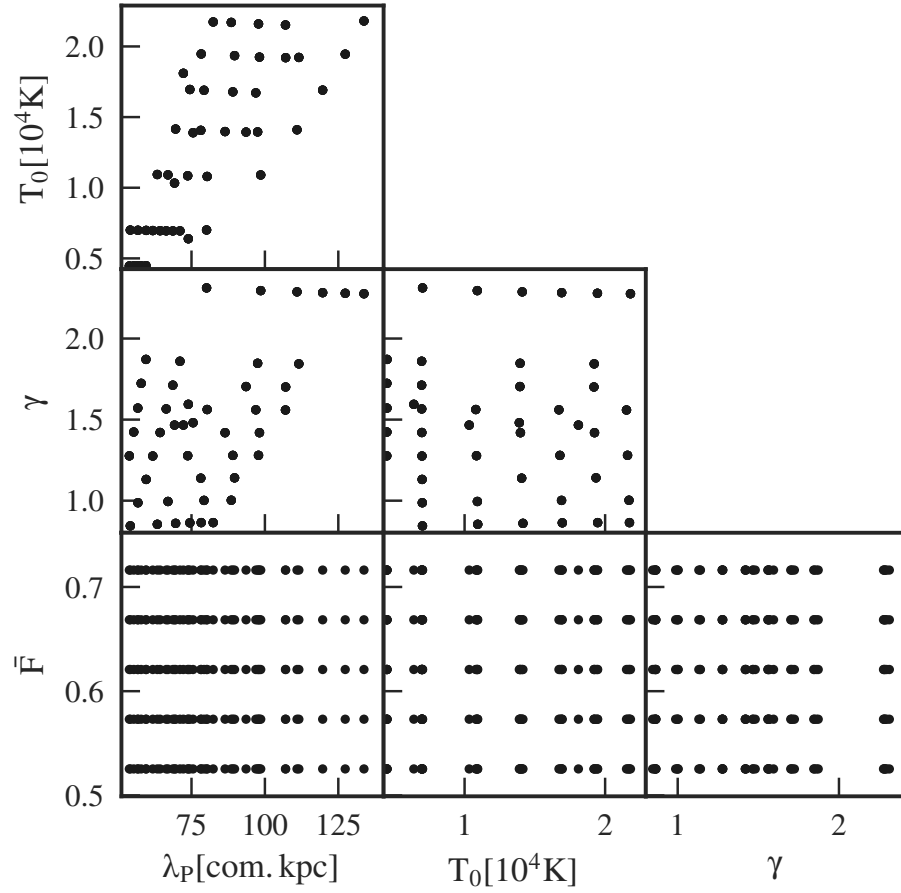


**Figure 4.2.:** The subset of thermal models we used at  $z = 3.2$ . Each point in the  $T_0, \gamma, \lambda_p$  space corresponds to a different Hydrodynamical simulation. Note the correlations between  $T_0$  ( $\gamma$ ) and  $\lambda_p$  in the grid. For each simulation we rescaled the optical depths to obtain outputs with different mean transmitted fluxes  $\bar{F}$ .

#### 4.2. The THERMAL Suite of Hydrodynamical Simulations

probes the integrated thermal history which is smooth for each individual model and partly constrained by physical limits on heating and cooling of the IGM during and after reionization it turns out to be relatively difficult to independently vary  $\lambda_p$  in a way that is not correlated with the thermal state parameters  $T_0$  and  $\gamma$ . Alternatively, one could generate models with abruptly changing temperature such that the pressure smoothing does not have enough time to follow this change. While arbitrary  $\lambda_p$  could be generated in this way, fine-tuning is needed to produce this kind of model for an individual redshift which would take a lot of additional computational time (especially for changes at low redshifts) and it also seems unphysical. Therefore, we do not have full flexibility (mostly due to CPU time restrictions) in varying  $T_0$  vs.  $\lambda_p$  orthogonal to the degeneracy direction visible in our models. However, this in the end does not pose a problem to our analysis as the correlation between both parameters is physically motivated.

In principle reionization is an inhomogeneous process (Davies, & Furlanetto, 2016; D’Aloisio et al., 2015), but we only use an homogeneous model to describe photoionizations. While generally UVB and thermal fluctuations could be influencing the power spectrum and therefore our conclusions on thermal evolution especially at  $z > 4$  (see e.g. Cen et al., 2009), recent analyses (Onorbe et al. 2018a, also earlier studies by McDonald et al. 2005a and Croft 2004 obtained similar results but with a focus on lower redshifts) have found that those mostly change the power spectrum on larger scales than used for this work (at least for HI reionization), but does not strongly change the power on small scales which provides most of the sensitivity to the thermal state of the IGM. Note again that we are not using the largest scale modes which strongly reduces our sensitivity to inhomogeneities, further justifying our use of a homogeneous UVB.

We computed skewers of optical depth  $\tau = -\ln F$  by convolving each pixel along one dimension in the simulation box with the corresponding Voigt-profile for the Temperature  $T$ ,  $N_{\text{HI}} \propto \Delta^2 / (T^{0.7} \Gamma_{\text{HI}})$  and Doppler shifts due to  $v$  for each simulation snapshot. As is common in Ly $\alpha$  forest studies (see e.g. Bolton et al., 2010b; Boera et al., 2014), the obtained values of  $\tau$  were then rescaled to match different mean transmission values  $\bar{F}$  to compensate for our lack of knowledge of the UVB amplitude. Generally this rescaling

#### 4. A New Measurement of IGM Thermal Evolution at $1.8 < z < 5.4$

will affect the shape and large scale amplitude of the power spectrum. Lukić et al. (2015) investigated this issue (see their Figure 23) and found that rescaling  $\tau$  by a factor of  $\sim 0.5$  results in to  $\sim 5\%$  changes in the Ly $\alpha$  forest power spectrum, especially at low redshifts. While rescaling  $\tau$  could be slightly biasing our results, we emphasize that the rescalings we perform in this work are typically smaller  $\Delta\tau/\tau \sim 30\%$ , and hence this effect should be subdominant compared to e.g. boxsize effects and cosmic variance (see § 4.5).

For each redshift and each parameter combination  $\theta = \{T_0, \gamma, \lambda_P, \bar{F}\}$  we generated 50000 randomly selected skewers – the same ones for each parameter combination – which serves as the starting point of our analysis.

### 4.3. Measuring the Thermal State of the IGM

In this section, we describe how we perform inference on our data using the THERMAL grid. This involves generating a forward model of the data, creating an emulator – a fast method to interpolate from a sparse grid of simulation to any point in the multi-d parameter space, and finally performing the actual inference via Bayesian methods.

#### 4.3.1. Forward Modeling

To compare to existing measurements, which didn't apply masking of spectral regions, but instead treated metal contamination statistically by comparing to lower redshift data where most metals are outside the Ly $\alpha$  forest, we compute the power spectrum based on  $\sim 50000$  noiseless, high-resolution skewers from our simulation. We will refer to this as the 'perfect model'.

However, due to fully account for the window function introduced on the power spectrum by masking parts of the data, when comparing to our measurement from chapter 3, we compute the power spectrum based on the skewers for each combination of parameters applying the full forward modeling technique described in chapter 3 to our hydrodynamical simulations. Henceforth we'll call this the 'forward model'. This

### 4.3. Measuring the Thermal State of the IGM

technique consists of several steps of post-processing the hydrodynamical simulation outputs followed by a power spectrum computation in the same way as for the data. To forward model an individual quasar spectrum we first merge randomly selected skewers (without repetition) to cover the same pathlength as the data, then convolve the spectra with a Gaussian smoothing kernel reducing the resolution of the models to match that of the data, rebin the models onto the pixels of the observed spectra, and add noise drawn from a Gaussian distribution for each individual pixel with a standard deviation equal to the  $1\sigma$  uncertainty of the corresponding quasar spectral pixel reported by the data reduction pipelines. Finally and most importantly, we mask the forward modeled spectrum in exactly the same way as the data to account for the windowing effects resulting from gaps in the data and our metal masking procedure. We then compute the power spectrum by utilizing  $\sim 50000$  skewers from our simulation. Note that while the full forward modeling of noise and resolution might not be completely necessary as they have been corrected in the measurement (and are corrected in the same way inside the forward modeling procedure as well), there might be subtle effects on the masking correction. We therefore want to make the model spectra as similar to data as possible. Note that this does not change our model precision which is dominated by dataset size rather than noise or resolution.

#### 4.3.2. Emulation of the Power Spectrum

To perform a fit to the data and infer the thermal state at a particular redshift we need to be able to compute power spectra on a continuous range of parameters. Therefore we need to interpolate between the discrete and sparse outputs of the THERMAL grid. To perform this task we follow the emulation approach of Heitmann et al. (2006) and Habib et al. (2007). For details, we refer the reader to their papers (and references therein) as well as chapter 3; in the following we summarize the main steps of the approach. First, we decompose the simulated logarithmic power spectra onto a PCA basis. We save the PCA vectors  $\Phi_i(k)$  as well as the coefficients  $\omega_i(\theta_j)$  at each thermal model location  $\theta_j$ .

4. A New Measurement of IGM Thermal Evolution at  $1.8 < z < 5.4$

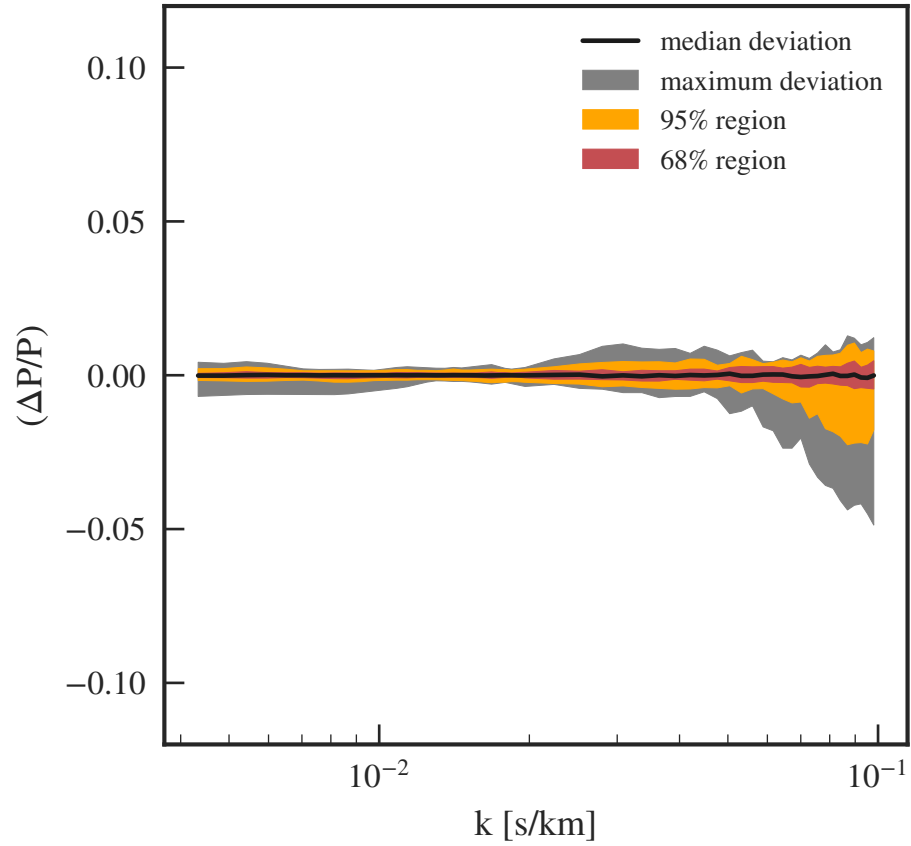


**Figure 4.3.:** Cross validation results for our emulation procedure at  $z = 2.8$ . Colored bands are showing the relative difference between emulated and true power for different cuts of the full cross validation set. The median is shown as a black curve. Other redshifts give similar results especially for the 68% region. See main text for more details.

### 4.3. Measuring the Thermal State of the IGM

We then use a Gaussian process to interpolate the coefficients  $\omega_i(\boldsymbol{\theta}_j)$  onto any arbitrary location in parameter space  $\boldsymbol{\theta}$ . Taking the dot product of the PCA vectors with these interpolated coefficients then gives the power spectrum evaluated at any parameter location.

We thus calculate a Gaussian process (GP) for each principal component coefficient (using GEORGE, see Ambikasaran et al., 2016) using a squared exponential kernel plus an additional white noise contribution

$$K(\boldsymbol{\theta}_i, \boldsymbol{\theta}_j) = \exp(-0.5(\boldsymbol{\theta}_i - \boldsymbol{\theta}_j)^T C_l^{-1} (\boldsymbol{\theta}_i - \boldsymbol{\theta}_j)) + \sigma_n \delta_{ij} \quad (4.2)$$

for parameter values  $\boldsymbol{\theta}_i$ , a chosen distance metric  $C_l$  (which is defined by a smoothing length  $l$  for each parameter, i.e. it's diagonal) and a noise contribution  $\sigma_n$  (for an in depth introduction to GP techniques, see Rasmussen, & Williams 2005).

As the hydrodynamical grid consists of far less models ( $\sim 50$ )<sup>4.4</sup> than the previous DM based grid ( $\sim 500$ ) used in chapter 3, we must be more careful about the interpolation errors resulting from our emulation procedure. Instead of just using a kernel with a fixed hand-tuned smoothing length, which was our approach in chapter 3, we additionally optimized our kernel parameters by maximizing GP-likelihood using the `scipy.optimize` (Jones et al., 2001–) package and the so-called L-BFGS-B (Zhu et al., 1997) method<sup>4.5</sup>. We then performed the analysis using the optimal smoothing lengths  $l$  and noise  $\sigma_n$  for the kernel for each Gaussian process emulator.

We estimate the emulation uncertainties using a cross-validation scheme to propagate interpolation errors. To do this we generate the emulator, but leave one simulation out of the training set<sup>4.6</sup>. We denote emulators with a model (defined by parameters  $\boldsymbol{\theta}$ ) left out as `emu \setminus \boldsymbol{\theta}`. We then compare the actual models (with power  $P_{\text{model}}$ ) for this simulation to

<sup>4.4</sup>The exact number of models used is redshift dependent because of further cuts that are discussed at the end of this subsection.

<sup>4.5</sup>If a low likelihood was achieved we optimized again using the downhill simplex method by Nelder, & Mead 1965 and took the more optimal of the 2 runs.

<sup>4.6</sup>In fact we discard all the different  $\bar{F}$  realizations for this simulation in this test as they all have the same thermal parameters.

#### 4. A New Measurement of IGM Thermal Evolution at $1.8 < z < 5.4$

the emulator (with power  $P_{\text{emu}|\theta}$ ) at the parameters  $\theta$  of this model:

$$\Delta P_{\text{emu}}(\mathbf{k}, \theta) = P_{\text{model},\theta}(\mathbf{k}) - P_{\text{emu}|\theta}(\mathbf{k}, \theta). \quad (4.3)$$

We show the accuracy of the emulation in Figure 4.3. This shows quantiles of the deviations  $\Delta P_{\text{emu}}$  from the true underlying model inside our cross-validation sample. We see that for most models in our parameter space the emulator works to better than 1%. However, emulation uncertainty can increase to the 5% level (with a preference for underestimation at  $k > 0.06 \text{ s km}^{-1}$ ) for some models. As the uncertainty in our power spectrum measurements is  $\sim 2\%$  (for the 68% quantile) on large scales ( $k \lesssim 0.01 \text{ s km}^{-1}$ ) and  $\gtrsim 5\%$  on smaller scales, measurement errors are much larger than these interpolation errors. Nevertheless, we opted to add the covariance matrix for the interpolation process to our likelihood. This covariance matrix can be obtained by performing:

$$C_{\text{emu},ij} = \langle \Delta_{\text{emu}}(\mathbf{k}_i, \theta) \Delta_{\text{emu}}(\mathbf{k}_j, \theta) \rangle \quad (4.4)$$

with the average performed over all possible combinations of model parameters inside our grid for each redshift bin.

Due to the variety of thermal histories in the THERMAL suite some simulations can have extremely close values of their thermal parameters at some specific redshifts. In order to avoid possible problems in the emulator due to this issue we removed models from the THERMAL grid that did not satisfy a distance threshold<sup>4.7</sup> and are left with 45 to 65 models per redshift.

### 4.3.3. Inference

We perform a Bayesian MCMC analysis on the power spectrum data at each individual redshift using the `emcee` package (Foreman-Mackey et al., 2013) based on the affine

---

<sup>4.7</sup>To be precise we demand  $\sqrt{\sum_{\theta \in \theta} \left( \frac{\theta_i - \theta_j}{\max(\theta) - \min(\theta)} \right)^2} \geq 0.1$ , i.e. applying a minimal distance that is still far closer than our typical grid separation. While this threshold leads to good results throughout our redshift range, it is not necessarily the optimal one and further tests adopting different values could therefore be used to slightly increase interpolation accuracy.

### 4.3. Measuring the Thermal State of the IGM

invariant sampling technique (Goodman, & Weare, 2010) and again assuming the multivariate Gaussian likelihood (see eqn. (3.9)), but now accounting for our emulation covariance  $C_{\text{emu}}$  by adding it to the data the covariance of an individual measurement  $C_{\text{data}}$  to get the full covariance  $C$  for the likelihood, i.e.:

$$C = C_{\text{data}} + C_{\text{emu}}. \quad (4.5)$$

For these covariances we use published values if available. For our own dataset from chapter 3 as well as the Viel et al. (2013b) dataset, we used the published uncertainties (i.e. the diagonal covariance elements) and combined them with the correlation matrix of the model closest in parameter space to obtain an estimate of the covariance, i.e. we perform nearest neighbor interpolation between covariance matrices obtained at every point (see chapter 3 for details on this approach).

#### 4.3.4. Parameters and Priors

Our modeling so far depends on 4 parameters,  $T_0$  and  $\gamma$  describing the thermal state,  $\lambda_p$  for the pressure smoothing depending on the full thermal history, and  $\bar{F}$  for the mean transmission that corresponds to a given UVB amplitude. There is, however, one additional parameter that we input in our models for each dataset to generate the observed correlation between Si III and Ly $\alpha$  (see McDonald et al., 2006; Palanque-Delabrouille et al., 2013). Finally, because of significant uncertainties in the resolution of the XQ-100 data (see the detailed discussion in Appendix B of chapter 3), we also marginalize over the resolution of the XQ-100 measurement whenever we use this data, giving us another parameter. Therefore we have a total of 5 (in the case of high-resolution data only) to 8 (in the case of fitting 3 datasets of which one comes from XQ-100) parameters. We assume flat priors on  $\log T_0$ ,  $\log \lambda_p$ ,  $\gamma$ . We now go into further detail about the modeling and assumptions for the other parameters.

We add Si III correlations to the model analytically by multiplying the model power spectrum with an oscillating signal as correlations inside a spectrum correspond to

#### 4. A New Measurement of IGM Thermal Evolution at $1.8 < z < 5.4$

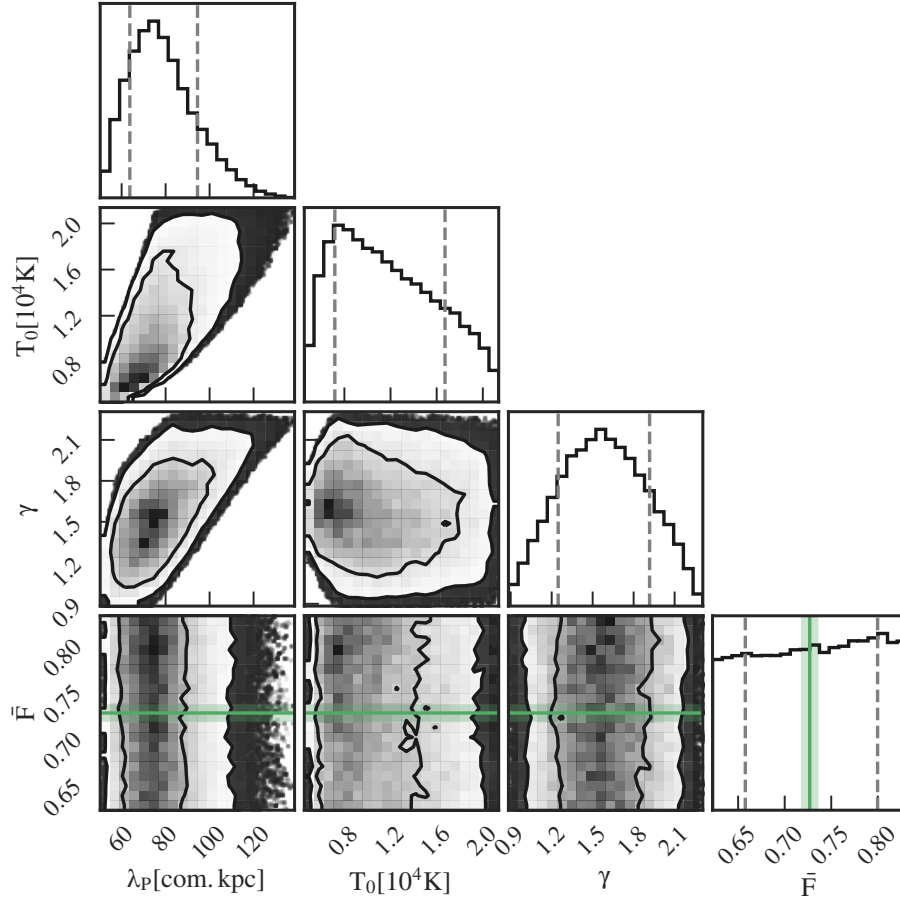


**Figure 4.4.:** Corner plot showing the Prior PDF for thermal parameters and  $\bar{F}$  given our model grid and excluding parameter values outside its convex hull. This was obtained by sampling our prior with an MCMC assuming a flat likelihood. Note that the degeneracies in our model grid lead to non-flat marginalized distributions. The diagonal shows the 1d-PDF (marginalized over all other parameters) for each parameter with dashed vertical lines at the 16% and 84% quantiles. The scatter plots below show the 2d-PDFs for each combination of 2 parameters (also marginalized over all others) with contours showing the region containing the 68% and 95% highest densities. Note that due to the restrictions of our grid there is a strong correlation especially between  $T_0$  and  $\lambda_P$ . The additional preference towards low  $T_0$  or  $\lambda_P$  is due to our choice of flat priors in the log of these parameters. The green band shows the  $1\sigma$  interval in  $\bar{F}$  we use for the Gaussian prior.

### 4.3. Measuring the Thermal State of the IGM

oscillations of the corresponding power spectrum:

$$P_{\text{tot}} = (1 + a_{\text{Si III}}^2 + 2a \cos(k \Delta v))P_{\text{HI}} \quad (4.6)$$

with  $a_{\text{Si III}}$  being a free nuisance parameter for the strength of the correlation. In previous works this was typically expressed as  $a_{\text{Si III}} = f_{\text{Si III}}/(1 - \bar{F})$  with  $f_{\text{Si III}}$  being a redshift independent quantity that was fit using the entire dataset. We adopt this same parametrization but opt to fit for a unique value of  $f_{\text{Si III}}$  at each redshift and for each dataset because of the different metal treatment in the datasets and as we do not perform a joint fit of different redshifts here. We assume a flat prior on each  $f_{\text{Si III}}$  and demand correlations to be positive.

We modeled the resolution of the X-SHOOTER spectrograph  $R_{\text{new}}$  by multiplying the measured XQ-100 power spectrum with the resolution dependent part of the window function:

$$W_R(k, R) = \exp\left(-\frac{1}{2}(kR)^2\right) \quad (4.7)$$

using the resolutions quoted in Iršič et al. (2017a) and dividing by  $W_R(k, R_{\text{new}})$ . Note that the resolution of the instrument depends on two different factors: the resolution for a fully illuminated slit (or "slit resolution") and the seeing which gives rise to higher spectral resolution if smaller than the slit size. We assume two limits for the resolving power of the XQ-100 dataset. The lower limit assumes the slit resolutions quoted in the XQ-100 data release paper (López et al., 2016) as well as a fully illuminated slit (leading to  $R_{\text{UVB}} = 4350$  for the UVB arm of the instrument,  $R_{\text{VIS}} = 7410$  for the VIS arm<sup>4.8</sup>). The upper limit assumes a seeing of 0.65" (smaller than the slit) and higher values for the slit resolution<sup>4.9</sup> (leading to  $R_{\text{UVB}} = 8230$  and  $R_{\text{VIS}} = 12184$ ). We assume a flat prior between these two limits. As  $z = 3.6$  is using both spectral arms we use the lowest and highest of the 4 resolution values above as the limits here. Note that this choice of priors

<sup>4.8</sup>These values are also close to the formerly quoted "new values" from the instrument website as well as manuals until Period 101.

<sup>4.9</sup>Based on our on estimates of XSHOOTER's resolution in chapter 3 which is also close to the recently updated values on the XSHOOTER website and manual from Period 102

#### 4. A New Measurement of IGM Thermal Evolution at $1.8 < z < 5.4$

on spectroscopic resolution is an extremely conservative choice that will significantly weaken the constraints that can be obtained from this XQ-100 dataset. This is most acute in the UVB arm because of its intrinsically lower resolution. A more careful analysis of the XQ-100 resolution would allow us to adopt a far stronger prior on these values, which would increase the precision of constraints deduced from power spectra measured from such moderate resolution spectra.

Note that most previous measurements (exceptions to this are e.g. Lidz et al., 2010; Iršič et al., 2017b) of the IGMs thermal state did not attempt to marginalize over the uncertainty in the mean flux estimate. Instead, typically simulations that match the mean flux of the data assuming perfect knowledge of this quantity are used (e.g. in Voigt profile fitting or curvature analyses). For  $\bar{F}$  we used both a flat prior (corresponding to performing a joint measurement of  $\bar{F}$  and the thermal state) and a Gaussian shaped prior. For the Gaussian prior we assumed a mean based on the fit by Oñorbe et al. (2017b) to a compilation of recent measurements (Fan et al., 2006a; Kirkman et al., 2007; Faucher-Giguère et al., 2008b; Becker et al., 2013) and a standard deviation based on the uncertainties for the most recent measurements at  $z \leq 4.0$ : Becker et al. (2013) for  $2.2 \leq z \leq 4.0$ , Faucher-Giguère et al. (2008a) for  $z = 2.0$ , Kirkman et al. 2005 for  $z = 1.8$ . For  $z \geq 4.2$  we use  $\sigma_{\bar{F}} = 0.03$  which is loosely based on the discrepancy between Fan et al. 2006a for  $z \geq 4.6$  and the measurements by Becker et al. 2011 in the range  $4.1 \leq z \leq 4.7$  (see also Bosman et al., 2018; Eilers et al., 2018, for more recent mean flux measurements that are discrepant by a similar amount for  $5.0 \leq z \leq 5.4$ ).

To avoid extrapolating from our model grid we additionally require that all thermal parameters lie inside the convex hull of our model grid (see Figure 4.2), i.e. the smallest convex shape including all THERMAL grid points. The convex hull is evaluated numerically by triangulating the model grid (using `scipy.spatial.Delaunay`) and for each MCMC sample we test whether it is inside the triangulation when evaluating the prior. Otherwise the prior is set to zero. To see the effective prior resulting from only using this non-rectangular region where we have models, we performed an MCMC run assuming a completely uninformative dataset, i.e. using only the priors in our fit and a

constant likelihood. The results of this procedure are shown in Figure 4.4 for  $z = 2.8$ . In some contours, e.g.  $T_0$  and  $\lambda_P$ , we can see that parameters are highly correlated already since our grid is non-rectangular. We argue, however, that these correlations are physically motivated as models perpendicular to these correlations are hard to produce (see § 4.2) and that this behavior actually constitutes prior information for our analysis.

## 4.4. Thermal Evolution of the IGM

### 4.4.1. Measurements and Degeneracies

We performed fits of the parameters governing the thermal state using combinations of all datasets discussed in § 4.1 in 16 individual redshift bins with  $1.8 < z < 5.4$ , where we used a bin size  $\Delta z = 0.2$  for  $z \leq 4.2$  and  $\Delta z = 0.4$  for  $z \geq 4.6$ .

The power spectra of each dataset are summarized and compared to models based on our posterior MCMC chains in Figure 4.5. Note that for visualization purposes we only compare window-function, Si III correlation and resolution corrected data to the perfect model. The window function due to masking was taken out of the UVES/HIRES data by multiplying measurement points with the median  $P_{\text{emu,perfect}}/P_{\text{emu,forward}}$  for our MCMC chain and propagating its uncertainties using Gaussian error propagation for each individual mode § 3.2.6<sup>4.10</sup>. Analogously, we rescaled the XQ-100 power to use the "best-fit" resolution correction, i.e. we renormalize with  $W_R(k, R_{\text{new}})/W_R(k, R)$  (see eqn. (4.7)) from the posterior and removed Si III correlations from the data applying eqn. (4.6). We can see that satisfactory fits have been achieved at all redshifts.

In Figure 4.6 we further illustrate the posterior distribution we infer via our MCMC at  $z = 2.8$  with a so-called 'corner plot'. We can see that the data strongly constrains all parameters (e.g. compare to Figure 4.4 or the blue curves in the 1d histograms, for which the likelihood is assumed to be completely uninformative). The most important feature

<sup>4.10</sup>Note that while we used DM models to correct the "raw" power in chapter 3, the masking correction performed here is fully based on hydrodynamical simulations

#### 4. A New Measurement of IGM Thermal Evolution at $1.8 < z < 5.4$

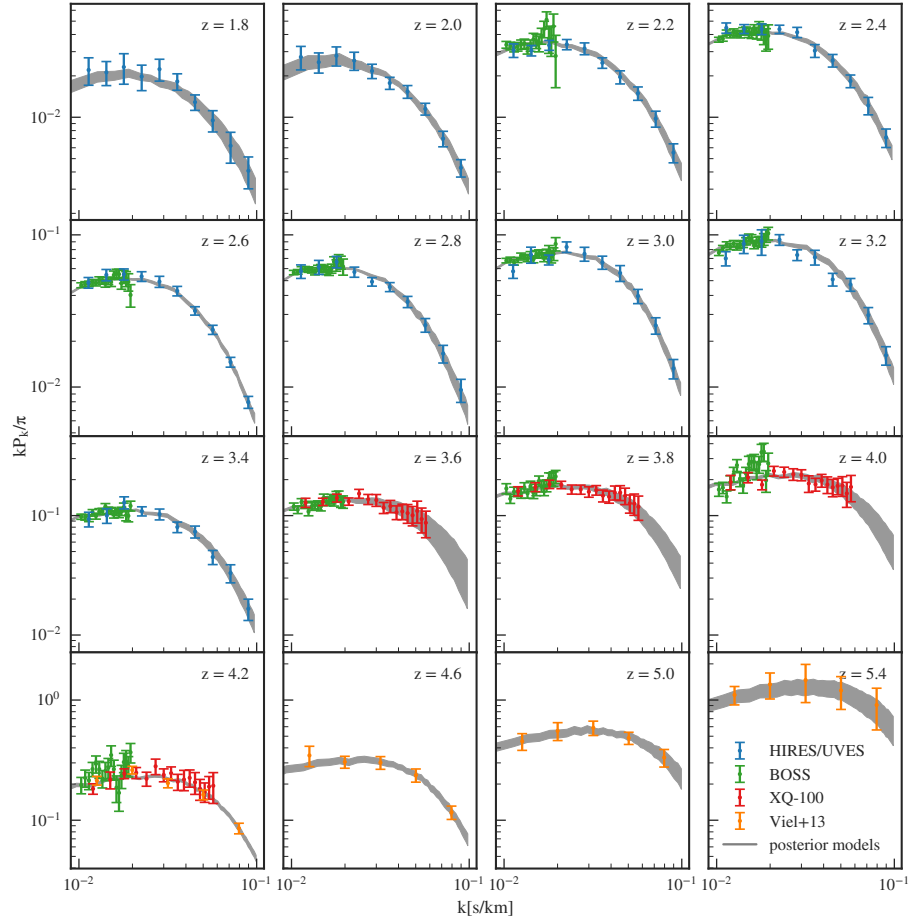


**Figure 4.5.:** Redshift evolution of the power spectrum with colors showing different datasets. Data by Iršič et al. (2017a) were corrected to the median of the marginalized posterior resolution, Walther et al. (2018a) points have been corrected for the masking window function. All data have been corrected for Si III correlations. Bands show 68% confidence regions for our emulator with parameters randomly drawn from the posterior distribution.

#### 4.4. Thermal Evolution of the IGM

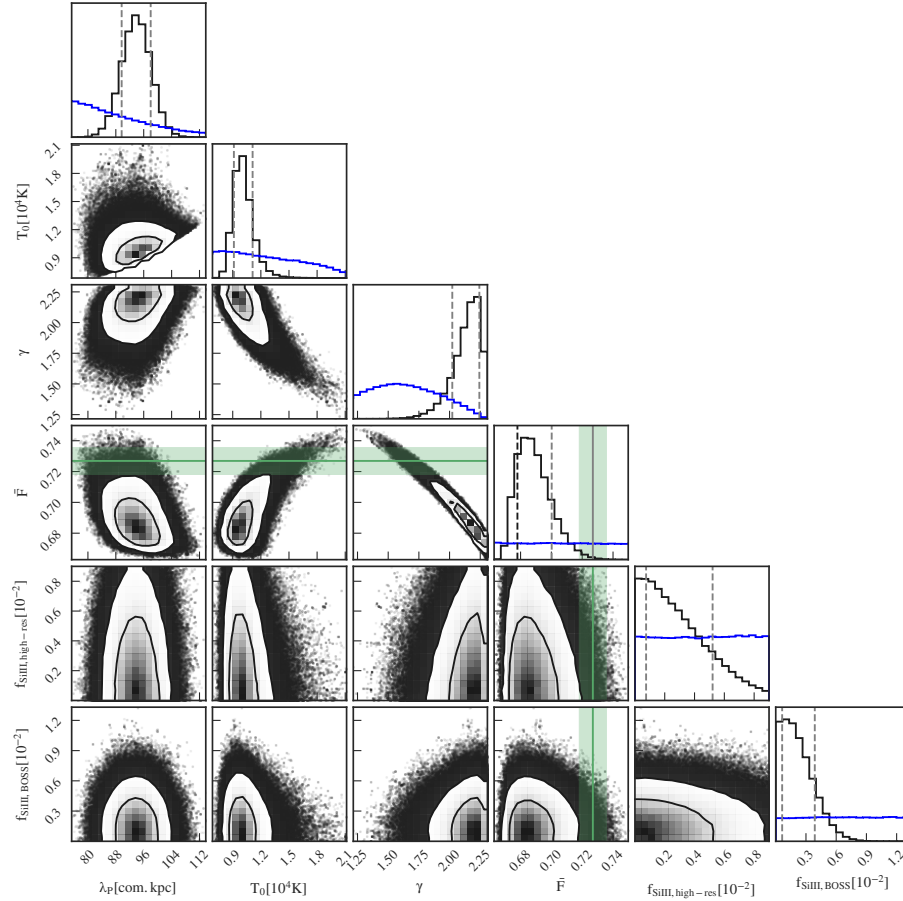


**Figure 4.6.:** Corner plot showing 1d- and 2d- marginalized posterior distributions for all fitting parameters at  $z = 2.8$  assuming a flat prior on  $\bar{F}$ . Blue curves in the 1d-histograms show 1d- marginalized distribution when ignoring the data and fitting the prior only (i.e. the result of the analysis performed for Figure 4.4). We can see that there are strong constraints on all parameters compared to the prior information. We also notice a strong correlation between permutations of  $\gamma$ ,  $T_0$  and  $\bar{F}$ . Note that the posterior in  $\bar{F}$  is significantly below the observed value of the Becker et al. (2013) mean flux measurement (shown as a green line with a band for the  $1-\sigma$ -region) which is, combined with the strong anticorrelation between  $\gamma$  and  $\bar{F}$  leading to higher values of  $\gamma$  than typically assumed.

#### 4. A New Measurement of IGM Thermal Evolution at $1.8 < z < 5.4$

we see is that there are strong degeneracies between some parameters, e.g. the diagonal contours between permutations of  $T_0$ ,  $\gamma$  and  $\bar{F}$ . Note that the strong correlation between  $T_0$  and  $\gamma$  is well understood and results from the IGM not probing the mean density, but instead mild overdensities at these redshifts (see e.g. Lidz et al., 2010; Becker et al., 2011). We also infer a low mean transmitted flux  $\bar{F} = 0.69 \pm 0.01$  compared to the Becker et al. (2013) measurement of  $\bar{F} = 0.727 \pm 0.009$  (green band). It is interesting to note that this low value however agrees well with the joint constraint on mean transmission evolution by Palanque-Delabrouille et al. (2015) obtained from the BOSS power spectrum yielding  $A = 0.0028 \pm 0.0002$ ,  $\eta = 3.67 \pm 0.02$  for  $\bar{F}(z) = \exp(-A(1+z)^\eta)$  resulting in  $\bar{F}(z = 2.8) \approx 0.687 \pm 0.020$ . Note that the dataset used in this analysis overlaps with the one we used here, but simulations and inference procedure are independent and our analysis has additional higher resolution data available. Independent of the BOSS data, we also obtain similarly low  $\bar{F}$  values when performing fits on the high-resolution data from chapter 3 alone.

Additionally, the posterior distribution for  $\gamma$  shows a clear preference for values  $\gamma \approx 2.1$ , far above the expected value of  $\sim 1.6$  for IGM gas in photoionization equilibrium long after reionization events (Hui, & Gnedin, 1997; McQuinn, & Upton Sanderbeck, 2016) Note again that there is a strong anti-correlation between  $\gamma$  and  $\bar{F}$ , so while our analysis prefers a high value of  $\gamma$  and a low value of  $\bar{F}$ , this is a movement along the degeneracy direction. We will further discuss this issue in § 4.4.2.

The redshift evolution of individual parameters, determined from the 1d marginalized posteriors, is illustrated in Figure 4.7. For  $3.0 \leq z \leq 3.4$  we also performed fits including the XQ-100 data, and fully marginalized over our lack of knowledge of the exact spectroscopic resolution (see discussion in § 4.3.4). As including this dataset did not significantly change our results, we decided to leave those points off the plot for clarity. Numerical values for the marginalized parameters are tabulated in Table 5 in the Appendix.

There are several noteworthy features in Figure 4.7. First, the disagreement that we saw at  $z = 2.8$  between our inferred value of  $\bar{F}$  and recent measurements is also present

#### 4.4. Thermal Evolution of the IGM

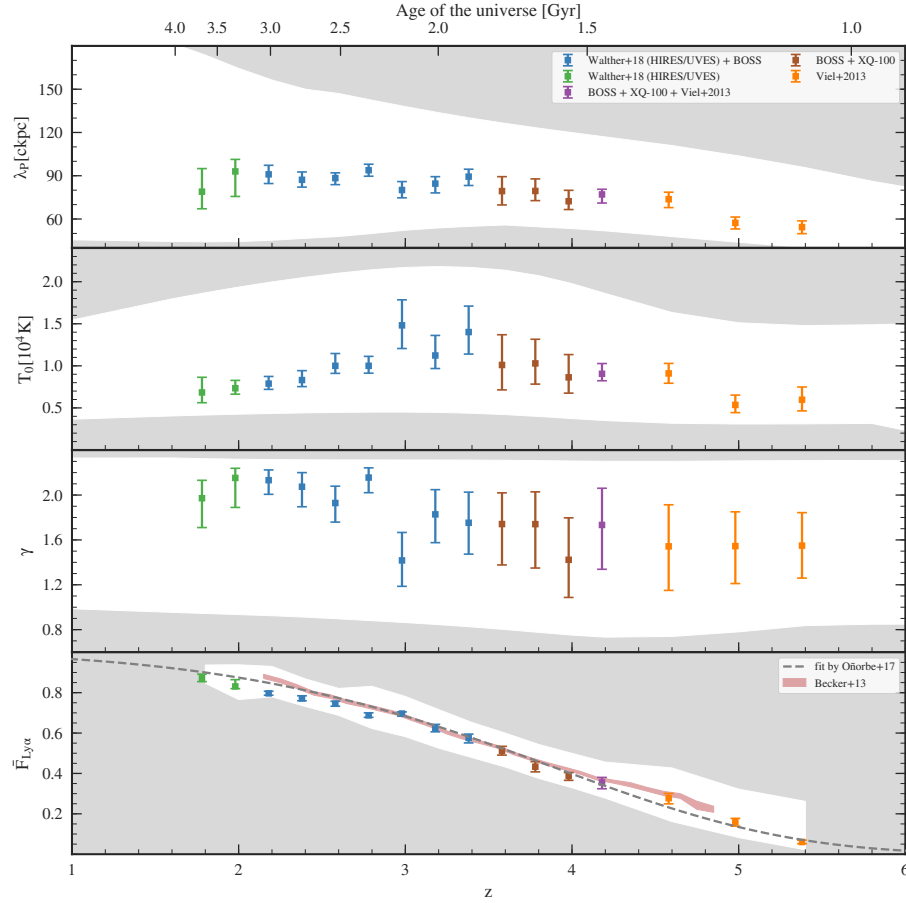


**Figure 4.7.:** Points with error bars show the median and the region between 16% and 84% quantiles of the 3 thermal parameters as well as the mean transmission of the IGM (marginalized over all model parameters of the fit) at different redshifts jointly using our fiducial dataset (squares) at each redshift. In the  $\bar{F}$  panel we also show the evolution obtained by Becker et al. (2013) (red band showing  $1\sigma$  uncertainties) based on relative changes in SDSS quasar transmissions as well as the Oñorbe et al. (2017b) (dashed line) fit to these data and further datasets. Note the large discrepancies between our measurements and those results when assuming an uninformative prior on the mean flux. The white range shows the space populated by our models, i.e. we cannot expect to measure values inside the gray shade using our current emulator.

#### 4. A New Measurement of IGM Thermal Evolution at $1.8 < z < 5.4$

at all other redshifts  $z < 3$  (green and blue datapoints compared to the pink shaded region in the lower panel). At the same time  $\gamma$  reaches very high values in the same redshift range. Also  $T_0$  drops strongly from  $z = 3.0$  to lower redshifts, but due to the degeneracies between  $T_0$ ,  $\gamma$ , and  $\bar{F}$  these measurements are all strongly correlated and this effect is therefore expected. Note that these trends – high  $\gamma$ , low  $\bar{F}$ , and low  $T_0$  – persists if we fit the high-resolution data alone, as the BOSS data alone do not individually constrain all of these parameters due to the lack of high- $k$  modes (resulting from limited spectral resolution).

Second, for  $z \geq 3$  we can see that  $\gamma$  shows little evolution and the mean transmitted flux  $\bar{F}$  is consistent with the Oñorbe et al. (2017b) fit to recent measurements. We can also see that  $T_0$  increases from  $\approx 5100$  K at  $z = 5.0$  to  $\approx 15\,000$  K at  $z = 3.4$ . This rise could be explained by the onset of He II reionization, which we discuss in more detail in § 4.4.5 where we compare our inferred parameter values to models of IGM thermal history that treat reionization heating.

In summary, we can see that the power spectrum analyzed here can in principle achieve high precision constraints on IGM thermal parameters and the mean transmission, but the high values of  $\gamma \approx 2$  inferred at  $z < 3$  and concomitant discrepancies between our inferred mean flux and the Becker et al. (2013) measurements might indicate systematics in our procedure. We consider this issue in detail in the next section.

#### 4.4.2. Analyzing the Discrepancies in $\gamma$ and $\bar{F}$

In the previous section we found low values of  $\bar{F}$  compared to Becker et al. (2013) and possibly unphysically high values of  $\gamma$ . While both parameters are degenerate and the degeneracy direction matches with our discrepancy this might point towards some problem within the analysis. To investigate this scenario we want to isolate the change in the power spectrum when moving along the degeneracy direction of our posterior distributions. Due to the dimensionality of the parameter space and correlations between different parameters this can't be achieved by simple cuts along a parameter direction.

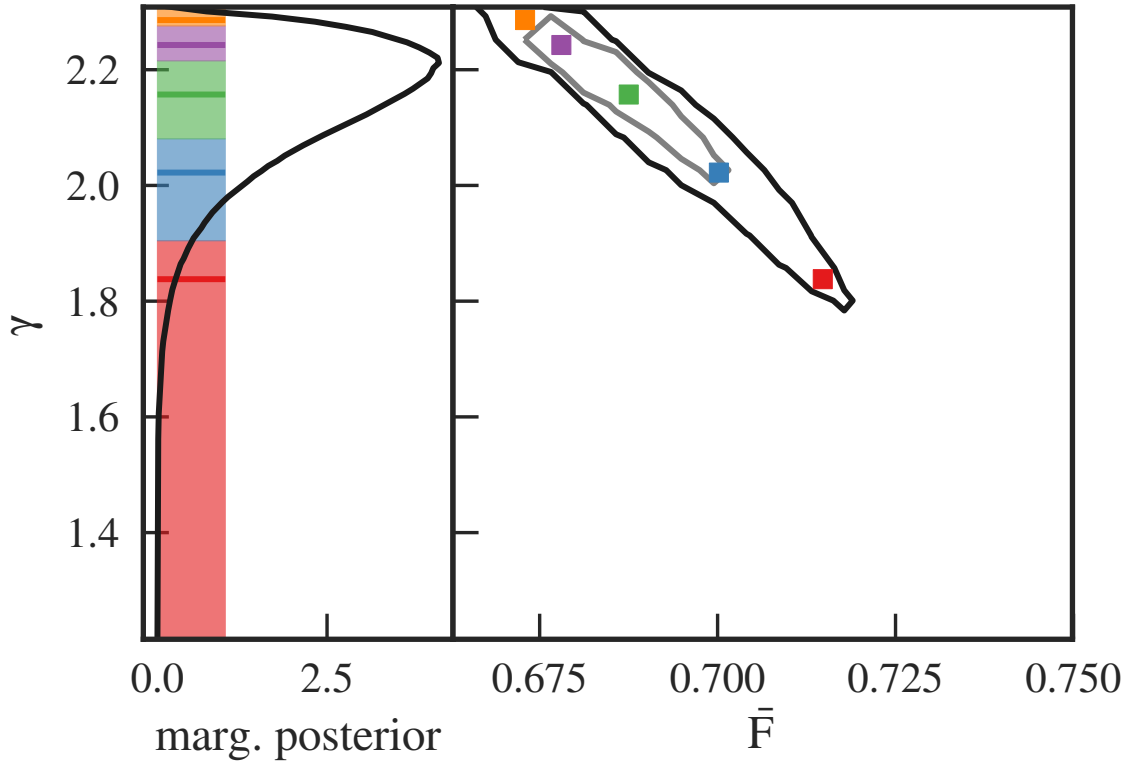


**Figure 4.8.:** Illustration for our approach in selecting models along the posterior distribution (see main text for details). Left: The marginalized posterior distribution of  $\gamma$  values from our chain with the bins which we used to select generate models at the 68% and 95% confidence intervals shown as bars. The median chain value in each bin is shown as a colored line. Right: 68% and 95% contours for  $\gamma$  vs.  $\bar{F}$  with the selected values of both parameters shown as squares.

Therefore we designed the following procedure to generate model curves tracking the degeneracy direction for different values of  $\gamma$  (also see the illustration in Figure 4.8):

- We take the posterior of our MCMC analysis (i.e. the Markov chain) and define bins such that the median of  $\gamma$  inside a bin is equal to a desired quantile of the marginalized  $\gamma$  distribution (which are chosen to be equivalent to  $\pm 1\sigma, \pm 2\sigma$ ).

These bins are shown as colored bars in the left panel of Figure 4.8.

- For  $\gamma$  values in our chain within a given bin, we then compute the median of all

#### 4. A New Measurement of IGM Thermal Evolution at $1.8 < z < 5.4$

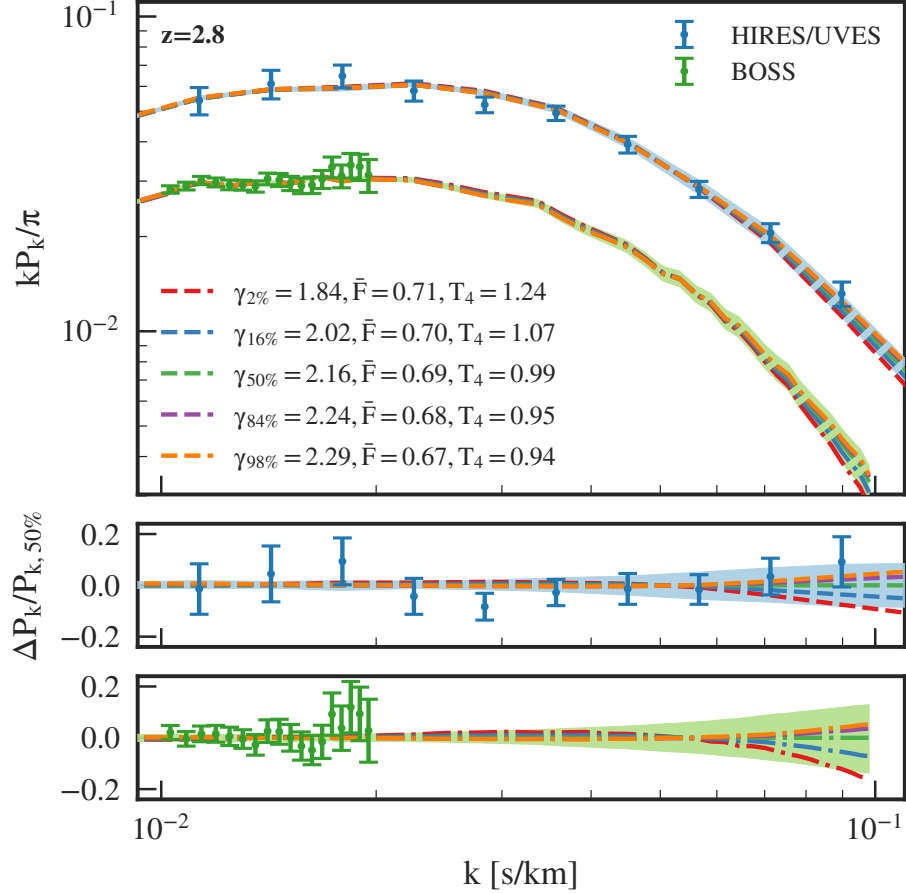


**Figure 4.9.:** Topmost panel: The power spectrum (not corrected for masking) at  $z = 2.8$  (other redshifts are shown in Figure 4.10, bands are showing regions in which 68% of models in the posterior fall) with curves showing models (drawn from the respective emulator) with different thermal parameters. Those are chosen such that the lines represent the 2.5%, 16%, 50%, 84% and 97.5% quantiles of the posterior distribution in  $\gamma$  while following degeneracies with the other parameters (see main text and Figure 4.8 for the details). Values of the most relevant parameters are printed inside the figure (with  $T_4 = T_0/10\,000$  K). Both datasets have been offset by a factor of two for clarity. Bottom panels: The fractional deviation between data in the topmost panel and the model at median  $\gamma$  (green curve) for each dataset.

#### 4.4. Thermal Evolution of the IGM

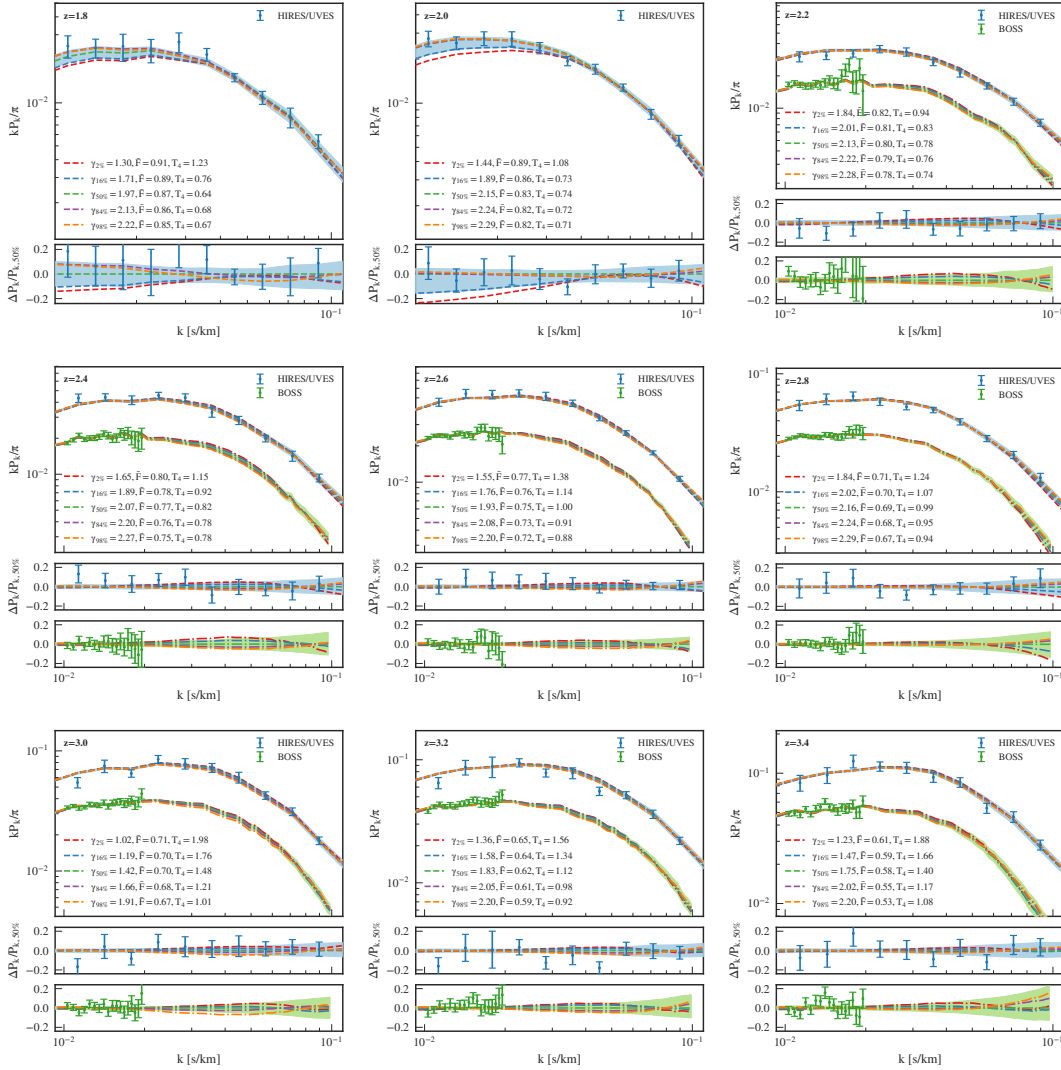


**Figure 4.10.:** Same as Figure 4.9, but also for all redshifts  $z \leq 3.4$ . We can see that while most redshift bins show the strongest scatter in the power at  $k \sim 0.06 \text{ s km}^{-1}$  when moving along the degeneracy direction. However, for  $z = 1.8, 2.0$  the behaviour seems to be significantly different most likely due to the lacking precision on small  $k$ .

#### 4. A New Measurement of IGM Thermal Evolution at $1.8 < z < 5.4$

other parameters. Because of the way we chose our  $\gamma$  bins, this yields the quantile of interest for  $\gamma$ , whereas the other parameters will track their corresponding degeneracy direction with respect to  $\gamma$ . This can be seen in the colored squares in the right panel of Figure 4.8.

- For the set of parameters at each of the quantiles (e.g. the 84% quantile in  $\gamma$  and the median in all other parameters for the corresponding bin) we can then generate a model using our Gaussian process emulator.

The result of this procedure is shown in Figure 4.9 for the power spectrum at redshift  $z = 2.8$  which is the highest redshift showing a high  $\gamma$  value. We compare models generated in this way to the measured power spectra shown as the blue and green points in the figure. Bands show the 68% confidence interval at each  $k$  for models generated using our emulator with random draws from the posterior distribution. Note that the forward model (due to both masking and forward modeling of noise and resolution) can generate slightly more converged model power spectra than the perfect model using the same parameters. The latter band is therefore actually a prediction for  $k \gtrsim 0.02 \text{ s km}^{-1}$  and its slightly larger extent is not surprising. Also note that due to the way we chose to produce curves with different thermal parameters and the dimensionality of the space the range spanned by the dashed curves is typically smaller than the colored bands. This is expected as the band shows the actual spread in the five/six (depending on the number of datasets used) dimensional parameter space whereas the lines are based on a quantile for one of the parameters and values at the center of the distribution close to that quantile for all others which will lead to a point inside the respective hypersurface, e.g. parameters of the purple/blue curve fall inside the five/six dimensional 68% surface, where the band corresponds to the actual surface).

We can see that all 5 models shown basically lead to the same power except for the highest  $k$ -values measured  $k \geq 0.07$  (smallest scales). At those scales a higher  $\gamma$  and lower  $\bar{F}$  indeed seems to provide a better fit to the data whereas at larger scales (smaller  $k$ ) the model does not seem to be strongly affected by the parameters when moving

along the degeneracy.

However, for other redshift bins (see Figure 4.10) the sensitivity of the power spectrum toward changes in  $\gamma$  for a region around the median value shifts to different scales. For example, at  $z \leq 2.0$  the most dominant effect seems to be on large scales, but note that we do not have the high precision BOSS measurement and that therefore both the range in allowed power spectra and the range of parameters in the  $2\sigma$  region of  $\gamma$  are larger. All other redshifts seem to suggest a highest sensitivity to  $\gamma$  at scales  $k \sim 0.05 \text{ s km}^{-1}$ , different from both the lowest redshifts and  $z = 2.8$ . While we note that differences between models of different  $\gamma$  along the degeneracy direction are typically small compared to our measurement errors for an individual  $k$ -bin, it is clear that the data of all bins combined has the precision to distinguish between these models, and that our inference is producing sensible fits. One might argue that the fact that the  $k$ -modes that are driving the fits to high  $\gamma$  and low  $\bar{F}$  change for different redshift bins is a source of concern, but we caution that the degeneracies in this multi-dimensional parameter space are complex and not always easy to visualize. We are confident that these results are not spurious, since this high  $\gamma$ , low  $\bar{F}$  combination persists consistently across all redshift bins with  $z \leq 2.8$ , and both measurements and our inference of different redshift bins are completely independent. We will return to this issue of discrepant  $\gamma$  and  $\bar{F}$  values in § 4.5 when we discuss possible systematic errors in our hydrodynamical simulations.

#### 4.4.3. Measuring Thermal Evolution in the IGM using a Gaussian Prior on the Mean Transmission

Given that independent precise constraints on the mean transmission exist we now consider the effect of applying a Gaussian prior on the mean transmission based on these measurements (see discussion in § 4.3.4 for details). Henceforth we will refer to these fits as the ‘strong prior’ results, and we will designate them as our fiducial measurements (as opposed to the joint fits for thermal parameters and  $\bar{F}$  described in previous sections). Note that most previous analyses of the IGM thermal properties have simply assumed

#### 4. A New Measurement of IGM Thermal Evolution at $1.8 < z < 5.4$

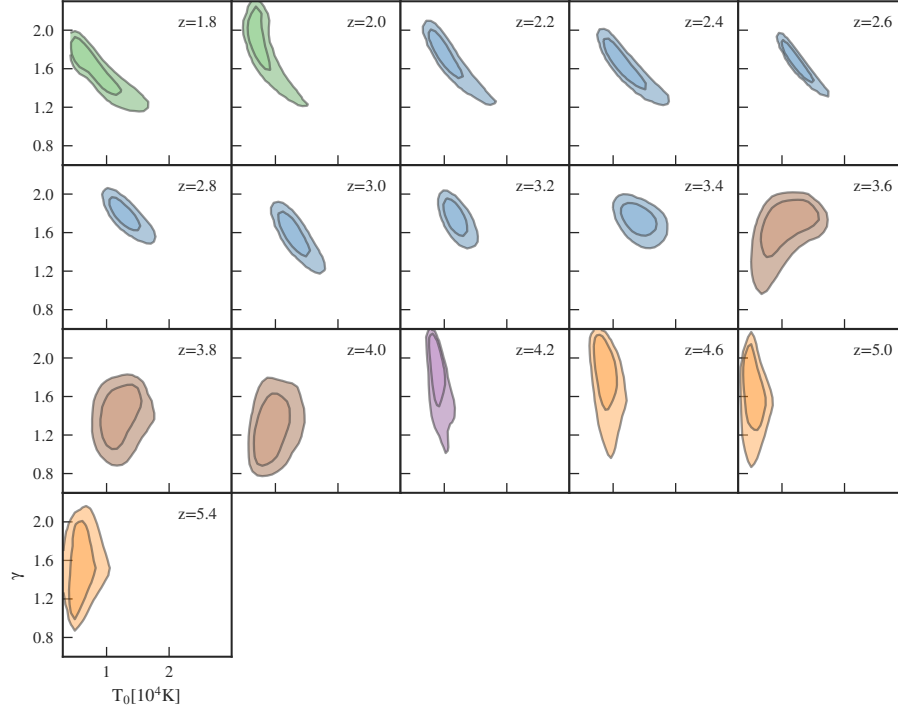


**Figure 4.11.:** Evolution of the  $T_0$  vs  $\gamma$  contours with redshift assuming the strong prior on  $\bar{F}$  for different combinations of datasets (different colors matched to Figure 4.7, filled contours showing our fiducial dataset while open contours show analyses ignoring the XQ-100 data as in the circles of Figure 4.7). When high resolution data is used we can see that strong constraints perpendicular to a degeneracy direction can be obtained. We can also see that this degeneracy direction rotates as the Ly $\alpha$  forest probes higher and higher densities.

perfect knowledge of the mean transmission (see Lidz et al., 2010; Iršič et al., 2017b, for exceptions), such that this ‘strong prior’ approach is more consistent with previous efforts.

We present the redshift evolution of posterior parameter degeneracies assuming the strong prior in Figure 4.11. Each panel in these figures shows the 2d marginalized 68% and 95% confidence regions of  $T_0$  vs.  $\gamma$ . While  $\gamma$  and  $T_0$  are strongly anticorrelated at low redshifts  $z \leq 3.4$ , i.e. the contours are close to diagonal, this correlation gets weaker at higher redshifts (especially at  $z \geq 4.2$ ), i.e. contours become aligned with the axes due

#### 4.4. Thermal Evolution of the IGM

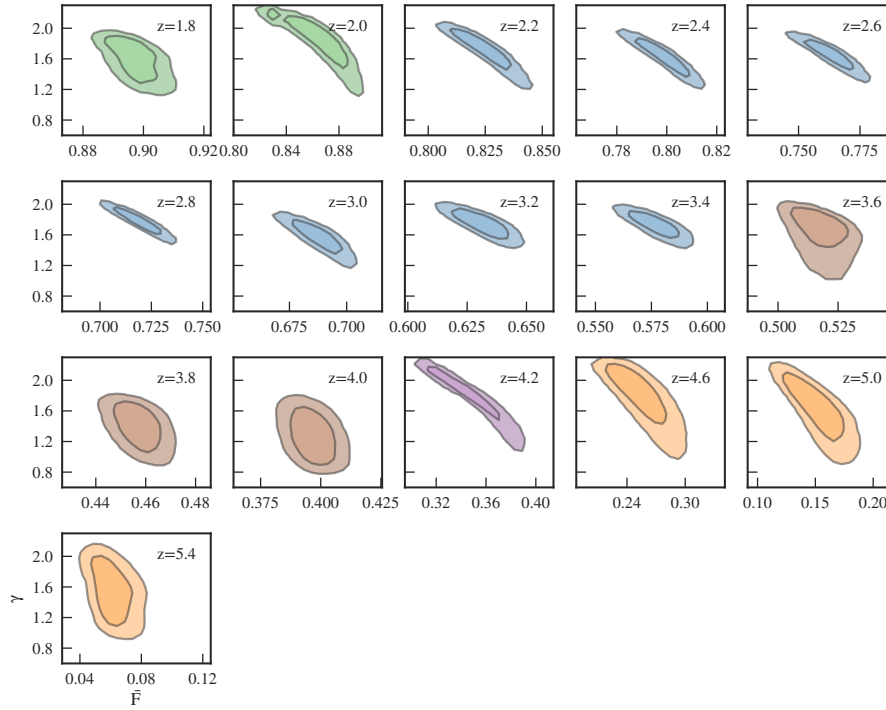


**Figure 4.12.:** The same as Figure 4.11 but with  $\bar{F}$  vs.  $\gamma$  contours. This shows that independent of redshift  $\gamma$  and  $\bar{F}$  are strongly anticorrelated.

to lower overdensities probed by the power spectrum. Likewise, the  $\gamma$  vs.  $\bar{F}$  confidence regions are shown in Figure 4.12. Note that these properties are correlated independent of redshift, in stark contrast to the thermal parameter degeneracy, while still changing shape and direction due to the different precision of the measurements. Therefore, a change of prior for the mean transmission measurements propagates into  $\gamma$  at high redshifts ( $z \geq 4.2$ ), but does not affect  $T_0$  significantly. At lower redshifts (especially for  $z \leq 3.4$ ), however,  $\gamma$  is strongly correlated with both  $T_0$  and  $\bar{F}$ , so a change in priors for any of the three quantities always affects the results on the other two quantities as well. Consequentially the change in our mean flux prior affects lower redshifts (especially  $z < 3$ ) more strongly than higher ones.

We show the fully marginalized posterior constraints on thermal parameters as a function of redshift in Figure 4.13. We can see that now the values of  $\gamma$  cover the

#### 4. A New Measurement of IGM Thermal Evolution at $1.8 < z < 5.4$

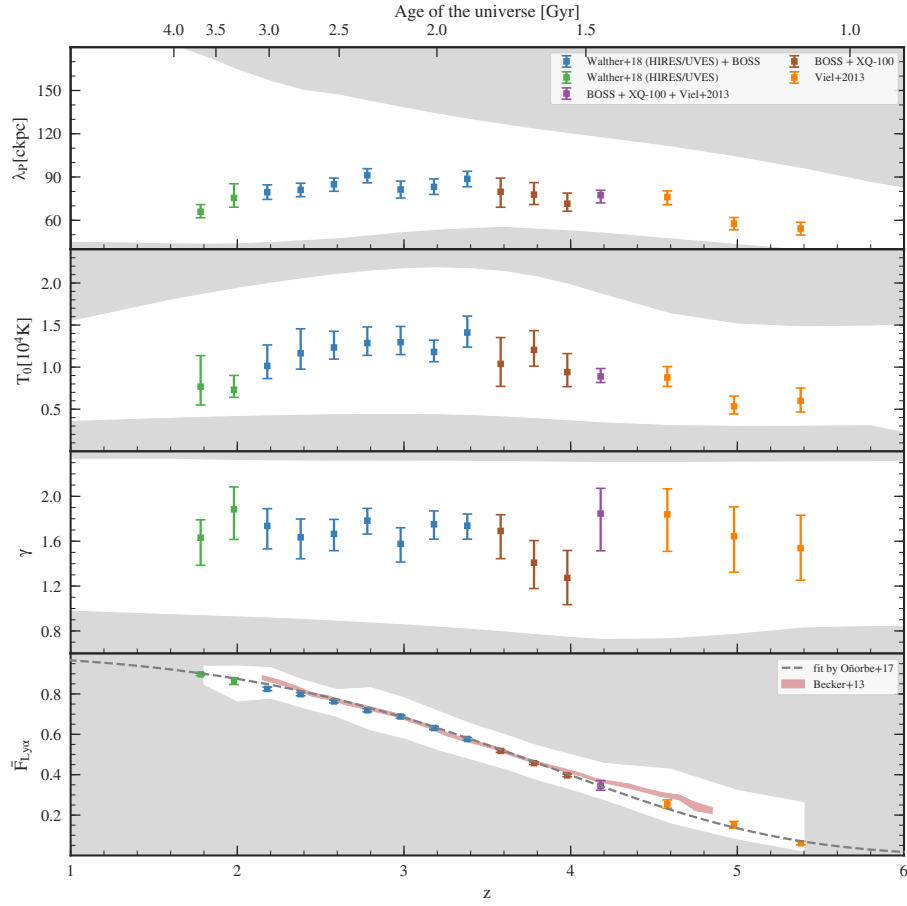


**Figure 4.13.:** The fiducial measurements from Figure 4.7, but assuming a Gaussian prior on the mean transmission complying with the fit of (Oñorbe et al., 2017a) measurement within errorbars given by observations (Becker et al., 2013; Faucher-Giguère et al., 2008a; Kirkman et al., 2005). We can see that now the obtained  $\gamma$  values at low redshifts are far lower (and compatible with the expected value of 1.6 long after reionization) due to the additional mean transmission constraint. The high values of  $\gamma$  at high redshifts obtained here, are likely due to the discrepancy of the mean of our chosen prior (dashed curve) with the Becker et al. (2013) (red band) analysis for the mean transmission. Due to the far lower overdensities probed at high-redshifts compared to low redshifts these high values of  $\gamma$  do not change results on  $T_0$  strongly as degeneracies are largely broken (see also the evolution of the  $T_0$ - $\gamma$  and  $\gamma$ - $\bar{F}$  contours which can be found in Figure 4.11 and Figure 4.12 ).

#### 4.4. Thermal Evolution of the IGM

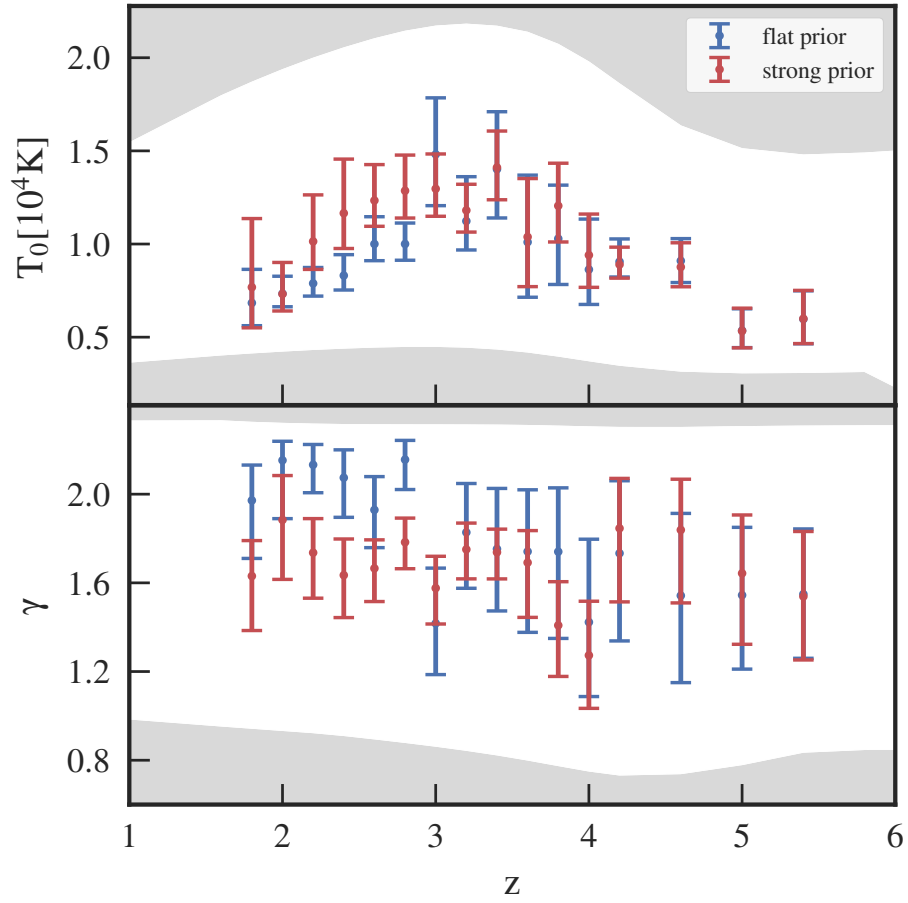


**Figure 4.14.:** Comparison of our results on the thermal state dependent on redshift between both priors (different colors). We can see that the flat prior leads to far higher values of  $\gamma$  that due to correlations between parameters lead to lower values of  $T_0$  (.)

#### 4. A New Measurement of IGM Thermal Evolution at $1.8 < z < 5.4$

theoretically expected value of  $\gamma \approx 1.6$  at low redshifts  $z < 3$ , while the values of  $T_0$  obtained are higher than in the fit using a flat prior on mean transmission because of the degeneracies between  $T_0$  and  $\gamma$ . This is more clearly illustrated in Figure 4.14 where we compare  $T_0$  and  $\gamma$  evolution for the different prior assumptions. We can see that indeed the changes between both the two fits are strongly anticorrelated between  $T_0$  and  $\gamma$  and that the change in marginalized parameters between the two cases can be large, particularly for  $\gamma$  where the differences at  $2.2 \leq z \leq 2.6$  are  $\gtrsim 2\sigma$  and as high as  $3\sigma$  at  $z = 2.8$ .

However, this is the first thermal evolution measurement performed over the whole epoch of He II reionization and beyond based on the power spectrum. Using the strong mean flux prior we also obtained reasonable results including physically possible measurements of  $\gamma$ , a rise in temperature for  $z \gtrsim 3$  and the first measurement of the IGM cooling down thereafter. In the next sections we compare our strong prior results to recent thermal parameter measurements from different methods as well as models of IGM thermal evolution.

#### 4.4.4. Comparison to Previous Measurements

A comparison of our results to recent measurements of thermal parameters is shown in Figure 4.15. We discuss the various datasets involved and elaborate on the comparison to our new measurement below.

The phase angle PDF of quasar pairs (Rorai et al., 2013) measures the smoothness of the 3d distribution of IGM gas and therefore directly constrains the pressure smoothing scale  $\lambda_p$  independent of the instantaneous thermal state of the IGM (i.e.  $T_0$  and  $\gamma$ ). Rorai et al. (2017b) measured  $\lambda_p$  from a sample of quasar pairs in 4 redshift bins between  $2.0 \leq z \leq 3.6$ . Figure 4.15 shows that our inferred values of  $\lambda_p$  are fully consistent with the Rorai et al. (2017b) measurement. We also see a smaller uncertainty in our power spectrum based measurement. Part of the explanation for these small error bars lies in how our model grid, and therefore our prior probability, is set up. As discussed

#### 4.4. Thermal Evolution of the IGM

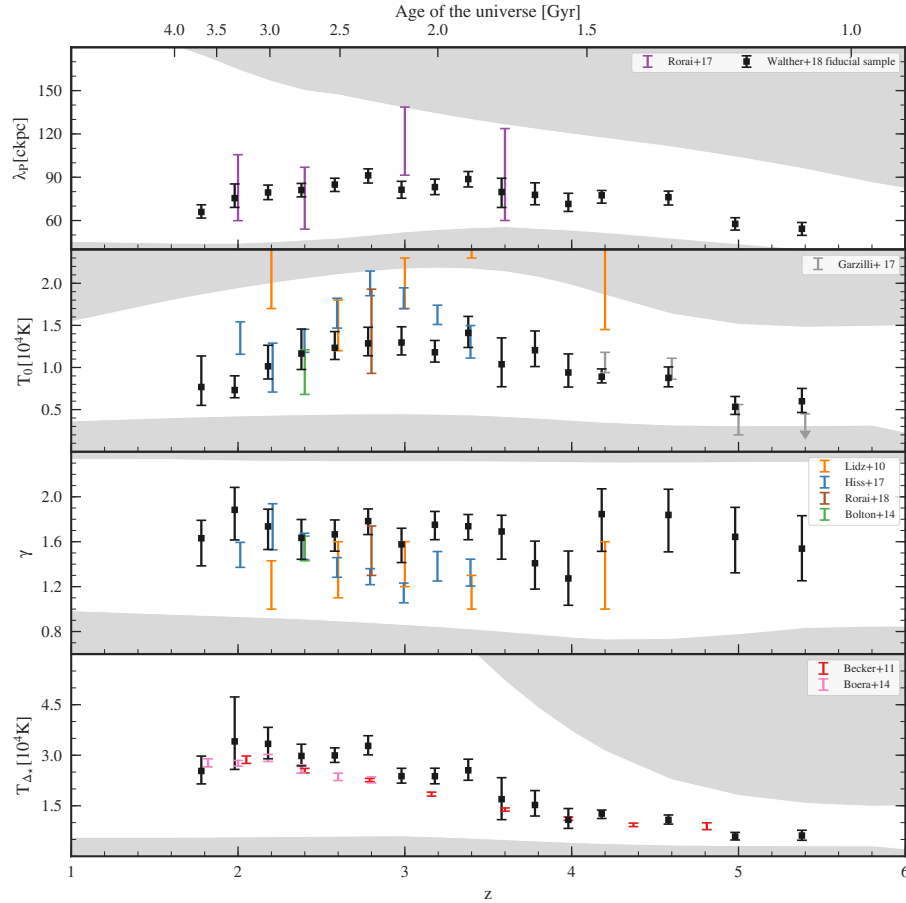


**Figure 4.15.:** The fiducial data from Figure 4.13 (black points) assuming the strong Gaussian prior on  $\bar{F}$ . In addition to the previous plots we show the thermal parameters as well as  $T(\Delta_\star)$  at the optimal overdensities  $\Delta_\star$  for curvature measurements as given by Becker et al. (2011). We compare to measurements of thermal evolution in the IGM based on different statistics: curvature (red, pink), line fitting (green, blue, brown), wavelets (orange), phase angles (purple) and power spectrum (gray). We can see overall good agreement with previous datasets (except for wavelets) albeit significantly higher  $T(\Delta_\star)$  than in the curvature measurements is obtained at some redshifts. All measurement errors shown are  $1\sigma$  or 68% intervals, for measurements that only quote  $2\sigma$  errorbars we divided those by a factor of two.

#### 4. A New Measurement of IGM Thermal Evolution at $1.8 < z < 5.4$

in § 4.3.4, the degeneracy between  $T_0$  and  $\lambda_P$  within our simulated models combined with our approach of not extrapolating to regions outside our model grid result in a positive correlation in the prior probability between these parameters. However, the power spectrum cutoff, is sensitive to a degenerate combination of both  $\lambda_P$  and thermal broadening (Peebles et al., 2010b; Rorai et al., 2013) leading to an anti-correlation in the likelihood. So the correlations inside our prior (Figure 4.4) and the degeneracy direction of the likelihood due to the aforementioned effect are nearly perpendicular and as the posterior distribution is the product of these two, resulting constraints appear very tight. However, we argue that it is hard to generate physical models without imprinting the correlation between thermal state and  $\lambda_P$  that depends on the integrated thermal history of the IGM. While the uncertainties in  $\lambda_P$  might still be somewhat underestimated, we note that our prior grid degeneracy has a strong physical motivation (see also § 4.3.4).

The orange points in Figure 4.15 show the  $T_0$  and  $\gamma$  measurements from Lidz et al. (2010), who decomposed the Ly $\alpha$  forest of the Dall’Aglia et al. (2008) dataset into wavelets and analyze the PDF of their squared amplitudes to derive constraints on the thermal state of the IGM. We note that this data is a subset of that used to compute the power spectrum in chapter 3 and analyzed here. Note that their  $\gamma$  constraint is often limited to the boundaries of their fits<sup>4.11</sup>. While the wavelet analysis results at  $z = 2.6$  are consistent with our measurement we disfavor the  $z = 2.2$ ,  $z = 3.0$ ,  $z = 4$  and especially  $z = 3.4$  wavelet results which seem to indicate a far hotter IGM than our measurement. The origin of this discrepancy is unclear, but it was also noted before by Becker et al. (2011).

Another method for obtaining constraints on the thermal state of the IGM is by decomposing the Ly $\alpha$  forest into individual absorption lines, assuming that a cutoff in the distribution of column densities  $N_{\text{HI}}$  vs. Doppler parameter  $b$  exists and can be attributed to lines that are only thermally broadened (see e.g. Schaye et al., 2000; Rudie et al., 2012; Bolton et al., 2014; Hiss et al., 2018; Rorai et al., 2018). Especially the new Hiss et al. (2018) (which is based on the same dataset as chapter 3 and is using a subset of the same

---

<sup>4.11</sup>We therefore show the extent of their  $1\sigma$  contours (as a by-eye marginalization) for  $\gamma$  in the Figure.

#### 4.4. Thermal Evolution of the IGM

simulation grid) thermal evolution result seems to hint toward a period of heating until  $z \sim 2.8$  that could be attributed to He II reionization.

For both  $T_0$  and  $\gamma$  we see broad agreement between our measurements and the line-fitting results at most redshifts. Of particular interest are  $z = 2.4$  and  $z = 2.8$  where several line fitting measurements exist. At  $z = 2.4$  we do reproduce the result from Hiss et al. (2018) (blue points) as well as Bolton et al. (2014) (green) in both  $T_0$  and  $\gamma$ . At  $z = 2.8$  we agree with the Rorai et al. (2018) (brown point), but obtain higher precision. However, agreement with Hiss et al. (2018) at this redshift seems to be poor as they measure both higher  $T_0$  and lower  $\gamma$  (which is along the degeneracy direction for line fitting analyses as well as the power spectrum). Part of this discrepancy might come from systematics in the Voigt profile analysis depending on the cutoff fitting algorithm chosen, as Hiss et al. (2018, see Appendix B) find either a multimodal posterior probability distribution for  $T_0, \gamma$  with a similar 68% confidence interval as the Rorai et al. (2018) or a unimodal distribution with the values shown here depending on the cutoff fitting algorithm used. Whether this multimodal behavior results from systematics in the measurement procedure or is a real physical effect from e.g. a real multimodal IGM temperature density relation is not yet clear, but we do not see such behavior in our power spectrum analysis. For the other overlapping redshifts (except  $z = 2.2$  and  $z = 2.4$  which match very well) we generally measure a lower  $T_0$  and higher  $\gamma$  compared to Hiss et al. (2018).

The most precise measurements of temperature in the IGM so far are based on the mean curvature in the Ly $\alpha$  forest  $\langle \kappa \rangle$  (Becker et al., 2011; Boera et al., 2014). These measurements constrain  $T(\Delta_\star)$  at an optimal overdensity  $\Delta_\star$  at which a one-to-one relation between the mean curvature  $\langle \kappa \rangle$  of the Ly $\alpha$  forest and  $T(\Delta_\star)$  exists independent of the slope  $\gamma$  of the TDR (note again Figure 4.11 which shows the corresponding degeneracy for the power spectrum). However this method is not able to measure  $\gamma$  or  $T_0$  independently. To compare to curvature based measurements, we compute  $T_{\Delta_\star} = T_0 \Delta_\star^{\gamma-1}$  (using the values for  $\Delta_\star$  given by Becker et al. 2011) for each sample in our MCMC chain and evaluate the 68% confidence interval. This approach allows us to directly compare to what the curvature results measure.

#### 4. A New Measurement of IGM Thermal Evolution at $1.8 < z < 5.4$

The agreement with the curvature analysis seems to be generally good for the largest part of the overlapping redshift range, but we seem to measure overall slightly higher temperatures. There are some redshifts  $z = 2.6, 2.8, 3.2, 3.4$  where our analysis gives significantly higher temperatures than implied by the curvature measurements. Note in particular that at  $z = 2.8$  where we see the strongest discrepancy between our results and the curvature measurements, multiple measurements of the thermal state have been performed via several different methods and these results do not fully agree with each other. We argue, that the overall agreement is still good given the significantly different datasets, statistical approaches and models used for both types of analysis. E.g., the difference in measured thermal state might potentially arise due to the different sensitivity of both statistics to metal contamination. While the power spectrum is only weakly affected by residual metal lines on the very smallest scales we cover here (see the comparison in Figure 3.7), the averaged squared curvature is basically measuring  $\int_{k_{\min}}^{\infty} k^5 P(k) d \ln k$  (see Appendix D in Puchwein et al., 2015) and thus enhances the weight of residual small scale contamination in the Ly $\alpha$  forest. At the same time small scale contaminants, like e.g. leftover metal lines, would decrease the obtained IGM temperatures as there is now too much small-scale power, thus leading to a colder IGM in curvature than in power spectrum analyses. Additionally, these measurements did not marginalize over the mean flux in the simulations, thereby e.g. potentially underestimate their errors.

Finally, we also show the Garzilli et al. (2017) measurement of  $T_0$  at  $4.2 \leq z \leq 5.4$  based on the same Viel et al. (2013b) dataset we use here (gray points, the limit is at the  $1\sigma$  level), but using a different analysis pipeline and including a warm dark matter (WDM) particle mass as an additional free parameter. We can see that for  $z \leq 5$  the agreement is good, but for  $z = 5.4$  we seem to get slightly higher values of  $T_0$  than their  $1\sigma$  upper limit. Part of that difference can be attributed to the additional freedom in their model.

Overall we conclude, that the agreement between our data and previous results is reasonably good. Our measurement comprises a strong advancement with regard to previous analyses especially due to the large range of uniformly covered redshifts and

**Table 4.2:** Thermal evolution models used in comparisons to existing measurements, parameters are the reionization redshifts and the total heat input during reionization for HI and He II, see Oñorbe et al. (2017b) for details

model name	$z_{\text{reion,HI}}$	$z_{\text{reion,He II}}$	$\Delta T_{\text{HI}}[\text{K}]$	$\Delta T_{\text{He II}}[\text{K}]$
no He II	7.3	–	20000	–
cold He II	6.55	3.0	20000	10000
standard He II	6.55	3.0	20000	15000
warm He II	6.55	3.0	20000	20000
hot He II	6.55	3.0	20000	30000
late He II	6.55	2.8	20000	15000

due to jointly constraining  $T_0$  and  $\gamma$  over this full range.

#### 4.4.5. Comparing to Thermal Evolution Models for Different He II Reionization Scenarios

In the previous sections we performed a self-consistent measurement of thermal evolution in the IGM from  $z = 5.4$  to  $z = 1.8$  corresponding to 3 Gyr of cosmic history. In this section we compare to simulations to thermal evolution due to He II reionization as this is expected to be the dominant process setting the thermal state of the IGM at this epoch.

In Figure 4.16 we show comparisons between our thermal evolution measurement and models based on different approaches. The solid curves show the "explicit reionization" simulations from our model grid for which hydrogen reionizes (to a level  $x_{\text{H II}} = 99.9\%$ ) at  $z_{\text{reion,HI}} = 6.5$  in agreement with the Planck Collaboration et al. (2016a) (and also Planck Collaboration et al. 2018) constraints, but for which the parameters governing He II reionization are varied (see Table 4.2). The red dash-dotted curve is showing an extreme version of these models for which He II was never reionized<sup>4.12</sup>. The measured

<sup>4.12</sup>We note that this reionizes HI slightly earlier  $z = 7.3$  which is still in good agreement with both Planck

#### 4. A New Measurement of IGM Thermal Evolution at $1.8 < z < 5.4$

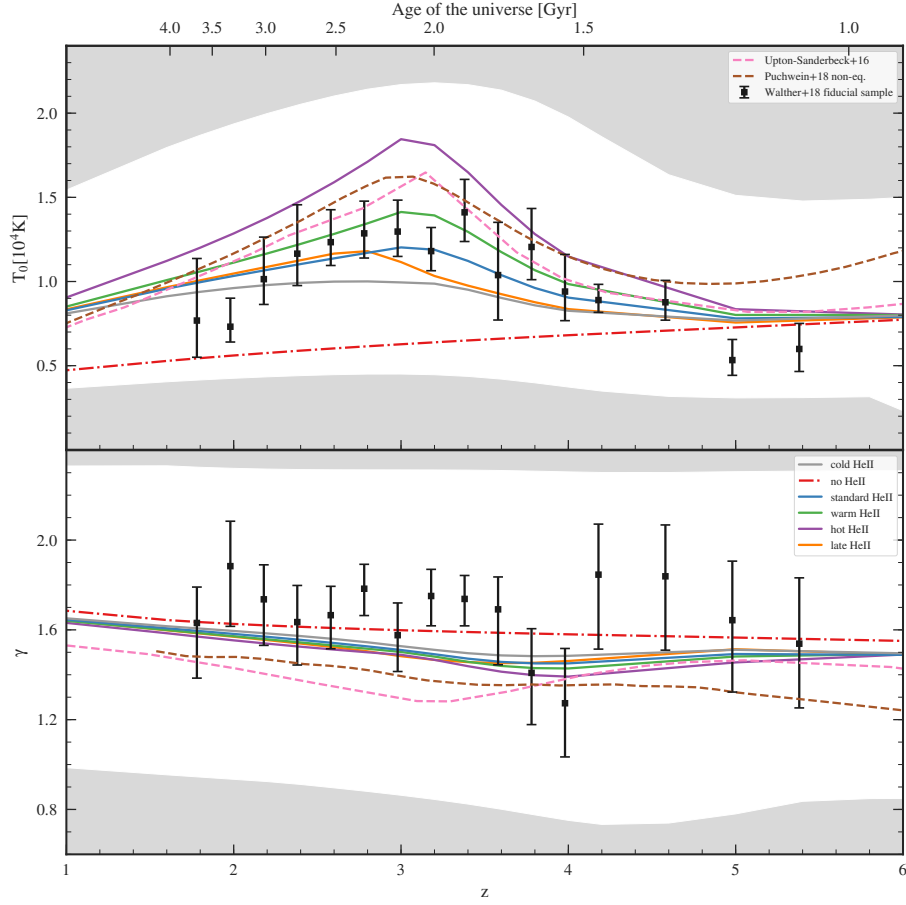


**Figure 4.16.:** The fiducial data assuming the strong Gaussian prior from Figure 4.13 (black points) compared to thermal evolution models assuming different redshifts of He II reionization and heat inputs during this process (solid curves) and without any He II reionization (dot-dashed red curve). The model parameters are given in Table 4.2. We also show comparisons to the Upton Sanderbeck et al. (2016) (dashed pink) thermal evolution model and a run using the Puchwein et al. (2018) non-eq. heating rates in a Nyx simulation (dashed brown). We can clearly see that the data shows a hotter IGM than created in the model without He II reionization. Instead, the overall evolution of thermal parameters seems to agree well with the standard to warm He II reionization scenarios in both  $T_0$  and  $\gamma$ . Finally, the temperatures found at the 2 highest redshift bins are colder than any model.

#### 4.4. Thermal Evolution of the IGM

temperature at mean density is significantly higher (by  $\gtrsim 3\sigma$  for each of the 7 individual redshift bins with  $2.2 \leq z \leq 3.4$ ) than this "no He II" scenario for  $z \leq 4.6$  suggestive of a period of He II reionization taking place.

To allow a comparison between different He II reionization scenarios, the gray, blue, green, and purple curves show models with  $z_{\text{reion,He II}} = 3.0$  assuming different amounts of heat being injected  $\Delta T_{\text{He II}}$  into the IGM varying from 10 000 K (cold) to 30 000 K (hot); whereas the orange curve shows a model with  $\Delta T_{\text{He II}} = 15\,000$  K but  $z_{\text{reion,He II}} = 2.8$  (late). We can see that the models predict an extended period of heating (i.e. increasing  $T_0$ ) until  $z_{\text{reion,He II}}$  followed by the IGM cooling down due to the expansion of the universe whose effects on the thermal state cannot be fully counteracted by ionizations anymore. Overall, for our measurement this rise and fall in  $T_0$  lies between the standard and warm He II evolution models for  $2.2 \leq z \leq 4.6$  disfavoring particularly hot or late phases of He II reionization.

We also compare to the analytical thermal evolution model by Upton Sanderbeck et al. (2016) and the fiducial non-equilibrium reionization model by Puchwein et al. (2018, see their Figure 6). We note that while the general shape of thermal evolution looks similar to both models for  $z \leq 4.6$  we seem to obtain a slightly less pronounced peak in  $T_0$ . Overall, the temperature evolution we see in this redshift range is indeed well modeled by an He II reionization event followed by photoionization equilibrium in an adiabatically expanding IGM. While it has been argued that this effect has been seen before (Becker et al., 2011), previous work did not break the degeneracy between  $\gamma$  and  $T_0$ . Note that also the cooldown of the IGM after reionization has never been conclusively observed due to this degeneracy.

Models of He II reionization typically also show a dip in  $\gamma$  resulting from the IGM to be more isothermal during reionization events (see e.g. also McQuinn et al., 2009). We can also see this effect by comparing  $\gamma$  for our He II models with the no-He II model. Note that while the Upton Sanderbeck et al. (2016) model also shows a dip (albeit at later times and with a more strongly isothermal  $\gamma$ ), the fully non-equilibrium simulation by

---

results.

#### 4. A New Measurement of IGM Thermal Evolution at $1.8 < z < 5.4$

Puchwein et al. (2018) does show an intrinsically smaller  $\gamma$  and no strong dip. The reason for this is that the non-equilibrium model reached  $\gamma = 1$  at  $z = 7$  due to HI reionization and is still recovering from this feature, i.e. it did not yet forget about the timing of HI reionization. The "dip" for this model therefore manifests in the near constant evolution from  $z \sim 5$  to  $z \sim 3$  compared to an otherwise expected rise in  $\gamma$ .

We can see this dip in  $\gamma$  for the measurement at  $z \sim 3.9$  aligned in redshift with the expected decrease due to He II reionization in our explicit He II reionization models. Note that the dip is only  $\sim 2\sigma$  significant compared to the no-He II reion model, but overall a slightly higher value for  $\gamma$  than this model is preferred. Also note that on the data side this feature is currently dominated by XQ-100 data (which is the highest resolution data available at  $3.6 \leq z \leq 4.0$ ) which we strongly degraded by marginalizing over resolution. Additional high resolution data or an accurate determination of the XQ-100 dataset resolution at these redshifts and adopting a prior based on those results could therefore lead to additional constraints on He II reionization due to its signature in the slope of the TDR.

Note that this feature also strongly relies on precise knowledge of  $\bar{F}$  as the expected decrease is very shallow. Additionally,  $\gamma$  values for  $z > 4.2$  might have a significant uncertainty as measurements of the mean transmission get less accurate for this range due to the smaller amounts of data available and stronger fluctuations in the ionization state of the IGM. Thus, there are currently several discrepant measurements of  $\bar{F}$  (as discussed in § 4.3.4) which consequently lead to a high uncertainty in  $\gamma$ .

At early times ( $z \geq 5$ , we call those points the highest redshift measurements) we can see that the measured  $T_0$  is lower than in any of the models. Note again that similarly low temperatures were also obtained by Garzilli et al. 2017 based on the same dataset in a fully independent analysis. While one could in principle think that an earlier redshift of HI reionization gives the IGM more time to cool thereafter leading to lower temperatures at these times, models suggest that is not the case and  $T_0$  has essentially forgotten about the timing of reionization by  $z = 5.4$  (see e.g. Oñorbe et al. 2017a who present models for a range of different  $6.0 < z_{\text{reion,HI}} < 9.7$ ). Instead the post-reionization thermal state

#### 4.5. Systematic Effects on the Measured Thermal Evolution

mostly depends on the spectral shape of the UVB (McQuinn, & Upton Sanderbeck, 2016) and a low temperature at  $z \sim 5.4$  requires lower photoheating rates, i.e. a particularly soft SED for ionizing sources is needed which is not favored by current models of the UVB (Faucher-Giguère et al., 2009; Haardt, & Madau, 2012; Stanway et al., 2016; D’Aloisio et al., 2018b; Puchwein et al., 2018).

While it may be that the thermal state at  $z \simeq 5.4$  would still be sensitive to the reionization redshift for particularly late  $z \lesssim 6$  reionization scenario (which now seems to be allowed regarding the newest CMB results from Planck Collaboration et al., 2018), this would nevertheless need to be in conjunction with very low reionization heat injection. The recent results by D’Aloisio et al. (2018b) who use radiative transfer to simulate photoheating by ionization fronts during H I reionization suggest that such low levels of IGM heating are unlikely. Finally, note that the onset of He II reionization can only increase model temperatures and therefore worsen the disagreement as none of the models shown exhibits any He II reionization before  $z = 4.8$ .

Therefore, the small temperatures we (and also other groups using the same dataset) obtain at  $z \geq 5$  are challenging to fit with current models of reionization. Consequently, models fitting the low-T measurements would also lead to a colder IGM at later times without additionally increasing heating due to e.g. He II reionization. However, as current constraints at the highest redshifts rest upon the single dataset by Viel et al. (2013b) based on a handful of objects, future measurements based on larger samples of quasar spectra obtained might change those low- $T_0$  results.

## 4.5. Systematic Effects on the Measured Thermal Evolution

In § 4.4.1 we attempted to jointly fit the mean flux and thermal parameters and arrived at puzzling results for  $\gamma$ . This, combined with the fact that independent high-precision measurements of the mean flux are available and that the most precise former analyses

#### 4. A New Measurement of IGM Thermal Evolution at $1.8 < z < 5.4$

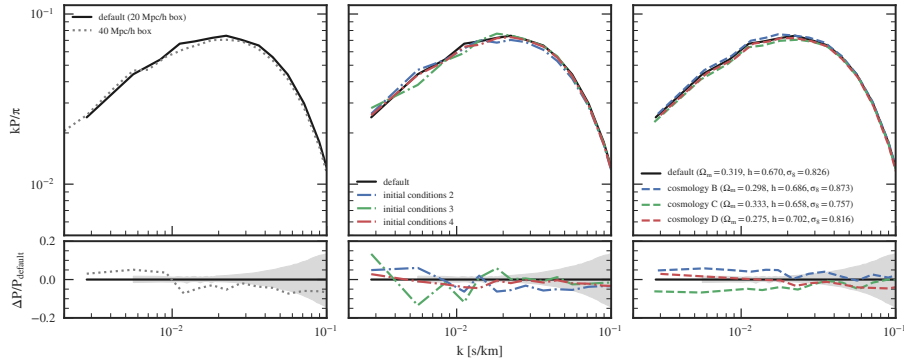


**Figure 4.17.:** Left: One model from our thermal grid at  $z = 2.8$  (solid black, the redshift is taken as an example, other redshifts are similar) compared to the same model run with a two times larger box and the same spatial resolution (dotted gray). The bottom panel shows relative differences and the size of the 68% confidence region of jointly fitting BOSS + high-resolution data as a grey band. Center: A comparison between different initial conditions (dot-dashed) that were otherwise run with the same setup. Right: A comparison of models based on other cosmologies (B,C are compatible with the Planck Collaboration et al. 2016b parameters and chosen to maximally change the matter power spectrum w.r.t. the default model, see Oñorbe et al. 2017b for details; D is the cosmology from Lukić et al. 2015). We can see that all three effects change the power on the 5% level.

of thermal evolution fixed the mean flux, led us to adopt the strong prior which led to sensible results on thermal evolution of the IGM that are in broad agreement with previous measurements as well as simulation predictions. In this section we investigate possible systematics in our modeling procedure which could be responsible for the high  $\gamma$ - low  $\bar{F}$  we observe with the flat prior on  $\bar{F}$  in § 4.4.

We think that the biggest issue is our modeling and there are several possible sources of bias for our measurement: the small boxes used and the cosmic variance, not simultaneously exploring cosmological parameters, and spatial resolution of the simulation. We attempt to quantify the significance of all these issues below. While ideally a large set of simulations would be used to do a detailed study of each issue, due to computational cost we are limited to a handful of simulations per problem.

To explore box size we compare one model from our grid to a simulation with exactly

#### 4.5. Systematic Effects on the Measured Thermal Evolution

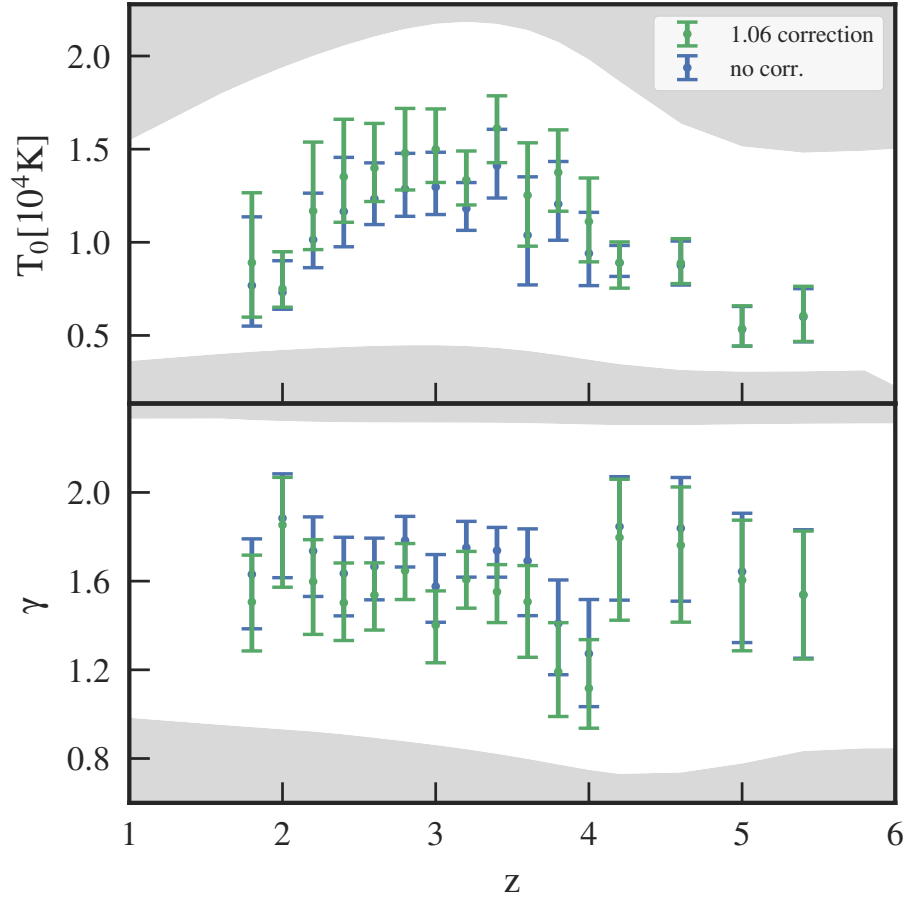


**Figure 4.18.:** Comparison of our results on the thermal state with fits obtained if we apply a flat "correction factor" of 0.94 (mimicking the joint effect of box size and cosmic variance seen in Figure 4.17) to the model power (different colors). We can see that without the "correction" higher values of  $\gamma$  as well as lower values of  $T_0$  (due to correlations between parameters) are obtained.

#### 4. A New Measurement of IGM Thermal Evolution at $1.8 < z < 5.4$

the same thermal model and cosmology performed with the same resolution, but with twice the box size, i.e.  $L_{\text{box}} = 40 h^{-1} \text{ Mpc}$ ,  $N_{\text{cell}} = 2048^3$ <sup>4.13</sup> In the left panel of Figure 4.17 we show this comparison. Similar to the results of Lukić et al. (2015), one clearly sees that for the range of power spectrum modes that we fit a  $\sim 6\%$  bias in the power might be expected due to box size effects. The gray curve shows the posterior 68% model interval from Figure 4.5 as a measure of the joint precision of all datasets used in the fit. So especially for scales  $k \lesssim 0.03 \text{ s km}^{-1}$  box size effects are larger than this precision and could thus strongly affect the results. Whether the overall 6% at  $k \gtrsim 0.01 \text{ s km}^{-1}$  results from box size effects or cosmic variance (see below) is unclear, but assuming the former, we perform an estimate of how much a flat bias affects our thermal evolution constraints. For this purpose, we repeat our data analysis, but rescale the emulated power spectrum for every redshift by a factor of 0.94 independent of  $k$  and model parameters. In Figure 4.18 we show our fiducial analysis (blue) compared to this "corrected" measurement (green). We can see that the rescaling leads to a  $\sim 0.5\sigma$  to  $1.2\sigma$  higher  $T_0$  and lower  $\gamma$  for all  $2.2 \leq z \leq 4$ . Therefore, our measurement is clearly limited by the combined effect of box size and cosmic variance in this redshift range. Note that the change when applying this rescaling is such that the inferred  $\gamma$  is reduced, i.e. the discrepancies we analyzed in § 4.4.2 become weaker.

Simulations also suffer from statistical variance for the largest modes where the sampling is poor. To better understand this issue we ran simulations with different initial conditions but an otherwise identical setup. The comparison of those runs to our default simulation is shown in the middle panel of Figure 4.18. We can clearly see, that even with just 4 samples of initial conditions a  $\sim 5\%$  change in the power can be reached on small scales similar to the results in the boxsize test above. Additionally, the effect of cosmic variance on the largest scales (lowest  $k \lesssim 0.01 \text{ s km}^{-1}$ ) can exceed the 10% level, which is huge compared to the  $\sim 2\%$  errors of the BOSS measurement. To get both box

---

<sup>4.13</sup>Note that the initial conditions cannot be the same for two boxes of different size and so every comparison of this kind includes cosmic variance on both boxes, but with  $\sqrt{8}$  times lower amplitude at a given mode for the larger box.

#### 4.5. Systematic Effects on the Measured Thermal Evolution

size and cosmic variance effects under better control requires an analysis based on larger simulations, where doubling the (linear) box size would be expected to reduce cosmic variance by a factor of  $\sqrt{8}$  (but also needs at least eight times more computing time).

To understand the effect of cosmological parameters on the Ly $\alpha$  forest power spectrum we compare to three different cosmologies consistent with the Planck Collaboration et al. (2016b) results. Cosmology B & C were selected from their posterior distribution in order to differ as much as possible in the linear matter power spectrum (see Oñorbe et al., 2017b). Cosmology D uses the same parameters as in Lukić et al. (2015). The right panel of Figure 4.18 shows that a change in cosmological parameters within the current CMB constraints can lead to a  $\sim 5\%$  change in the flux power as well. Of course a more detailed analysis of this effect is needed and ideally one would marginalize over cosmological parameters adding additional dimensions to our simulation grid. However future independent higher precision cosmological constraints from either joining existing datasets or new measurements will reduce the strength of this effect.

Finally, the finite resolution of the simulations is not an issue at  $z \lesssim 4$  (see Figure 11 in Lukić et al., 2015, showing convergence to 1% at  $z \leq 3$  and to better than 5% at  $z = 4$ ), but might be of some importance at  $z \gtrsim 5$  (see Appendix of Oñorbe et al., 2017b) and might be more severe in exceptionally cold models as pressure smoothing is then weaker and structures are thus harder to resolve. In the latter case the power at the smallest mode covered in our analysis could be underestimated at the  $\sim 10\%$  level which is comparable to its errorbars. However, in contrast to box size effects only the smallest scales ( $k \gtrsim 0.07 \text{ s km}^{-1}$ ) are affected which will not lead to changes as dramatic as seen for the other modeling errors considered in this section. However, the scale dependence of this effect, large scales (small  $k$ ) being nearly unaffected while small scale power is reduced in the model, might lead to slightly underestimated results on  $T_0$ .

In summary, we have seen that all four effects we discuss in this section, box size, initial conditions, cosmology, and resolution can affect the power spectrum by a similar amount as our statistical measurement errors at least for some range of scales and redshifts. We have seen that these effects can be comparable or larger than our statistical errors

#### 4. *A New Measurement of IGM Thermal Evolution at $1.8 < z < 5.4$*

on the power spectrum, and can thus systematically change our thermal evolution at the  $0.5$  to  $1\sigma$  level at a range of redshifts. Note again that all the effects we considered here are converged at the  $\sim 5\%$  level and a better treatment of any of the effects would require additional computation time or reduce the number of simulations that can be performed thereby increasing interpolation errors. The current analysis is therefore the best compromise between accurate results and available computing time. But note that the effects discussed here, might very well explain some of the discrepancies between constraints of the thermal state obtained by different groups.

### 4.6. Summary

In this chapter, we presented the first uniform thermal evolution analysis based on the Ly $\alpha$  forest power spectrum covering a large redshift range from  $z = 5.4$  to  $z = 1.8$  or equivalently a timespan of nearly 3 Gyr. For this purpose we combined multiple high-precision measurements performed by several groups using different instruments. Furthermore, we compare this dataset with a large grid of high-resolution hydrodynamical simulations to connect the measured Ly $\alpha$  forest to physical properties of the IGM. To interpolate between these simulations we developed a Gaussian process emulation scheme and take its errors into account using a cross-validation approach. Compared to previous results we measure thermal evolution from high redshifts  $z = 5.4$  to the limit of Ly $\alpha$  forest observability with ground based telescopes due to the atmospheric UV cutoff at  $z \sim 1.8$ , and our combination of high-precision low- $k$  measurements with our new high- $k$  analysis allows us to break the well known degeneracy between the temperature at mean density and the slope of the TDR. Our analysis thus provides the first comprehensive homogeneous analysis of IGM thermal evolution probing times as early the end stages of H I reionization, extending through the epoch of He II reionization, and spanning the era of galaxy formation.

Our primary results are measurements of  $T_0$ ,  $\gamma$ , and  $\lambda_p$  (see Table 6) marginalizing over the mean transmission in two different ways (with a flat prior or a Gaussian prior

based on recent measurements). These measurements show a clear increase in  $T_0$  from  $T_0 \sim 6000$  K at  $z = 5.4$  to  $T_0 \sim 14000$  K at  $z = 3.4$  followed by a decrease reaching  $T_0 \sim 7000$  K at  $z = 1.8$ . We compared our results to published thermal evolution constraints using different statistics and find broad consistency with data from curvature, Voigt profile fitting and the phase angle distribution analyses. Comparing to simulations we indeed see compelling evidence for He II reionization in the rise of  $T_0$  which is not expected in absence of He II reionization. In general the thermal parameters we obtained from fitting the power spectrum measurements agree well with models for which He II reionization is complete at  $z \sim 3$ . At later times, i.e.  $z < 3$ , we see the first conclusive evidence that the IGM is cooling down after the last reionization heating episode driven by adiabatic cooling due to the expansion of the universe.

However, at the highest redshifts  $z \geq 5$  we find evidence for low temperatures  $T_0 \sim 6000$  K (slightly higher, but consistent with other measurements based on the same dataset) that might be hard to explain with our current understanding of the shape of the UVB at those redshifts as well as our current understanding of H I reionization. This is especially important as the same dataset resulting in these low temperatures is also places the most stringent limits on the mass of WDM (Viel et al., 2013b). Comparing these power spectrum measurements to models that include both WDM particle mass as well as the IGMs thermal history as free parameters would necessarily result in an even colder IGM, because small-scale structure in the Ly $\alpha$  forest can now be erased by both thermal broadening and a finite WDM free-streaming length (see Figure 4.15, compare to Garzilli et al. 2017). Thus, given our current expectations for reionization heating, the cold temperatures we infer provide additional evidence for a cold dark matter universe.

In the next chapter we will extend the constraints on the power spectrum as well as the thermal state of the IGM towards lower redshifts  $z < 1$ .



## 5. Extending Thermal Evolution Measurements to Low Redshifts

Thermal evolution past He II reionization is expected to be well understood from a theoretical point of view. The overall thermal evolution of the IGM is by far dominated by cooling due to the expansion of the universe and heating due to photoionizations (McQuinn, & Upton Sanderbeck, 2016). Compared to the reionization epochs the mean free path for ionizing photons is now extremely long leading to a mostly uniform UVB and thus the details of reionization are forgotten. The IGM therefore cools down towards a thermal asymptote which only depends on the shape of the UVB as the primary source of heating. The goal of this chapter is to test these predictions, especially since further sources of heating have been brought forward in recent years, e.g. Blazar heating (Chang et al., 2012; Puchwein et al., 2012) or dark matter decay (Araya, & Padilla, 2014).

However, as the Ly $\alpha$  forest is unobservable from the ground at  $z < 1.6$  (due to the atmospheric UV cutoff at  $\lambda_{\text{cutoff}} \sim 3300 \text{ \AA}$ ) there have been few previous measurements of the IGM's thermal state long after reionization (e.g. Ricotti et al., 2000; Davé et al., 2001). In fact to obtain constraints from the low redshift Ly $\alpha$  forest UV spectroscopy from space is needed. Data can currently only be gathered with the Space Telescope Imaging Spectrograph (STIS) (most efficient in the near UV for  $\lambda \gtrsim 2300 \text{ \AA}$ , i.e. for the Ly $\alpha$  forest at  $z \gtrsim 0.9$ ) and COS (which is especially efficient in the far UV (FUV)  $\lambda \lesssim 1800 \text{ \AA}$ , i.e.  $z \lesssim 0.5$ ) on the HST which is far more costly than optical ground based observations. As a successor for this telescope is not expected to launch within the next decade, any permanent failure of HST could shut this window completely.

## 5. Extending Thermal Evolution Measurements to Low Redshifts

To put a constraint on the IGM’s low redshift thermal state we therefore use archival COS/FUV spectra. From those we compute the power spectrum in an equivalent way to chapter 3. Using essentially the same approach applied in chapter 4 then allows us to derive a joint constraint on the thermal state as well as the UVB amplitude at  $z = 0.2$ .

This chapter is organized as follows. In § 5.1 we introduce the dataset on which we perform our analysis and note important changes in our power spectrum analysis due to the peculiarities of working with COS. The power spectrum result is then presented in § 5.3 for 5 redshift bins. We then obtain our measurement of the thermal state as well as the UVB for a subset of those bins in § 5.4.

### 5.1. Dataset

To measure the low-redshift power spectrum, we use the high-quality medium-resolution ( $R \sim 15000\text{--}20000$ , but with a non-Gaussian LSF) HST/COS FUV survey by Danforth et al. (2016) which comprises one of the largest low- $z$  IGM samples to date. The survey contains 82 spectra of  $z_{\text{em}} < 0.72$  QSOs and covers the Ly $\alpha$  forest at  $z < 0.48$ . The observations were obtained with the G130M and G160M gratings from 2009 to 2013. Danforth et al. (2016) have co-added individual spectra (across both gratings whenever available) to get continuous coverage across the FUV. They also fitted continua to each spectrum and identified nearly all individual absorption and emission lines. We use the publically available version of this dataset<sup>5.1</sup>.

To calculate the flux power spectrum,  $P(k)$ , we mask the metal lines arising from either intervening absorption systems or the ISM of the MW, all emission lines including geocoronal airglow emissions, low quality data having  $S/N/\text{pix} < 5$  which occur at the edge of a few spectra, and all gaps in the spectral coverage. In contrast to our previous high-redshift analysis the masking of metal absorption (and also emission) systems will prove to be important for this analysis on all scales of interest (see § 5.3). To illustrate our masking procedure, we show two chunks of spectra in Figure 5.1. We can see that the

---

<sup>5.1</sup><http://archive.stsci.edu/prepds/igm/>

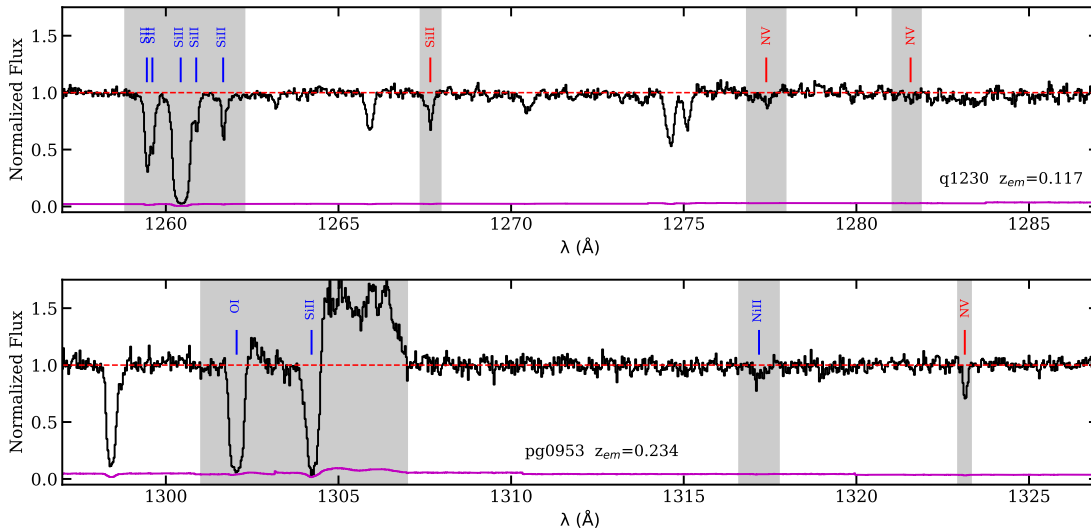


**Figure 5.1:** Illustration of our masking procedure. Each panel shows a chunk of one quasar spectrum (transmission in black, uncertainties in magenta, continuum level as a dashed red curve, quasar name and redshift in the legend). Shaded regions show our masking. Ticks indicate metal absorption features that were identified and fit by Danforth et al. (2016), blue shows contamination from the Milky Way (MW) interstellar medium (ISM) while red signifies intergalactic absorption. We also mask geocoronal airglow emissions, which is visible e.g. in the region around  $\lambda \sim 1305$  Å in the bottom panel and in this case is associated with OI.

low- $z$  Ly $\alpha$  forest consists mostly of unabsorbed quasar continuum and contains relatively few absorption lines (compare to the high- $z$  example in Figure 3.2). This allowed a clear identification of most metal absorption lines (ticks in the plot) visible. As we can identify and mask individual lines, in total we apply less masking than in the high- $z$  analysis and do not require as strong a masking correction as in § 3.2.2. While we do not mark Ly $\alpha$  absorption lines explicitly in Figure 5.1, most of them have been unanimously identified utilizing higher order Lyman series lines available in the spectra. We tested for the effects of the masking window on models and found that the effect is negligible compared to the expected uncertainties of the analysis.

For the power spectrum calculation we again conservatively used the restframe wave-

## 5. Extending Thermal Evolution Measurements to Low Redshifts

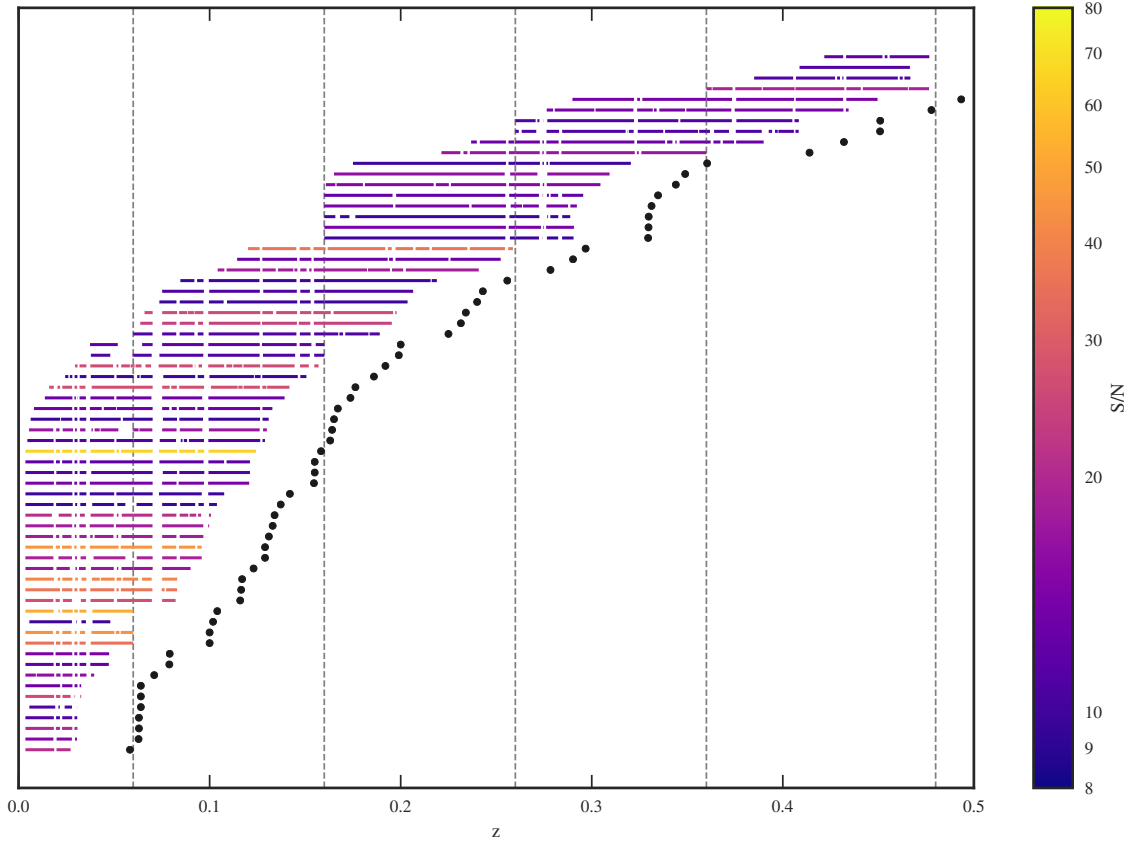


**Figure 5.2.:** The redshift path covered by the Lyman- $\alpha$  forest sample from Danforth et al. (2016) that we used for our low redshift power spectrum measurement color coded by  $S/N/\text{pix}$ . Horizontal lines indicate the Lyman-alpha path excluding proximity regions (rest frame 1050 to 1180Å), filled circles show the emission redshift of quasars (QSOs) and vertical dashed lines mark the boundaries of our redshift bins (i.e, 0-0.6, 0.06-0.16, 0.16-0.26, 0.26-0.36 and 0.36-0.48). Gaps in the horizontal lines show masked regions of spectra containing metal lines, emission lines, spectral-gaps, and bad data. White bands protruding through many spectra originate in significant MW ISM lines. The widest of those bands also contain geocoronal emission, e.g. the feature at  $z = 0.073$  is the same feature we highlighted in Figure 5.1.

## 5.2. Adjustments in Methodology due to COS Peculiarities

length range from 1050 Å to 1180 Å to avoid the QSO proximity zones as well as any contamination by higher order Lyman absorption or continuum systematics close to emission lines<sup>5.2</sup>. After masking and choosing the relevant wavelength range, we calculate the median S/N per pixel in the remaining pixels of the 82 quasar spectra and apply a cut of  $S/N/\text{pix} > 10$ . In Figure 5.2 we show the redshift path covered by the non-rejected data. The gaps in the horizontal lines show our masking and the lines are color coded by  $S/N$ . The alignment between some gaps across many different spectra in redshift shows where MW ISM lines were masked which contrary to intervening absorbers always fall at the same observed wavelength.

We bin the total redshift path covered by the spectra into five redshift bins. The first bin is chosen from  $z = 0.005$  to  $0.6$  to remove any systematics arising from both the core and the extended wings of the geocoronal Ly $\alpha$  emission line. The next three bins ( $z = 0.06 - 0.16$ ,  $z = 0.16 - 0.26$  and  $z = 0.26 - 0.36$ ) are chosen with the same width ( $\Delta z = 0.1$ ) and also because the mean redshift of the Ly $\alpha$  forest in these bins is centered at  $z = 0.1, 0.2$  and  $0.3$  thereby facilitating comparisons to previous analyses of the low- $z$  IGM focused on the UVB (e.g Shull et al., 2015; Gaikwad et al., 2017a; b). The last redshift bin ( $z = 0.36 - 0.48$ ) covers the remaining redshift-path covered by the data. Finally, in each redshift bin we removed short spectra that cover less than 10% of the redshift width of that bin leaving us with a dataset of 65 Quasars.

## 5.2. Adjustments in Methodology due to COS Peculiarities

For this analysis, we calculate the flux contrast  $\delta_F$  using the mean transmission inside each spectrum (instead of using an external measurement of  $\bar{F}$  as we did before). Note that the mean transmission is close to one here and the exact values assumed for it

---

<sup>5.2</sup>Note that in principle, as all absorption lines have been identified, one could mask all higher order Lyman series lines to obtain spectra of the Ly $\alpha$  forest that cover the whole range from  $\lambda \approx 1216$  Å to the quasar redshift, leaving a far longer path per spectrum and thus allowing to probe larger scales.

## 5. Extending Thermal Evolution Measurements to Low Redshifts

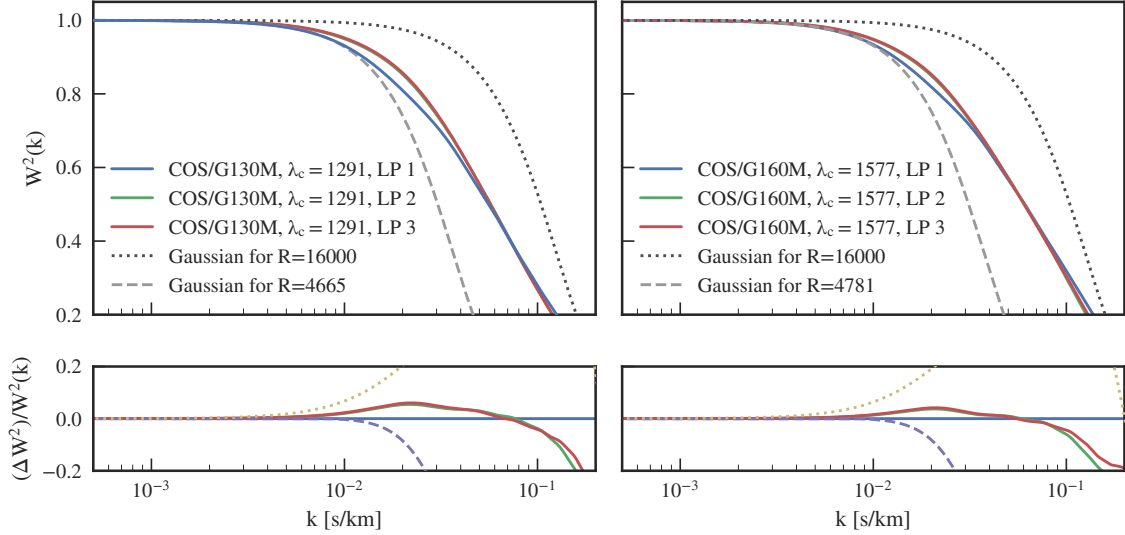


**Figure 5.3.:** Comparison of LSFs in Fourier space. Shown are the COS LSF for both medium resolution gratings (different columns) varying lifetime position (LP) (colored lines) and Gaussian LSFs with different resolutions for comparison. The Gaussian resolutions shown are the lower resolution quoted in the instrument manual (dotted curve) and the result of fitting a Gaussian LSF to the blue curve (dashed) on large scales  $k < 0.01 \text{ s km}^{-1}$ .

are therefore of less importance compared to high-redshift data. The power spectrum  $P_{\text{data}}(k)$  is then obtained following the same approach as before (see eqn. (3.3)), but with a modification regarding the resolution correction. Note that the COS LSF has significant wings on top of an approximately Gaussian core, i.e. pixels are correlated on far larger scales than would be expected from the narrow core itself. The reason for those wings ultimately lies in the polishing errors of the HST mirror.

We show the effect of the LSF on the power spectrum in Figure 5.3 by plotting the resolution dependent part of the window function  $W$  (i.e. we do not overplot the sinc function part due to pixelization). We compare the true LSF (colored lines) as tabulated on the COS webpage<sup>5.3</sup> to two different Gaussian LSFs. One of those approximately matches the nominal resolution of the instrument, i.e. the Gaussian core of the LSF,

<sup>5.3</sup> [http://www.stsci.edu/hst/cos/performance/spectral\\_resolution/](http://www.stsci.edu/hst/cos/performance/spectral_resolution/)

the other was fit to match the true LSF on large scales as close as possible. We can see that  $W^2$  is significantly non-Gaussian and affects large scale modes  $k \lesssim 0.01 \text{ s km}^{-1}$  in a similar way as an  $R \sim 5000$  instrument, but leaving significantly more structure on smaller scales until reaching the Gaussian core of the LSF (at  $k$  larger than the maximum value shown in the Figure 5.3). The effective resolution is also dependent the LP of the COS instrument, the grating used in the observation, and the central wavelength setting used. We used the corresponding Tables for the LP when the observations were taken which is LP1 or LP2 dependent on the spectrum.

As our data has been co-added from different central wavelength settings to avoid detector gaps and both the G130M and G160M gratings to get larger spectral coverage, the LSF for some spectra changes inside the spectrum and is not necessarily correctable by a simple division. At this stage we chose to divide out the LSF for the grating on which more than half the spectral pixels fall and to ignore the central wavelength completely as its effect is far lower, in fact curves for different central wavelength settings would be indistinguishable in Figure 5.3. Finally, the LSF is also wavelength dependent as the spectroscopic resolution (for a given grating) increases toward the red. To fully account for effects of spectroscopic resolution we generate forward models in the same way as in § 4.3.1, but now (instead of using a Gaussian, wavelength independent LSF) convolving the model spectrum with the full wavelength dependent LSF and taking into account that for some spectra both gratings are used assuming a switch of gratings at  $\lambda = 1450 \text{ \AA}$ .

### 5.3. Power Spectrum Measurement

In Figure 5.4, we show the  $z < 0.5$  power spectrum obtained at the 5 different redshift bins from  $k = 10^{-3} \text{ s km}^{-1}$  to  $0.15 \text{ s km}^{-1}$  (black points). We can clearly see that the data probes the small scale cutoff until  $k \sim 0.1 \text{ s km}^{-1}$  with a precision of  $\sim 15\%$  and is thus usable for obtaining constraints on the thermal state of the low- $z$  IGM. Note that for the very smallest scales ( $k > 0.01 \text{ s km}^{-1}$ ) the measurement is limited by noise subtraction and not so much by residual metal contamination which has been identified and removed.

## 5. Extending Thermal Evolution Measurements to Low Redshifts

We are also able to still probe large scales of  $k \sim 1.5 \times 10^{-3} \text{ s km}^{-1}$  with 25% precision.

Figure 5.4 also shows an additional version of our measurement where we did not mask any metal absorption lines, but still masked any other feature e.g. airglow emission (green points). We can see that while for some  $z \geq 0.2$  additional power due to metal lines is visible, but only changes the power spectrum estimate on the zero to few  $\sigma$  level, at the lowest redshifts  $z \leq 0.1$  this contamination is the dominant component of the power spectrum. This is caused by strong MW absorption lines, which appear in most spectra for these redshifts and are correlated with each other as they always have the same separation (see white vertical bands in Figure 5.2). Therefore we expect to have peaks in the correlation function corresponding to the separation of each pair of MW lines. While an individual such correlation just adds a sine wave pattern (see e.g. § 3.2.7) to the power, the superposition of many sine waves with different frequencies due to the different correlations changes the power more drastically.

Contrary to the high-redshift analysis, there is no clear trend in the redshift evolution of the low- $z$  power spectrum. While in our previous analysis, a higher redshift always corresponded to a higher overall power, in this low- $z$  measurement the large scale power for  $z \sim 0.1, 0.2$  and  $0.3$  is basically the same. However, such an evolution can be the result of a steeply evolving UV background  $\Gamma_{\text{UV}} \propto (1+z)^5$  (e.g. Shull et al., 2015; Gaikwad et al., 2017a)<sup>5.4</sup> combined with the evolution in density  $\rho \propto (1+z)^{3.5}$ <sup>5.5</sup> and the unknown thermal state of the IGM at these redshifts.

Assuming the optical depth is approximately described by eqn. (2.3), one obtains  $\tau \propto (1+z)/T_0^{0.7}$  using these redshift evolutions (for constant  $\gamma$  in this redshift range). Note that at redshifts  $z \sim 3$   $\Gamma_{\text{UV}}$  is nearly independent of redshift (Becker, & Bolton, 2013) leading to density evolution being the dominant effect on  $\tau$  which therefore evolves like  $\tau \propto (1+z)^6/T_0^{0.7}$ , far stronger than at low redshifts  $z \lesssim 2$ .

---

<sup>5.4</sup>This steep evolution is supposed to happen because sources at higher redshifts are dominating the UVB as quasar formation peaks at  $z \sim 2$  (Khaire, & Srianand, 2015).

<sup>5.5</sup>This is only the evolution of the mean density, in principle the overdensity corresponding to the Ly $\alpha$  forest features evolves as well which we ignore for this argument.

## 5.4. Measuring the Thermal State at $z < 0.5$

While the flux power spectrum at redshifts  $0.1 \leq z \leq 0.4$  was also presented by Gaikwad et al. (2017a), their power spectrum normalization is different from the standard conventions and cannot be easily reproduced in models as a renormalization was performed on each individual spectrum. Additionally they compute the power of the transmission  $F$  instead of using the flux contrast  $\delta_F$  which leads to a higher impact of continuum fitting errors. These differences complicate comparisons between the different analyses as well as comparisons of the Gaikwad et al. (2017a) data to simulations.

## 5.4. Measuring the Thermal State at $z < 0.5$

### 5.4.1. Changes in our Measurement Approach Compared to the High Redshift Analysis

To derive constraints of the IGM's thermal state at  $z = 0.2$  we again use the THERMAL grid of hydrodynamical simulations discussed in § 4.2. For each of the simulations in the heating rate rescaling grid an output at  $z = 0.2$  was already available. Additional simulations were run to cover the other redshift bins, but the analysis of those is not yet completed, nevertheless we will present preliminary results for the bins at  $z = 0.03$  and  $z = 0.4$ .

Due to the high mean transmission of the low- $z$  IGM and the increasing abundance of collisionally heated gas for lower redshifts<sup>5.6</sup> we changed our approach of generating different  $\bar{F}$ . Our previous approach of rescaling  $\tau$  to match a given  $\bar{F}$  is equivalent<sup>5.7</sup> to rescaling the total ionization rate by a factor. However, the only variable we have available here is the photoionization rate  $\Gamma_{\text{HI}}$  as changing collisional ionizations which only depends on hydrodynamical properties and is therefore not a free parameter. At high redshifts nearly all gas is photoionized, thus rescaling  $\tau$  effectively rescales  $\Gamma_{\text{HI}}$ .

---

<sup>5.6</sup>The so-called WHIM, which covers the upper left corner of Figure 1.2 with  $T \lesssim 1 \times 10^5$  K and  $\rho \lesssim 100\bar{\rho}$  (Davé et al., 2010).

<sup>5.7</sup>This is true only in the regime of low column densities where wings of the Voigt profile are not important, but most of the Ly $\alpha$  gas fulfills this criterion

## 5. Extending Thermal Evolution Measurements to Low Redshifts

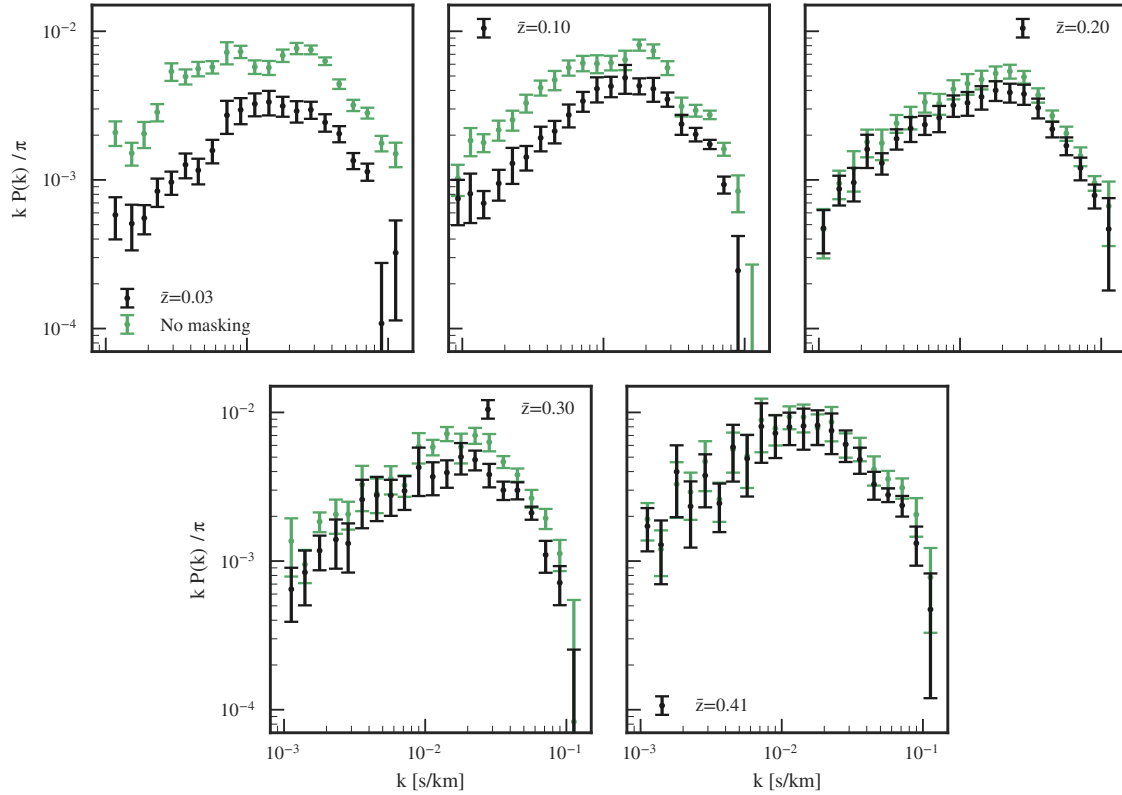


**Figure 5.4.:** Our measurement of the power spectrum at  $z \leq 0.5$  (black points) using our full data processing pipeline including subtraction of noise, correcting for the resolution window function and masking metal lines. The panels show different redshifts. For all the redshifts we measure the power from large scales to the thermal cutoff. For comparison we also show an analysis where we did not mask any intervening absorption systems (green points). We can clearly see that metals dominate the power spectrum in that case for  $z \leq 0.1$ . The likely cause for this is the increasing abundance of fairly strong MW absorption lines and their correlation with each other.

#### 5.4. Measuring the Thermal State at $z < 0.5$

At low redshifts  $z \lesssim 1$  this assumption is no longer true (see Figure 1.2) and therefore we recompute the skewers of  $\tau$  through the simulation assuming different UVB amplitudes keeping collisional ionizations fixed and redoing all Voigt profile convolutions (see the full description in § 4.2). We also decided to parametrize the models in our simulation grid by the photoionization rate  $\Gamma_{\text{HI}}$  instead of the mean transmission  $\bar{F}$  which is close to one for all models and thus compresses the photoionization values we have put in to a narrow dynamic range. We chose to generate 15 logarithmically spaced UVB amplitudes from  $\Gamma_{\text{HI}} = 4.4 \times 10^{-14} \text{ s}^{-1}$  to  $2.75 \times 10^{-13} \text{ s}^{-1}$  for  $z = 0.2^{5.8}$  bracketing a large range around the current constraints by Gaikwad et al. (2017b). We restrict ourselves to  $0.005 \text{ s km}^{-1} \leq k \leq 0.1 \text{ s km}^{-1}$ . Note that in principle for low redshifts boxsize effects are expected to become more important, e.g. due to the higher abundance of WHIM. But at the same time the power spectrum measurement at these redshifts is less precise. A detailed characterization of boxsize effects, however, is beyond the scope of this work.

As noted earlier we also changed our forward modeling to account for the wavelength dependent COS LSF. This was done by performing the convolution of each simulation skewer with the LSF in real space and evaluating the correct LSF, which is tabulated for up to 160 COS instrument pixels in each direction and which we interpolated to the pixel scale of the simulation, for each pixel in the process. Elsewise we used the same forward modeling approach as for high redshifts, i.e. we randomly selected a spectrum, stitched together as many simulation skewers as needed to arrive at the full length, convolved with the window function, applied noise with the same level as in the data, and computed the power in the same way as for the data. We used 50000 simulated skewers<sup>5.9</sup> for each forward model and again estimated the correlation matrix of the measurement from the simulation while obtaining the diagonal covariance matrix elements by bootstrapping

---

<sup>5.8</sup>For preliminary results on  $z = 0.03$  we chose 11 bins spanning from  $\Gamma_{\text{HI}} = 1.5 \times 10^{-14} \text{ s}^{-1}$  to  $8.3 \times 10^{-14} \text{ s}^{-1}$ , for  $z = 0.4$  we chose 9 bins from  $\Gamma_{\text{HI}} = 6.5 \times 10^{-14} \text{ s}^{-1}$  to  $2.2 \times 10^{-13} \text{ s}^{-1}$

<sup>5.9</sup>60000 for  $z = 0.03$  and  $z = 0.4$  that for those cases were extracted along all 3 directions of the simulation to reduce cosmic variance.

## 5. Extending Thermal Evolution Measurements to Low Redshifts

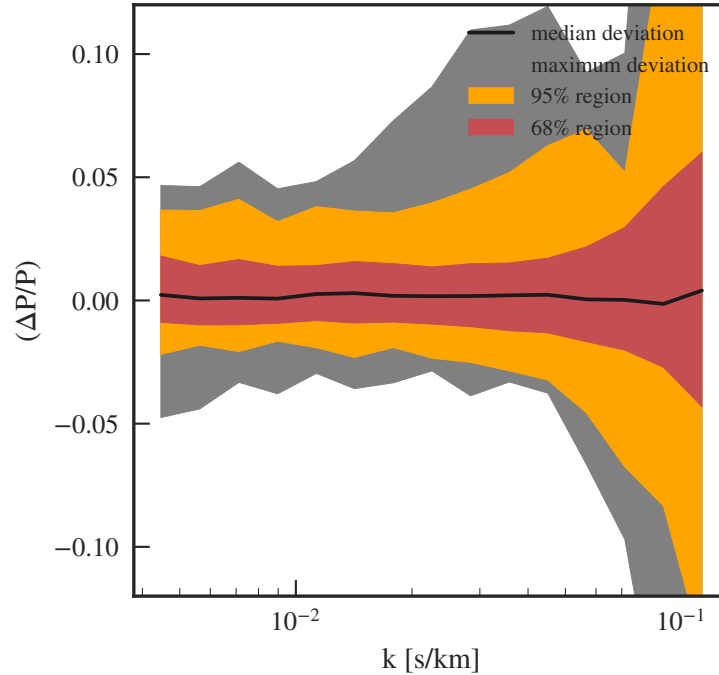


**Figure 5.5.:** The same as Figure 4.3, but showing the errors in the emulation at  $z = 0.2$ .

the data.

To infer thermal parameters we use these simulations and the emulation technique discussed in § 4.3.2. As any effects due to reionization are expected to be forgotten until  $z \leq 0.4$  and therefore  $\lambda_P$  is fully degenerate with  $T_0$  and  $\gamma$  for a redshift this low, we did not use additional explicit reionization models to generate the emulator and we also do not treat  $\lambda_P$  as a free parameter reducing the emulation process from four to three dimensions ( $T_0$ ,  $\gamma$  and  $\Gamma_{\text{HI}}$ ). We show the interpolation accuracy for this emulator in Figure 5.5. While they are significantly larger than at high redshifts, we note that those errors are fully propagated into the final results and are subdominant for most of the range in  $k$ . We also do not consider Si III correlations to be important for this analysis as every strong metal absorption line has been masked. We assume uniform priors on  $\log T_0$ ,  $\gamma$  and  $\log \Gamma_{\text{HI}}$  and keep our inference approach from the previous high redshift analysis unchanged, i.e. we use `emcee` to sample the parameter space via MCMC and

## 5.4. Measuring the Thermal State at $z < 0.5$

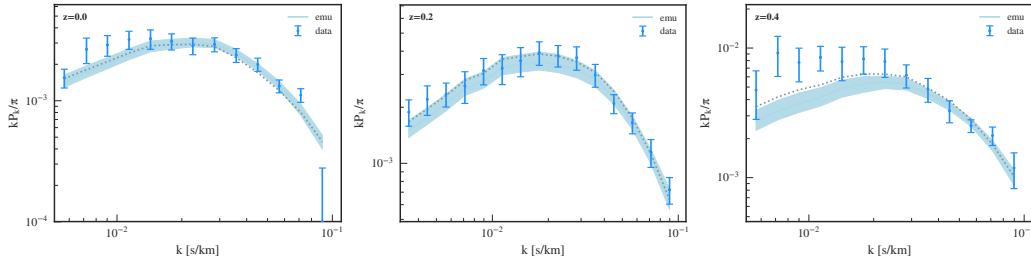


**Figure 5.6.:** Comparison between the measured power spectra at  $z = 0.03$ ,  $z = 0.2$ , and  $z = 0.4$ . The band shows the range of 68% best fitting models.

assume a multivariate Gaussian likelihood.

### 5.4.2. Thermal Evolution at Low Redshifts

In Figure 5.6 we show our fits using forward models to the measured Ly $\alpha$  forest power spectrum at  $z = 0.03$ ,  $0.2$ , and  $0.4$ . We can see that for  $z = 0.2$  a reasonable fit has been achieved for the whole range of  $k$ , and for the other redshifts the small scales are reasonably fit, while the large scales are not matched well. The reason for this mismatch is not yet clear, and we treat the resulting constraints as preliminary as the errors we obtain might be influenced by this mismatch.

We show the corresponding constraints on IGM parameters at  $z = 0.2$  in Figure 5.7 (as well as for the other redshifts in Figure 5.8 and Figure 5.9). Here, we can observe multiple features. First, we can see that the data constrains the degeneracy direction between  $T_0$  and  $\gamma$  well. However, as the low-redshift Ly $\alpha$  forest probes overdensities of a few (the degeneracy direction suggests  $\Delta \sim 3$  for  $z = 0.2$ ) results between  $T_0$  and  $\gamma$  are strongly correlated and thus the marginalized constraints on each appear rather weak. We do not see the issues of extremely high  $\gamma$  to the same extent as in the high redshift analysis, while high values are still allowed, the theoretically expected values consistent with our confidence region.

In contrast to the high-redshift bins where we always measured strong correlations between thermal parameters and  $\bar{F}$ , the correlations between thermal parameters and

## 5. Extending Thermal Evolution Measurements to Low Redshifts

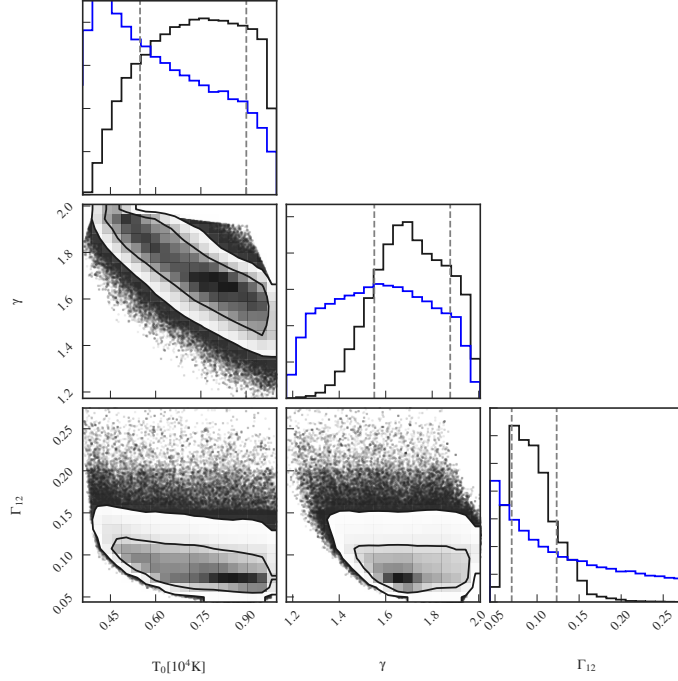


**Figure 5.7.:** Corner plot showing parameter constraints at  $z = 0.2$ . While the degeneracy direction between  $T_0$  and  $\gamma$  is well constrained, individual marginalized constraints are weak. However, the strength of the UVB  $\Gamma_{12} = \Gamma_{\text{HI}}/(1 \text{ s}^{-1})$  can be tightly constrained.

$\Gamma_{\text{HI}}$  seem to be rather weak. Therefore relatively strong constraints on the UVB can be obtained at  $z = 0.03$  and  $z = 0.2$ .

In Figure 5.10 we compare the thermal evolution from chapter 4 to our new low-redshift result. For comparison we show a band covering a range of explicit He II reionization models ranging from cold to hot (see Table 4.2 for the definition of those terms). We can see that independent of the exact heat input during He II reionization there is only a narrow range of thermal parameters generated for low redshifts. We can also see that in contrast to this a "no-HeII reionization" scenario produces a significantly colder IGM even at low redshifts. Our new low-redshift measurements are fully consistent with the predicted thermal state although with relatively large uncertainties. However, these uncertainties are still small enough to disfavor the "no-HeII reionization" model adding to

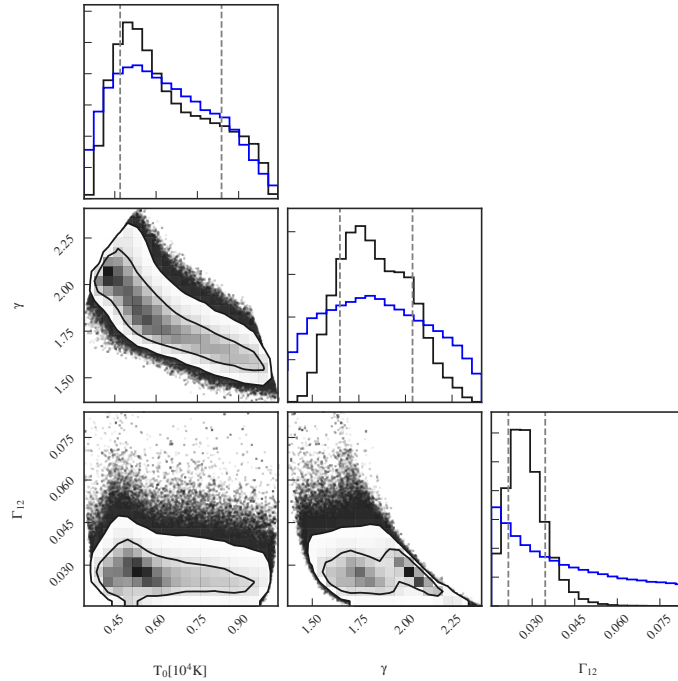


**Figure 5.8.:** Preliminary Parameter constraints for  $z = 0.03$ . While the degeneracy direction between  $T_0$  and  $\gamma$  is well constrained, individual marginalized constraints are weak. The amplitude of the UVB seems to be well constrained.

our previous constraint from high-redshift data. The fact that we obtain the temperatures expected for an IGM that is only heated by reionization and by photoionizations thereafter, should also allow to set limits on alternative heating scenarios, like e.g. Blazar heating or dark matter decay, but this analysis is beyond the scope of this work.

### 5.4.3. Constraints on the Low Redshift UV Background

For  $z = 0.2$ , we also obtain a  $\sim 30\%$  measurement of the amplitude of the UVB  $\Gamma_{\text{HI}}$  (see bottom right panel of Figure 5.7). While this has been measured before from the same dataset using a slightly different approach and a completely different set of simulations (Gaikwad et al., 2017a; b), this measurement provides an important cross-check for  $\Gamma_{\text{HI}}$  at a redshift where a photon underproduction crisis was previously claimed by

## 5. Extending Thermal Evolution Measurements to Low Redshifts

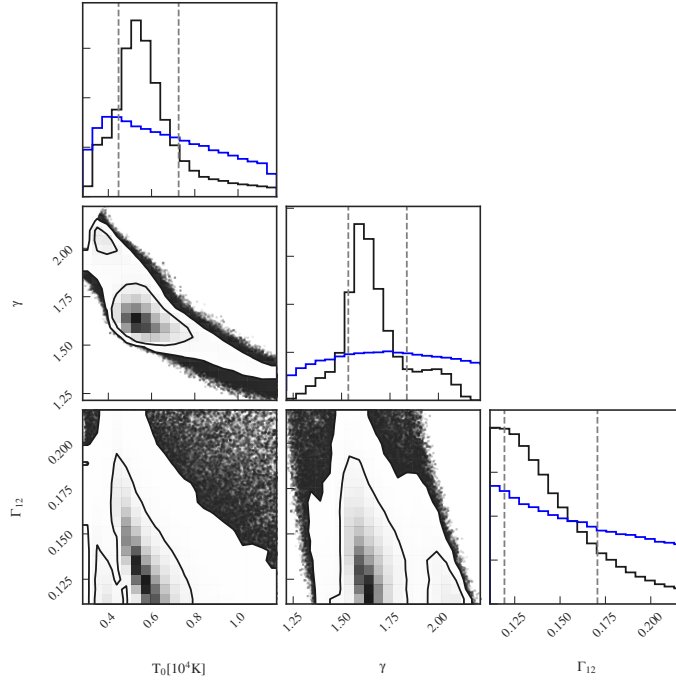


**Figure 5.9.:** Preliminary Parameter constraints for  $z = 0.4$ , we can see that while the the degeneracy direction thermal state between  $T_0$  and  $\gamma$  is well constrained, the UVB is strongly hitting the boundaries of our model grid which needs to be extended for a final result.

Kollmeier et al. (2014). This crisis consisted of a UVB measurement suggesting a five times higher photoionization rate than the most recent (at that time) models by (Haardt, & Madau, 2012) which would've demanded a high escape fraction for ionizing photons in low-redshift galaxies, in contradiction with current constraints. However, updated measurements by Shull et al. 2015 brought the discrepancy to only a factor of two which updated UVB models were able to explain (Khaire et al., 2015). The value we obtain is indeed consistent with the existing measurements by Gaikwad et al. (2017a) and Shull et al. (2015) based on different approaches and thus confirms the standard picture that at low redshifts quasars dominate the UVB. Performing the same analysis on the rest of our low-redshift power spectra data will generally enable us to track the evolution of the UVB and could also extend the redshift of available measurements further to the

### 5.4. Measuring the Thermal State at $z < 0.5$

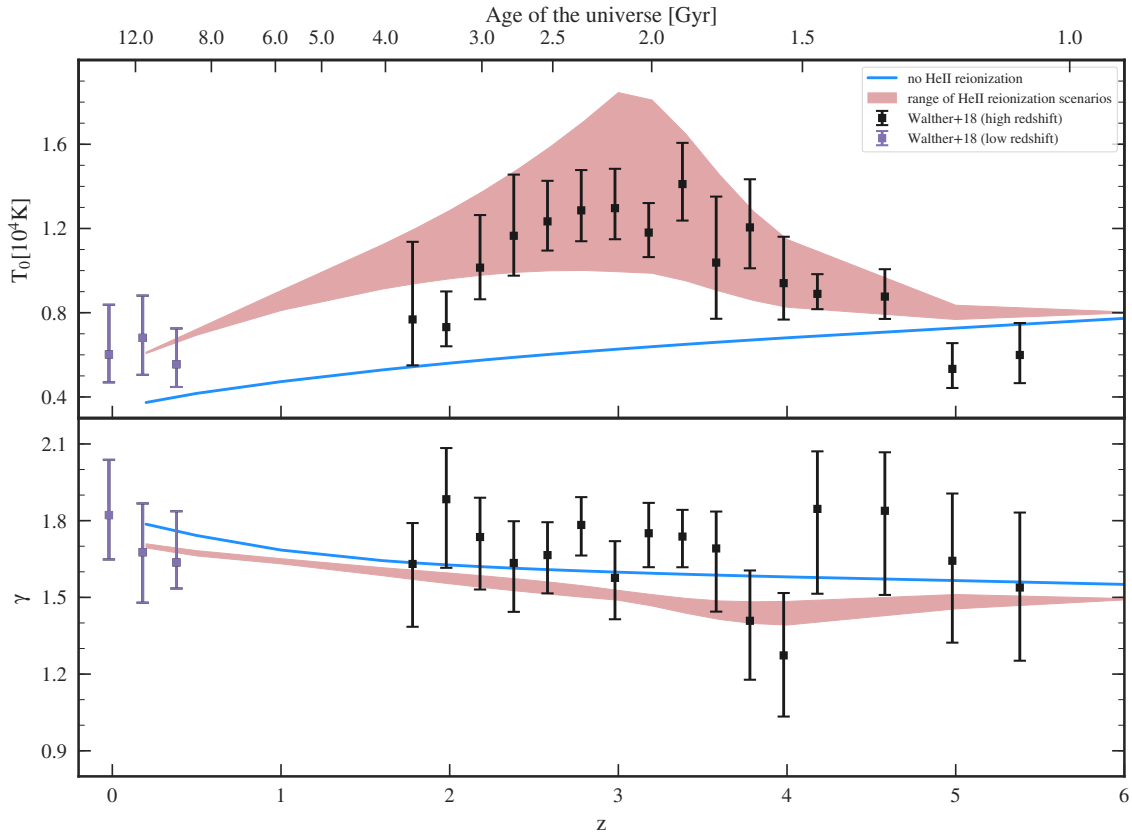


**Figure 5.10.:** Comparison of our low-redshift measurement to thermal evolution models (band showing the range from cold to hot He II reionization according to Table 4.2) and the high-redshift measurements from chapter 4. Note that the thermal state at  $z < 0.5$  is mostly independent of the amount of heat input during He II reionization and that our measurement nicely matches this prediction.

## 5. *Extending Thermal Evolution Measurements to Low Redshifts*

present day where currently only limits exist (Fumagalli et al., 2017).

### **5.5. Summary**

In this chapter, we extended our measurements of both the power and the thermal state to lower redshifts  $z < 0.5$ . As these observations cannot be performed from the ground due to the atmospheric UV cutoff, this required working with spectroscopic data from the HST. Fortunately, in the last few years, large datasets of far UV spectra have been collected with its COS instrument allowing us to perform a power spectrum measurement using 66 quasar spectra in this redshift range. While the thermal evolution measurement based on this dataset is not yet complete, we obtained the first constraint on the  $z = 0.2$  thermal state ever obtained, and provide preliminary measurements of the thermal state at  $z = 0.03$  and  $z = 0.4$ . All three datapoints are consistent with the standard picture of a cooling IGM in the post-reionization era. Additionally, our measurements also allow us to obtain constraints on the metagalactic UVB, providing further evidence for the absence of a photon underproduction crisis.

## 6. Conclusions and Outlook

In the present work, we obtained new measurements of the Ly $\alpha$  forest flux power spectrum at  $z < 0.5$  (low redshift) and  $1.8 \leq z \leq 3.4$  (high redshift) and used its sensitivity to the thermal state to constrain thermal evolution in the intergalactic medium over 12 billion years of cosmic history.

We presented the high redshift power spectrum in chapter 3. This measurement is based on archival high-resolution spectra obtained with the UVES and HIRES spectrographs which cover a pathlength of  $\sim 20$  cGpc several times larger than the previous high-resolution measurements at this redshift range (McDonald et al. 2000, Croft et al. 2002, and Kim et al. 2004). This allowed us to measure the small scale cutoff in the power spectrum and its redshift evolution with unprecedented precision. We analyzed the effects of contamination due to metal lines, the window function of masking those lines, and finite spectroscopic resolution and corrected for those effects using a forward modeling approach. Agreement with previous measurements from both low- and high-resolution spectrographs is generally good. However, especially the most recent measurements by Iršič et al. (2017a) and Yèche et al. (2017) seem to disagree with our result on small scales which we attributed to an improper characterisation of XSHOOTER’s spectroscopic resolution and a possibly improper correction in the measurements based on data from this spectrograph.

In chapter 4 we used the additional precision from our new measurement and showed that combining our results with low-resolution results from the BOSS survey by Palanque-Delabrouille et al. (2013) as well as existing higher redshift measurements (Iršič et al., 2017a; Viel et al., 2013b) results in a powerful new dataset for placing high precision

## 6. *Conclusions and Outlook*

constraints on thermal evolution in the IGM. In addition to this unprecedented dataset, our inference was based on the combination of large, high-resolution cosmological hydrodynamical simulations with powerful statistical techniques for interpolation, and MCMC sampling for parameter estimation. The resulting thermal parameter constraints conclusively show an epoch of heating and a subsequent cooling of the IGM. We compare to previous measurements of the IGM thermal state based on a variety of methods (Lidz et al., 2010; Becker et al., 2011; Boera et al., 2014; Bolton et al., 2014; Rorai et al., 2017b; Garzilli et al., 2017; Rorai et al., 2018; Hiss et al., 2018) and find reasonable agreement to most measurements. In comparisons to simulations we see evidence for a normal to warm He II reionization scenario based on the rise and fall of temperatures unexpected in the absence of this phase transition. We also measure particularly low temperatures at the very highest redshifts contained in this analysis that might be hard to understand in the context of H I reionization. As a low temperature inferred by our power spectrum measurement is a result of having more small scale structure (high- $k$  power) than expected, the same feature can be used to set a limit on other effects that erase structure in the IGM, e.g. free-streaming of WDM.

We extended the current measurements of both the power spectrum and the IGM's thermal state to lower redshifts  $z < 0.5$  in chapter 5. Due to the Earth's atmosphere being opaque in the UV, these measurements can only be performed using space based observations. We used an archival set of HST/COS spectra (Danforth et al., 2016), masked all identified metal lines, and developed additional techniques to fully treat the COS LSF. We obtained power spectra in five redshift bins and noted that especially at the lowest redshifts metal contamination has a far stronger effect than at high redshifts. We also noticed a nearly flat evolution of the power spectrum's overall normalization, a feature that is not found in high redshift measurements and could be explained by a steeply evolving UVB. Regarding the thermal state we performed a preliminary measurement in three of the five redshift bins. The results seem to be agreeing with the standard picture of the IGM that predicts a cooldown after the end of reionization leading to a small range of temperatures fully consistent with our measurement, thus further excluding a no

He II reionization scenario. Our new measurement also constrains the low redshift UVB, an area with a recently claimed "photon underproduction crises" (Kollmeier et al., 2014). This problem consists of a lack of ionizing photons at low redshift and was subsequently resolved by improved measurements (Shull et al., 2015; Gaikwad et al., 2017b) and modeling (Khaire, & Srianand, 2015). Our measurement is in perfect agreement with those more recent analyses disfavoring the crisis scenario.

After our analysis there are essentially two ranges of the IGM's history with an unconstrained thermal state. Due to a lack of Ly $\alpha$  forest data at  $0.5 < z < 1.6$ , there are essentially no constraints on the physical state of IGM gas in this redshift interval, representing 5 Gyr of the Universe's history. Note that observations of this regime need to be performed before the end of HST's mission, as likely no successor will be available for UV observations in the next decade or even decades.

Furthermore, to obtain a complete measurement of the IGM's thermal state, Ly $\alpha$  forest measurements clearly also need to be extended to higher redshifts. This would allow for testing the current power spectrum results at  $z > 5$  and enable stronger joint constraints on the thermal state just after HI reionization as well as the nature of dark matter (see Oñorbe et al., 2017a, for a forecast of possible constraints using high-resolution data up to  $z = 6$ ). The analysis of this redshift range will be enabled by the large increase in the available dataset size in recent years (e.g. Eilers et al., 2018, published a new medium resolution dataset, but more high-resolution data has been obtained as well).

However, to get accurate high-precision constraints of the thermal state in the IGM better hydrodynamical simulations are needed. We characterized the effect of box size, cosmic variance and cosmology and found, that for some range of scales systematic uncertainties due to these effects can be comparable to our measurement precision. Future progress will therefore rely on simulating larger grids to marginalize over cosmological parameters or alternatively a more precise external determination of those parameters as well as larger simulation boxes. Thanks to great improvements in recent years, allowing nearly linear scaling of computing time with volume (at fixed resolution) in some hydrodynamical simulation codes, and the current advancement of computing

## 6. Conclusions and Outlook

speed in supercomputers this will be possible within the next few years.

Finally, the power spectrum of the Ly $\alpha$  forest does not only constrain the thermal state of the IGM, but could also be used for measuring cosmological parameters. New measurements of this statistics based on several hundred thousand to millions of moderate resolution quasar spectra<sup>6.1</sup> will allow sub-percent level constraints on its large scale modes and are projected to allow a determination of the sum of neutrino masses  $\sum m_\nu$ , possibly allowing to discriminate between the normal and inverse mass hierarchy (e.g. Palanque-Delabrouille et al., 2015; Rossi, 2017). But this effort will rely on accurate treatment of systematic effects, i.e. due to degeneracies with the thermal state of the IGM. The greatly improved high- $k$  precision enabled by our work will help break these degeneracies, and thereby enable improved constraints on neutrino masses, but e.g. also on alternatives to the CDM paradigm such as warm (Viel et al., 2013b; Iršič et al., 2017b) or fuzzy dark matter (Hui et al., 2017; Iršič et al., 2017c).

---

<sup>6.1</sup>These will be obtained from the Dark Energy Spectroscopic Instrument (DESI) (DESI Collaboration et al., 2016) and WEAVE (Pieri et al., 2016) spectroscopic surveys (both are expected to launch science observations in 2019), the 4-metre Multi-Object Spectroscopic Telescope (4MOST) (de Jong et al., 2016) survey is expected to add to this as well (starting in 2021)

# Appendix

## A. Impacts of seeing on power spectrum measurements

For slit spectrographs, it is very difficult to know the exact resolution because it depends on the seeing, and also the resolution can vary at the  $\sim 10\%$  across the echelle orders, which is typically never carefully quantified or taken into account (e.g. the X-SHOOTER pipeline user manual Modigliani et al., 2017, shows variations in the slit resolution with wavelength at about this level). Note that the change of resolution with seeing is not a problem for fiber spectrographs (such as e.g. BOSS) that allow measurements of the resolution of the science data on sky fibers. Assuming the same resolution for each object (whereas the objects actually have different resolutions) generally will also increase the weight of higher resolution data in the power spectrum averages. This is because higher resolution data has a smaller scale (higher  $k$ ) cutoff. Therefore, a higher power by a factor that is exponential in  $k$  as well as in  $R$  would be measured. When performing the mean over all objects the higher resolution objects (which now have been overcorrected) will bias the power estimate as  $\langle \exp(k^2 R^2) \rangle > \exp(k^2 \langle R \rangle^2)$  (if  $R$  is not constant throughout the dataset). As explained in Yèche et al. (2017) this problem can be weakened by measuring the seeing from the data (e.g. by measuring the width of the object in the spacial direction) and correcting each spectrum using its correct seeing.

A similar biasing due to mixing different resolutions can appear already during data reduction because co-adding overlapping echelle orders as well as different observations

## *Appendix*

will give higher weight to data with better seeing as this typically has higher S/N as well. If resolution varies strongly between echelle orders or observations, the final co-added spectrum might be dominated by the best resolution obtained. Therefore, a knowledge of the spectrograph resolution for each individual object on the  $< 10\%$  level as well as an individual resolution correction for each object are needed to provide an accurate measurement.

## **B. Slit resolution of the X-SHOOTER spectrograph**

The quoted resolution in the X-SHOOTER manual was originally 5100 for the same slit/arm combination and was changed to 4260 during a recalibration run in 2011 (so before XQ-100 data was taken). The full reason for this change in value between calibrations is unclear to the authors. However, the X-SHOOTER Pipeline manual (Modigliani et al., 2017) shows values more consistent with the higher resolution<sup>1</sup>. The manual also claims an underestimation of resolution by the pipeline for the 1x1 binning in the UVB arm. Additionally, the reduction QC plots in the ESO archive for 1x1 binning and 1x2 binning (which XQ-100 used) for all measurements between 2012 and 2014 shows  $\sim 20\%$  higher values for the pipeline resolution values with the 1x2 binning. We contacted ESO about this issue and found out that the difference in estimated resolution for different binnings is still an open problem. A determination of the instruments' slit resolution to the accuracy needed for small scale power analyses is therefore not available.

This motivated us to estimate the X-SHOOTER resolving power for the UVB arm and the configuration used in the XQ-100 dataset (0.1'' slit width and a  $1 \times 2$  binning) from a slit-arc spectrum (taken at 2012-05-20T17:06:41.424) reduced in the same way as one would do for science data using the ESO Pipeline recipe `xsh_scired_slit_stare`.

---

<sup>1</sup>Note that the resolution values quoted on the ESO webpage were again significantly changed towards higher values since this part of the analysis was published in (Walther et al., 2018a). See here for the previous webpage: <https://web.archive.org/web/20180208222115/http://www.eso.org:80/sci/facilities/paranal/instruments/xshooter/inst.html>

## B. Slit resolution of the X-SHOOTER spectrograph

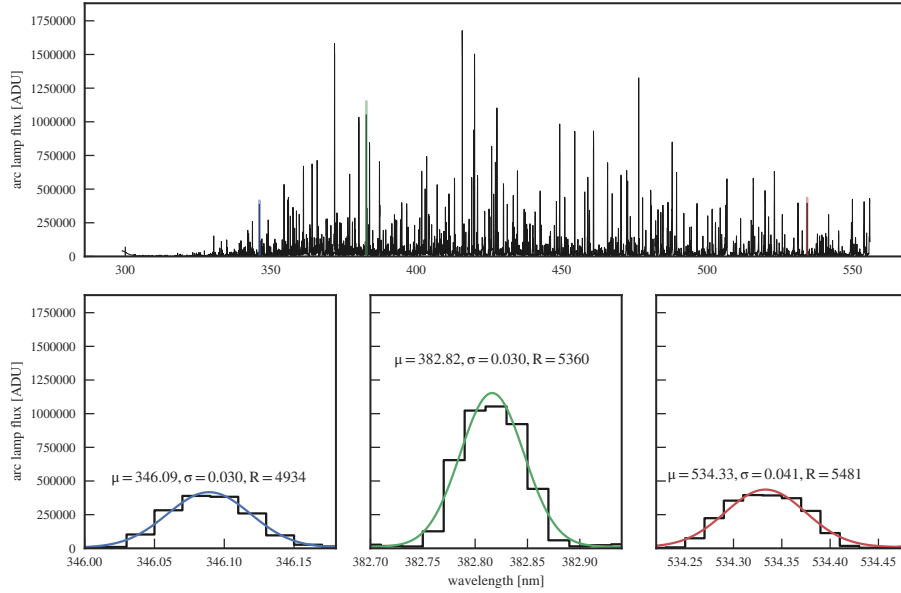


**Figure 1.:** A reduced slit-arc spectrum of the UVB channel with the same slit width and binning as the XQ-100 survey and reduced with the `xsh_scired_slit_stare` recipe of the ESO X-Shooter Pipeline using the same calibrations as for science data reductions (except for the response curves and disabling sky-subtraction). The full arc spectrum is shown in the top panel, colored lines indicate the position of zoom-ins in the bottom panel. The bottom panels also show Gaussian fits (colored lines) to three of the arc lines with the best-fit parameters (mean  $\mu$ , standard deviation  $\sigma$ , both in nm) as well as the resulting resolving power  $R$  printed as text. We can clearly see that the resolution of each of those fits is exceeding the nominal value (taken from the XQ-100 data release paper) of  $R = 4350$  and is varying over the spectrum.

These frames are taken on a regular basis using the same slits used for science targets. A normal reduction process (at least with the ESO pipeline) does not need those frames as the wavelength calibration is performed using pinhole arcs which cannot be used to determine the resolution of science data. In Figure 1 we show the reduced slit-arc spectrum as well as zoom-ins to three random, non-blended lines in different parts of the spectrum. We fitted the lines with Gaussian profiles which show that the resolution of X-SHOOTER in the UVB arm a) varies within the arm by at least  $\sim 10\%$  and b) can be  $\sim 25\%$  higher than the value quoted in the XQ-100 data release paper (López et al., 2016).

## Appendix

We also performed a quick automated fit for all lines in the arc line list individually without checking for line blends and other kinds of contamination. These might make some fits broader than a single line leading to determining a lower resolution. The resulting resolution with respect to wavelength is shown in Figure 2. We do not observe a clear trend with wavelength and note that the bulk of the distribution agrees with  $R \sim 5000$ .

These tests are in basic agreement with the QC plots in the ESO archive as well as the pipeline manual. We therefore assume that the resolution values given in the automatic QC plots are right and use their approximate median of  $R = 5350$  when performing further tests of the XQ-100 results. If one only determines the seeing and estimates spectral resolution by combining the seeing with the slit resolution quoted on the ESO website or X-SHOOTER manual one might therefore under-determine the true resolution of the spectra. In principle one should be able to obtain the slit resolution from sky-lines in the science observations as well (albeit with less available lines and worse signal to noise than for the arc spectra) as motions in the atmosphere are slower than the  $\sim 1 \text{ km s}^{-1}$  resolution accuracy we want to obtain.

## C. Normalization Conventions for the Power Spectrum

While Kim et al. (2004) as well as the SDSS/BOSS/XQ-100 measurements already used the same normalization as we do, Croft et al. (2002) and McDonald et al. (2000) measure the power of the transmission  $F$  instead of  $\delta_F$ . This leads to an additional factor  $\bar{F}^2$  between their measurements and the more recent ones. The Croft et al. (2002) measurement also has a different normalization convention by a factor 2 compared to McDonald et al. (2000) which we corrected for. The former also does not provide a measurement of the mean transmission of their sample. Therefore we renormalized the McDonald et al. (2000) measurement using the provided mean transmission of their sample and rescaled the

### D. Data Products for the Power Spectrum Measurement

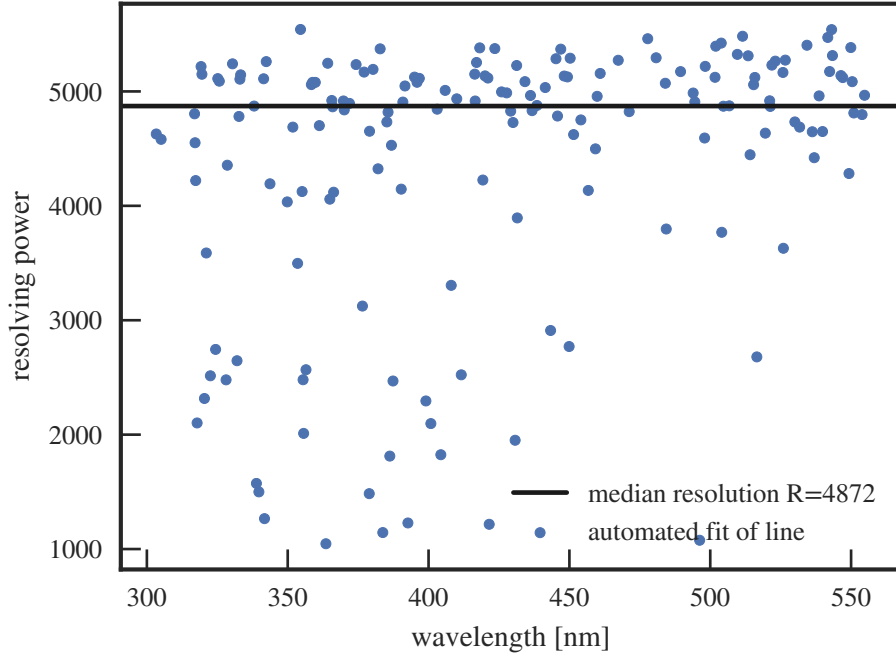


**Figure 2.:** Full slit resolution with respect to wavelength for the X-SHOOTER spectrograph estimated from the spectrum in Figure 1. We show the resolution for a quick fit of individual lines in the arc spectrum based on the line list provided by ESO. Obviously unphysical or unconverged fits have been removed. As fits to blends have not been removed, spurious low-resolution fits are included inside the figure.

Croft et al. (2002) with the external mean transmission measurement by Becker et al. (2013).

## D. Data Products for the Power Spectrum Measurement

Truncated data tables showing our high-resolution measurement at  $z = 2.8$  are shown in Table 2 (including our metal masking approach) and Table 3 (without metal masking). We also show the first and last column of the correlation matrix at  $z = 2.8$  in Table 4. Note that the correlation matrix is based on the best-fitting DM only simulation. It is

## Appendix

therefore a model dependent quantity although the agreement of the fit with the data is good. Thus, while it should give a good representation of data correlations, for fitting models to the measured power spectra you might want to estimate the correlation matrix from the actual model fitted in the analysis to be fully independent of our modeling. The full tables including all redshifts and  $k$ -bins are available in the electronic version of Walther et al. (2018a) Masked spectra (with and without enabled metal masking) can be obtained from the Zenodo upload under Walther et al. (2017)<sup>2</sup>. Random samples from our  $f_{\text{window}}$  chain can be found therein as well.

## E. Tables of the Measured Thermal Evolutions

In this section we tabulate our measurement values at each redshift for the flat prior on  $\bar{F}$  (Table 5) and the strong prior (Table 6). Those tables do not only show the marginalized constraints of all thermal parameters, but additionally show values for the temperature at the overdensity  $\Delta_{\star}$  where curvature measurements are optimal (with the value for  $\Delta_{\star}$  interpolated in redshift between results from Becker et al., 2011) as well as at  $\Delta_{\text{power}}$  where the degeneracy between  $\gamma$  and  $T$  is minimized for the power spectrum. The latter was obtained by assuming a power law relation  $T(\Delta_{\text{power}}) = T_0 \Delta_{\text{power}}^{\gamma-1}$  to the samples in our Markov chains and varying  $\Delta_{\text{power}}$  such that the variance of  $T(\Delta_{\text{power}})$  is minimized. The density values where degeneracies are minimal are tabulated as well. We will provide chains from our MCMC analysis on request.

---

<sup>2</sup><https://zenodo.org/record/1041022>

*E. Tables of the Measured Thermal Evolutions*

**Table 1:** Priors used for each fitting parameter

Parameter	type of prior	lower limit	upper limit	$\mu$	$\sigma$
$\log(T_0/\text{K})$	flat	3.48	4.30		
$\gamma$	flat	0.5	2.1		
$\log(\lambda_J/\text{ckpc})$	flat	1.34	2.18		
$f_{\text{Si III}}$	Gaussian	-0.002	0.018	0.008	0.001
$\bar{F}(z = 1.8)$	Gaussian	0.871	0.931	0.901	0.006
$\bar{F}(z = 2.0)$	Gaussian	0.785	0.976	0.881	0.019
$\bar{F}(z = 2.2)$	Gaussian	0.818	0.921	0.869	0.010
$\bar{F}(z = 2.4)$	Gaussian	0.766	0.859	0.812	0.009
$\bar{F}(z = 2.6)$	Gaussian	0.723	0.813	0.768	0.009
$\bar{F}(z = 2.8)$	Gaussian	0.683	0.771	0.727	0.009
$\bar{F}(z = 3.0)$	Gaussian	0.640	0.724	0.682	0.008
$\bar{F}(z = 3.2)$	Gaussian	0.581	0.661	0.621	0.008
$\bar{F}(z = 3.4)$	Gaussian	0.528	0.602	0.565	0.007

Note. — priors in  $\bar{F}$  are based on Kirkman et al. (2005) for  $z = 1.8$ , Faucher-Giguère et al. (2008b) for  $z = 2$  and Becker et al. (2013) for the higher redshifts

*Appendix*

**Table 2:** Measured flux power spectrum at  $z = 2.8$  after masking metals and removing the window function due to masking. Note that the full table that also includes the other redshifts and matrix elements is available in the electronic version of Walther et al. (2018a).

$\bar{z}$	$\bar{k}$ [s km <sup>-1</sup> ]	$kP_k\pi^{-1}$	$\sigma_{kP_k\pi^{-1}}$
2.795	0.002803	0.03103	0.009415
2.795	0.003499	0.03522	0.006892
2.795	0.004479	0.04468	0.008296
2.795	0.005632	0.04717	0.006015
2.795	0.00708	0.05932	0.007473
2.795	0.008945	0.05596	0.006969
2.795	0.0113	0.05733	0.005735
2.795	0.01425	0.06204	0.006429
2.795	0.01794	0.06517	0.005423
2.795	0.02259	0.05688	0.003983
2.795	0.02838	0.05032	0.002825
2.795	0.03573	0.04715	0.002449
2.795	0.04501	0.03812	0.002463
2.795	0.05666	0.02728	0.001632
2.795	0.07132	0.01872	0.001295
2.795	0.08978	0.01121	0.00106
2.795	0.113	0.00548	0.0005469
2.795	0.1423	0.002266	0.0003068
2.795	0.1792	0.0009699	0.000172
2.795	0.2255	0.0003949	9.197e-05
2.795	0.2839	0.0002304	3.592e-05
2.795	0.3574	0.0001749	2.872e-05

*E. Tables of the Measured Thermal Evolutions*

**Table 3:** Measured flux power spectrum at  $z = 2.8$  without masking of metals and after removing the window function due to masking. Note that the full table that also includes the other redshifts will be available in the electronic edition of the journal.

$\bar{z}$	$\bar{k}$ [s km <sup>-1</sup> ]	$kP_k\pi^{-1}$	$\sigma_{kP_k\pi^{-1}}$
2.797	0.002822	0.02772	0.007839
2.797	0.003539	0.03315	0.007177
2.797	0.004509	0.04198	0.006247
2.797	0.005635	0.04608	0.005853
2.797	0.007045	0.04969	0.006732
2.797	0.00895	0.05159	0.005478
2.797	0.01133	0.06545	0.006951
2.797	0.0142	0.06722	0.006563
2.797	0.01791	0.06762	0.004682
2.797	0.02264	0.06177	0.005428
2.797	0.02843	0.05868	0.003455
2.797	0.03575	0.04829	0.003225
2.797	0.045	0.04044	0.002322
2.797	0.05662	0.03103	0.002069
2.797	0.07131	0.02063	0.001187
2.797	0.08978	0.01292	0.001051
2.797	0.113	0.007671	0.0006593
2.797	0.1423	0.004842	0.0005712
2.797	0.1792	0.003066	0.0003734
2.797	0.2255	0.001638	0.0002774
2.797	0.2839	0.0008713	0.0001418
2.797	0.3574	0.0005683	0.0001228

*Appendix*

**Table 4:** Correlation matrix at  $z = 2.8$  for the measurement in Table 2. Note that the full table that also includes the other redshifts and matrix elements is available in the electronic version of Walther et al. (2018a).

$\bar{z}$	$\bar{k}$ [s km <sup>-1</sup> ]	$R_{1,j}$	...	$R_{n,j}$
2.8	0.002803	1		-0.08482
2.8	0.003499	0.1022		0.009749
2.8	0.004479	0.14		-0.05212
2.8	0.005632	0.1838		-0.02332
2.8	0.00708	0.1645		-0.002453
2.8	0.008945	0.112		0.04121
2.8	0.0113	0.03341		-0.04957
2.8	0.01425	0.07737		-0.07281
2.8	0.01794	-0.001218		0.04444
2.8	0.02259	0.05922		0.08884
2.8	0.02838	0.04739		0.1806
2.8	0.03573	-0.08184		0.2035
2.8	0.04501	-0.1025		0.2783
2.8	0.05666	-0.08604		0.3239
2.8	0.07132	-0.09288		0.4122
2.8	0.08978	-0.1069		0.5116
2.8	0.113	-0.07494		0.4853
2.8	0.1423	-0.0566		0.4612
2.8	0.1792	-0.0352		0.3981
2.8	0.2255	-0.03103		0.3749
2.8	0.2839	-0.06502		0.6858
2.8	0.3574	-0.08482		1

E. Tables of the Measured Thermal Evolutions

**Table 5:** Fiducial Evolution of Thermal Parameters Assuming a Flat Prior on  $\bar{F}$

$z$	$\lambda_P$ [kpc]	$T_0$ [ $10^4$ K]	$\gamma$	$\bar{F}$	$T_{\Delta_{\text{power}}}$ [ $10^4$ K]	$T_{\Delta_{\star}}$ [ $10^4$ K]
1.8	$79.0^{+16.0}_{-11.9}$	$0.684^{+0.180}_{-0.122}$	$1.97^{+0.16}_{-0.26}$	$0.872^{+0.020}_{-0.018}$	$1.160^{+0.239}_{-0.239}$	$4.288^{+2.162}_{-1.525}$
2.0	$93.0^{+8.3}_{-17.4}$	$0.734^{+0.093}_{-0.071}$	$2.15^{+0.09}_{-0.26}$	$0.831^{+0.033}_{-0.011}$	$1.096^{+0.122}_{-0.121}$	$5.749^{+1.011}_{-2.290}$
2.2	$91.0^{+6.3}_{-6.4}$	$0.789^{+0.085}_{-0.068}$	$2.13^{+0.09}_{-0.13}$	$0.796^{+0.010}_{-0.009}$	$1.369^{+0.120}_{-0.106}$	$4.942^{+0.773}_{-0.771}$
2.4	$87.2^{+5.4}_{-5.1}$	$0.831^{+0.112}_{-0.078}$	$2.07^{+0.13}_{-0.18}$	$0.772^{+0.013}_{-0.012}$	$1.593^{+0.143}_{-0.123}$	$3.995^{+0.717}_{-0.631}$
2.6	$88.3^{+3.7}_{-4.5}$	$1.000^{+0.146}_{-0.090}$	$1.93^{+0.15}_{-0.17}$	$0.745^{+0.012}_{-0.013}$	$1.936^{+0.095}_{-0.084}$	$3.449^{+0.445}_{-0.345}$
2.8	$93.8^{+4.2}_{-4.2}$	$1.000^{+0.112}_{-0.087}$	$2.16^{+0.09}_{-0.13}$	$0.688^{+0.013}_{-0.010}$	$1.982^{+0.163}_{-0.149}$	$3.911^{+0.426}_{-0.408}$
3.0	$80.6^{+6.0}_{-5.6}$	$1.429^{+0.313}_{-0.271}$	$1.47^{+0.26}_{-0.24}$	$0.694^{+0.009}_{-0.015}$	$2.027^{+0.155}_{-0.143}$	$2.347^{+0.269}_{-0.226}$
3.2	$84.9^{+4.7}_{-6.3}$	$1.115^{+0.230}_{-0.149}$	$1.85^{+0.21}_{-0.25}$	$0.623^{+0.018}_{-0.019}$	$1.910^{+0.167}_{-0.150}$	$2.465^{+0.278}_{-0.253}$
3.4	$90.1^{+4.7}_{-5.8}$	$1.330^{+0.295}_{-0.215}$	$1.82^{+0.24}_{-0.27}$	$0.569^{+0.021}_{-0.023}$	$2.202^{+0.206}_{-0.214}$	$2.592^{+0.283}_{-0.277}$
3.6	$79.4^{+10.0}_{-9.6}$	$1.010^{+0.360}_{-0.296}$	$1.74^{+0.28}_{-0.36}$	$0.512^{+0.022}_{-0.021}$	$1.160^{+0.394}_{-0.338}$	$1.704^{+0.602}_{-0.561}$
3.8	$79.4^{+8.4}_{-6.7}$	$1.029^{+0.287}_{-0.246}$	$1.74^{+0.29}_{-0.39}$	$0.433^{+0.025}_{-0.026}$	$1.320^{+0.355}_{-0.273}$	$1.548^{+0.441}_{-0.338}$
4.0	$72.3^{+7.6}_{-5.8}$	$0.863^{+0.271}_{-0.187}$	$1.42^{+0.37}_{-0.34}$	$0.387^{+0.017}_{-0.022}$	$0.942^{+0.288}_{-0.201}$	$1.090^{+0.340}_{-0.262}$
4.2	$77.0^{+3.6}_{-6.0}$	$0.905^{+0.122}_{-0.082}$	$1.73^{+0.33}_{-0.40}$	$0.355^{+0.025}_{-0.031}$	$1.051^{+0.087}_{-0.082}$	$1.246^{+0.118}_{-0.165}$
4.6	$73.7^{+4.9}_{-5.8}$	$0.910^{+0.119}_{-0.117}$	$1.54^{+0.37}_{-0.39}$	$0.278^{+0.023}_{-0.028}$	$0.966^{+0.126}_{-0.109}$	$1.037^{+0.153}_{-0.124}$
5.0	$57.3^{+4.0}_{-4.3}$	$0.535^{+0.117}_{-0.092}$	$1.54^{+0.31}_{-0.33}$	$0.159^{+0.018}_{-0.020}$	$0.555^{+0.119}_{-0.095}$	$0.580^{+0.122}_{-0.102}$
5.4	$54.4^{+4.3}_{-4.5}$	$0.597^{+0.152}_{-0.132}$	$1.55^{+0.29}_{-0.29}$	$0.060^{+0.009}_{-0.008}$	$0.551^{+0.138}_{-0.118}$	$0.613^{+0.158}_{-0.139}$

Appendix

**Table 6:** Fiducial Evolution of Thermal Parameters Assuming the Strong Prior on  $\bar{F}$

$z$	$\lambda_P$ [kpc]	$T_0$ [ $10^4$ K]	$\gamma$	$\bar{F}$	$T_{\Delta_{\text{power}}}$ [ $10^4$ K]	$T_{\Delta_{\star}}$ [ $10^4$ K]
1.8	$65.9^{+5.0}_{-4.2}$	$0.768^{+0.369}_{-0.218}$	$1.63^{+0.16}_{-0.25}$	$0.897^{+0.005}_{-0.005}$	$2.011^{+0.312}_{-0.278}$	$2.533^{+0.441}_{-0.384}$
2.0	$75.5^{+9.8}_{-6.4}$	$0.732^{+0.169}_{-0.091}$	$1.88^{+0.20}_{-0.27}$	$0.865^{+0.015}_{-0.019}$	$1.357^{+0.203}_{-0.151}$	$3.411^{+1.320}_{-0.832}$
2.2	$79.4^{+5.1}_{-5.0}$	$1.014^{+0.250}_{-0.150}$	$1.74^{+0.15}_{-0.21}$	$0.825^{+0.009}_{-0.008}$	$2.119^{+0.177}_{-0.153}$	$3.338^{+0.490}_{-0.443}$
2.4	$81.1^{+4.6}_{-4.7}$	$1.165^{+0.290}_{-0.189}$	$1.63^{+0.16}_{-0.19}$	$0.799^{+0.008}_{-0.008}$	$2.267^{+0.188}_{-0.165}$	$2.980^{+0.348}_{-0.297}$
2.6	$84.9^{+4.4}_{-4.8}$	$1.234^{+0.193}_{-0.139}$	$1.67^{+0.13}_{-0.15}$	$0.763^{+0.007}_{-0.007}$	$2.277^{+0.097}_{-0.092}$	$2.994^{+0.225}_{-0.207}$
2.8	$91.3^{+4.5}_{-5.3}$	$1.286^{+0.191}_{-0.147}$	$1.78^{+0.11}_{-0.12}$	$0.719^{+0.008}_{-0.008}$	$2.610^{+0.221}_{-0.195}$	$3.278^{+0.301}_{-0.267}$
3.0	$81.7^{+5.8}_{-5.9}$	$1.289^{+0.182}_{-0.144}$	$1.60^{+0.14}_{-0.16}$	$0.687^{+0.008}_{-0.008}$	$1.946^{+0.150}_{-0.136}$	$2.408^{+0.237}_{-0.209}$
3.2	$83.4^{+5.6}_{-5.3}$	$1.186^{+0.133}_{-0.115}$	$1.75^{+0.11}_{-0.13}$	$0.631^{+0.007}_{-0.008}$	$1.770^{+0.153}_{-0.138}$	$2.385^{+0.238}_{-0.222}$
3.4	$88.7^{+5.2}_{-5.3}$	$1.404^{+0.165}_{-0.157}$	$1.74^{+0.10}_{-0.11}$	$0.576^{+0.007}_{-0.007}$	$2.075^{+0.205}_{-0.209}$	$2.555^{+0.265}_{-0.270}$
3.6	$79.7^{+9.5}_{-10.7}$	$1.038^{+0.313}_{-0.267}$	$1.69^{+0.14}_{-0.25}$	$0.518^{+0.007}_{-0.007}$	$0.666^{+0.164}_{-0.139}$	$1.696^{+0.638}_{-0.608}$
3.8	$77.8^{+8.3}_{-6.9}$	$1.205^{+0.229}_{-0.194}$	$1.41^{+0.20}_{-0.23}$	$0.457^{+0.006}_{-0.006}$	$1.132^{+0.201}_{-0.179}$	$1.524^{+0.427}_{-0.328}$
4.0	$71.5^{+7.4}_{-5.2}$	$0.940^{+0.220}_{-0.173}$	$1.27^{+0.24}_{-0.24}$	$0.397^{+0.006}_{-0.006}$	$0.878^{+0.193}_{-0.154}$	$1.084^{+0.334}_{-0.256}$
4.2	$77.5^{+3.3}_{-5.4}$	$0.890^{+0.093}_{-0.073}$	$1.85^{+0.23}_{-0.33}$	$0.346^{+0.025}_{-0.022}$	$1.047^{+0.082}_{-0.079}$	$1.268^{+0.105}_{-0.146}$
4.6	$76.2^{+4.2}_{-5.4}$	$0.877^{+0.130}_{-0.106}$	$1.84^{+0.23}_{-0.33}$	$0.254^{+0.021}_{-0.020}$	$1.016^{+0.138}_{-0.112}$	$1.080^{+0.147}_{-0.124}$
5.0	$57.7^{+4.2}_{-4.3}$	$0.533^{+0.122}_{-0.091}$	$1.64^{+0.26}_{-0.32}$	$0.152^{+0.016}_{-0.017}$	$0.576^{+0.123}_{-0.099}$	$0.586^{+0.124}_{-0.102}$
5.4	$54.3^{+4.3}_{-4.6}$	$0.599^{+0.152}_{-0.134}$	$1.54^{+0.29}_{-0.29}$	$0.061^{+0.009}_{-0.008}$	$0.549^{+0.138}_{-0.117}$	$0.616^{+0.158}_{-0.140}$

# Acronyms

**BAL** broad absorption line.

**BAO** baryon acoustic oscillation.

**BOSS** Baryon Oscillation Spectroscopic Survey.

**CDM** cold dark matter.

**CMB** cosmic microwave background.

**COBE** Cosmic Background Explorer.

**COS** Cosmic Origins Spectrograph.

**DESI** Dark Energy Spectroscopic Instrument.

**DLA** damped Ly $\alpha$  absorption system.

**DM** dark matter.

**FGPA** fluctuating Gunn-Peterson absorption.

**FUV** far UV.

**GP** Gaussian process.

**GRB** gamma ray burst.

**HIRES** High Resolution Echelle Spectrometer.

**HST** Hubble Space Telescope.

**IGM** intergalactic medium.

**ISM** interstellar medium.

**JWST** James Webb Space Telescope.

**KODIAQ** Keck Observatory Database of Ionized Absorption toward Quasars.

**LLS** Lyman Limit System.

**LP** lifetime position.

## *Acronyms*

**LSF** line spread function.

**LUVOIR** Large Ultraviolet/Optical/Infrared Surveyor.

**Ly $\alpha$**  Lyman Alpha.

**MCMC** Markov Chain Monte Carlo.

**MW** Milky Way.

**PCA** principal component analysis.

**PDF** probability density function.

**pLLS** partial LLS.

**PPM** piecewise parabolic method.

**QSO** quasar.

**RSD** redshift space distortion.

**RT** radiative transfer.

**SDSS** Sloan Digital Sky Survey.

**SED** spectral energy distribution.

**STIS** Space Telescope Imaging Spectrograph.

**TDR** temperature density relation.

**THERMAL** Thermal History and Evolution in Reionization Models of Absorption Lines.

**UV** ultraviolet.

**UVB** ultraviolet background.

**UVES** Ultraviolet and Visual Echelle Spectrograph.

**VLT** Very Large Telescope.

**WDM** warm dark matter.

**WHIM** Warm-Hot Intergalactic Medium.

**WMAP** Wilkinson Microwave Anisotropy Probe.

# Own Publications

This is the full list of papers I am an author of. This includes submitted papers, co-authored papers, database entries, or in-preparation papers that are cited in the text. My name is highlighted for those works. This thesis is based on **Walther** et al. (2018a), **Walther** et al. (2018c), Khaire et al. (2018) and **Walther** et al. (2018b)

Hiss, H., **Walther, M.**, Hennawi, J. F., Oñorbe, J., O’Meara, J. M., & Rorai, A. (2018). *accepted for publication in Apj*, arXiv:1710.00700.

Khaire, V., **Walther, M.**, Hennawi, J. F., Oñorbe, J., Lukic, Z., Prochaska, J. X., Tripp, T. M., Burchett, J. N., & Rodriguez, C. (2018). *ArXiv e-prints*, arXiv:1808.05605.

Oñorbe, J., Hennawi, J. F., Lukić, Z., & **Walther, M.** (Sept. 2017a). *Apj* 847, 63, 63.

Rorai, A., Hennawi, J. F., Oñorbe, J., White, M., Prochaska, J. X., Kulkarni, G., **Walther, M.**, Lukić, Z., & Lee, K.-G. (Apr. 28, 2017b). *Science* 356.6336, 418–422.

**Walther, M.**, Hennawi, J. F., Hiss, H., Onorbe, J., Lee, K.-G., Rorai, A., & O’Meara, J. (Nov. 2017). *Zenodo Dataset* 1041022.

**Walther, M.**, Hennawi, J. F., Hiss, H., Oñorbe, J., Lee, K.-G., Rorai, A., & O’Meara, J. (Jan. 2018a). *Apj* 852.1, 22.

**Walther, M.**, Khaire, V., Hennawi, J. F., & Lukic, Z. (2018b). *in prep.*

**Walther, M.**, Oñorbe, J., Hennawi, J. F., & Lukić, Z. (Aug. 2018c). *submitted to Apj*, arXiv:1808.04367.



# All References

- Ali, Z. S., Parsons, A. R., Zheng, H., et al. (Aug. 2015). 809, 61, 61.
- Almgren, A. S., Bell, J. B., Lijewski, M. J., et al. (2013). *ApJ* 765.1, 39.
- Alpher, R. A., Bethe, H., & Gamow, G. (Apr. 1948). *Physical Review* 73, 803–804.
- Alpher, R. A., & Herman, R. (Nov. 1948). 162, 774–775.
- Ambikasaran, S., Foreman-Mackey, D., Greengard, L., et al. (Feb. 1, 2016). *TPAMI* 38.2, 252–265.
- Araya, I. J., & Padilla, N. D. (Nov. 2014). 445, 850–868.
- Armengaud, E., Palanque-Delabrouille, N., Yèche, C., et al. (2017). *arXiv preprint arXiv:1703.09126*.
- Bañados, E., Venemans, B. P., Mazzucchelli, C., et al. (Jan. 2018). 553, 473–476.
- Barkana, R., & Loeb, A. (July 2001). 349, 125–238.
- Baur, J., Palanque-Delabrouille, N., Yèche, C., et al. (Dec. 2017). *JCAP* 2017, 013, 013.
- Bautista, J. E., Busca, N. G., Guy, J., et al. (June 2017). 603, A12, A12.
- Becker, G. D., Bolton, J. S., Haehnelt, M. G., et al. (Jan. 2011). *MNRAS* 410, 1096–1112.
- Becker, G. D., Bolton, J. S., Madau, P., et al. (Jan. 22, 2015a). *MNRAS* 447.4, 3402–3419.
- Becker, G. D., Hewett, P. C., Worseck, G., et al. (Feb. 12, 2013). *MNRAS* 430.3, 2067–2081.
- Becker, G. D., & Bolton, J. S. (Jan. 12, 2013). *MNRAS* 436.2, 1023–1039.
- Becker, G. D., Bolton, J. S., & Lidz, A. (Oct. 12, 2015b).
- Bennett, C. L., Larson, D., Weiland, J. L., et al. (Oct. 2013). *The Astrophysical Journal Supplement Series* 208, 20, 20.
- Boera, E., Murphy, M. T., Becker, G. D., et al. (July 2014). *MNRAS* 441, 1916–1933.
- Boera, E., Murphy, M. T., Becker, G. D., et al. (Feb. 11, 2016). *MNRAS* 456.1, L79–L83.
- Bolton, J. S., Becker, G. D., Haehnelt, M. G., et al. (Mar. 2014). *MNRAS* 438, 2499–2507.
- Bolton, J. S., Viel, M., Kim, T.-S., et al. (May 2008). *MNRAS* 386, 1131–1144.
- Bolton, J. S., Becker, G. D., Wyithe, J. S. B., et al. (July 2010b). 406, 612–625.
- Bosman, S. E. I., Becker, G. D., Haehnelt, M. G., et al. (Sept. 2017). *MNRAS* 470, 1919–1934.

## All References

- Bosman, S. E. I., Fan, X., Jiang, L., et al. (Sept. 2018). 479, 1055–1076.
- Bouwens, R. J., Illingworth, G. D., Oesch, P. A., et al. (Apr. 13, 2015). *ApJ* 803.1, 34.
- Bowman, J. D., Rogers, A. E. E., Monsalve, R. A., et al. (Mar. 2018). 555, 67–70.
- Bryan, G. L., & Machacek, M. E. (2000). *ApJ* 534.1, 57.
- Carswell, R. F., & Webb, J. K. (Aug. 1, 2014). *Astrophysics Source Code Library*, ascl:1408.015.
- Cen, R., McDonald, P., Trac, H., et al. (Nov. 2009). *ApJL* 706, L164–L167.
- Cen, R., & Ostriker, J. P. (Mar. 1999). 514, 1–6.
- Chang, P., Broderick, A. E., & Pfrommer, C. (June 2012). 752, 23, 23.
- Clowe, D., Gonzalez, A., & Markevitch, M. (Apr. 2004). 604, 596–603.
- Compostella, M., Cantalupo, S., & Porciani, C. (Nov. 11, 2013). *MNRAS* 435.4, 3169–3190.
- Cooke, J., Sullivan, M., Gal-Yam, A., et al. (Nov. 2012). 491, 228–231.
- Croft, R. A. C. (Aug. 2004). 610, 642–662.
- Croft, R. A. C., Weinberg, D. H., Bolte, M., et al. (2002). *ApJ* 581, 20–52.
- Croft, R. A. C., Weinberg, D. H., Katz, N., et al. (Mar. 1, 1998). *ApJ* 495, 44.
- Croft, R. A., Weinberg, D. H., Pettini, M., et al. (1999). *ApJ* 520.1, 1.
- D’Aloisio, A., McQuinn, M., Davies, F. B., et al. (Nov. 8, 2016).
- D’Aloisio, A., McQuinn, M., Maupin, O., et al. (July 2018b). *ArXiv e-prints*, arXiv:1807.09282, arXiv:1807.09282.
- D’Odorico, V., Cristiani, S., Pomante, E., et al. (Dec. 2016). 463, 2690–2707.
- D’Aloisio, A., McQuinn, M., & Trac, H. (Nov. 6, 2015). *ApJ* 813.2, L38.
- Dall’Aglio, A., Wisotzki, L., & Worseck, G. (Nov. 2008). *A&A* 491.2, 465–481.
- Danforth, C. W., Keeney, B. A., Tilton, E. M., et al. (Feb. 2016). 817, 111, 111.
- Davé, R., Cen, R., Ostriker, J. P., et al. (2001). *ApJ* 552.2, 473.
- Davé, R., Oppenheimer, B. D., Katz, N., et al. (Nov. 2010). 408, 2051–2070.
- Davé, R., & Tripp, T. M. (June 2001). 553, 528–537.
- Davies, F. B., & Furlanetto, S. R. (Aug. 1, 2016). *MNRAS* 460.2, 1328–1339.
- Davies, F. B., Hennawi, J. F., Bañados, E., et al. (Feb. 2018a). *ArXiv e-prints*, arXiv:1802.06066, arXiv:1802.06066.
- Davies, F. B., Hennawi, J. F., Eilers, A.-. C., et al. (Mar. 2018b). 855, 106, 106.
- De Graaff, A., Cai, Y.-C., Heymans, C., et al. (Sept. 2017). *ArXiv e-prints*, arXiv:1709.10378, arXiv:1709.10378.

- De Jong, R. S., Barden, S. C., Bellido-Tirado, O., et al. (Aug. 2016). “4MOST: The 4-Metre Multi-Object Spectroscopic Telescope Project at Preliminary Design Review”. *Ground-Based and Airborne Instrumentation for Astronomy VI*. Vol. 9908, 99081O.
- Dekker, H., D’Odorico, S., Kaufer, A., et al. (2000). “Design, Construction, and Performance of UVES, the Echelle Spectrograph for the UT2 Kueyen Telescope at the ESO Paranal Observatory”. *Astronomical Telescopes and Instrumentation*. Proc. SPIE. International Society for Optics and Photonics, 534–545.
- DESI Collaboration, Aghamousa, A., Aguilar, J., et al. (Oct. 2016). *ArXiv e-prints*, arXiv:1611.00036, arXiv:1611.00036.
- Dijkstra, M. (Apr. 2017). “Saas-Fee Lecture Notes: Physics of Lyman Alpha Radiative Transfer”. *ArXiv E-Prints*, arXiv:1704.03416.
- Draine, B. T. (2011). *Physics of the Interstellar and Intergalactic Medium*. Princeton University Press.
- Eilers, A.-C., Davies, F. B., & Hennawi, J. F. (July 2018). *submitted to ApJ*, arXiv:1807.04229, arXiv:1807.04229.
- Fan, X., Strauss, M. A., Becker, R. H., et al. (2006a). *ApJ* 132.1, 117.  
– (July 2006b). 132, 117–136.
- Faucher-Giguère, C.-A., Lidz, A., Hernquist, L., et al. (Nov. 1, 2008a). *ApJ* 688, 85–107.
- Faucher-Giguère, C.-A., Lidz, A., Zaldarriaga, M., et al. (Oct. 2009). 703, 1416–1443.
- Faucher-Giguère, C.-A., Prochaska, J. X., Lidz, A., et al. (July 1, 2008b). *ApJ* 681, 831–855.
- Finkelstein, S. L., Ryan Russell E., J., Papovich, C., et al. (Sept. 2015). 810, 71, 71.
- Font-Ribera, A., Kirkby, D., Busca, N., et al. (May 2014). *Journal of Cosmology and Astro-Particle Physics* 2014, 027, 027.
- Foreman-Mackey, D., Hogg, D. W., Lang, D., et al. (2013). *PASP* 125.925, 306.
- Friedmann, A. (Jan. 1922). *Zeitschrift fur Physik* 10, 377–386.
- Fumagalli, M., Haardt, F., Theuns, T., et al. (June 1, 2017). *Mon Not R Astron Soc* 467.4, 4802–4816.
- Fumagalli, M., O’Meara, J. M., Prochaska, J. X., et al. (Oct. 2010). 408, 362–382.
- Furlanetto, S. R., & Oh, S. P. (2008). *ApJ* 681.1, 1.
- Gaikwad, P., Khaire, V., Choudhury, T. R., et al. (2017a). *MNRAS*, stw3086.
- Gaikwad, P., Srianand, R., Choudhury, T. R., et al. (May 2017b). 467, 3172–3187.
- Garzilli, A., Bolton, J. S., Kim, T.-S., et al. (Aug. 2012). *MNRAS* 424, 1723–1736.

## All References

- Garzilli, A., Boyarsky, A., & Ruchayskiy, O. (Oct. 2017). *Physics Letters B* 773, 258–264.
- Giallongo, E., Grazian, A., Fiore, F., et al. (June 2015). *A&A* 578, A83.
- Gnedin, N. Y., & Hui, L. (May 1998). *MNRAS* 296, 44–55.
- Gnedin, N. Y. (Sept. 2014). 793, 29, 29.
- Gnedin, N. Y., Baker, E. J., Bethell, T. J., et al. (2003). *ApJ* 583.2, 525.
- Goodman, J., & Weare, J. (Jan. 31, 2010). *CAMCoS* 5.1, 65–80.
- Greig, B., Bolton, J. S., & Wyithe, J. S. B. (Mar. 2015). 447, 2503–2511.
- Gunn, J. E., & Peterson, B. A. (Nov. 1965). *ApJ* 142, 1633–1641.
- Haardt, F., & Madau, P. (Feb. 20, 2012). *ApJ* 746.2, 125.
- Habib, S., Heitmann, K., Higdon, D., et al. (Oct. 2007). *Phys. Rev. D* 76.8.
- Haehnelt, M. G., & Steinmetz, M. (1998). *MNRAS* 298.1, L21–L24.
- Heitmann, K., Higdon, D., Nakhleh, C., et al. (2006). *ApJL* 646.1, L1.
- Heitmann, K., Higdon, D., White, M., et al. (Nov. 1, 2009). *ApJ* 705.1, 156–174.
- Heitmann, K., Lawrence, E., Kwan, J., et al. (Dec. 13, 2013). *ApJ* 780.1, 111.
- Hills, R., Kulkarni, G., Meerburg, P. D., et al. (May 2018). *ArXiv e-prints*, arXiv:1805.01421, arXiv:1805.01421.
- Hinshaw, G., Larson, D., Komatsu, E., et al. (Oct. 1, 2013). *ApJS* 208.2, 19.
- Hiss, H., **Walther, M.**, Hennawi, J. F., Oñorbe, J., O’Meara, J. M., & Rorai, A. (2018). *accepted for publication in ApJ*, arXiv:1710.00700.
- Hogg, D. W. (May 10, 1999).
- Hubble, E. (Mar. 1929). *Proceedings of the National Academy of Science* 15, 168–173.
- Hui, L., & Gnedin, N. Y. (Nov. 1997). *MNRAS* 292, 27–+.
- Hui, L., & Haiman, Z. (Oct. 1, 2003). *ApJ* 596, 9–18.
- Hui, L., Ostriker, J. P., Tremaine, S., et al. (Feb. 28, 2017). *Physical Review D* 95.4.
- Iršič, V., Viel, M., Berg, T. A. M., et al. (Apr. 2017a). *MNRAS* 466, 4332–4345.
- Iršič, V., Viel, M., Haehnelt, M. G., et al. (July 2017b). *Phys. Rev. D* 96.2, 023522, 023522.
- Iršič, V., & Viel, M. (Dec. 11, 2014). *JCAP* 2014.12, 024–024.
- Iršič, V., Viel, M., Haehnelt, M. G., et al. (2017c). *arXiv preprint arXiv:1703.04683*.
- Jakobsen, P., Boksenberg, A., Deharveng, J. M., et al. (July 1994). 370, 35–39.
- Jones, E., Oliphant, T., Peterson, P., et al. (2001–).
- Katz, N., Hernquist, L., & Weinberg, D. H. (Nov. 1992). *ApJL* 399, L109–L112.

- Khaire, V., & Srianand, R. (July 2015). 451, L30–L34.  
 – (Jan. 2018). *ArXiv e-prints*.
- Khaire, V., Srianand, R., Choudhury, T. R., et al. (Oct. 15, 2015).
- Khaire, V., **Walther, M.**, Hennawi, J. F., Oñorbe, J., Lukic, Z., Prochaska, J. X., Tripp, T. M., Burchett, J. N., & Rodriguez, C. (2018). *ArXiv e-prints*, arXiv:1808.05605.
- Kim, T.-S., Viel, M., Haehnelt, M. G., et al. (Jan. 2004). *MNRAS* 347, 355–366.
- Kirkman, D., Tytler, D., Lubin, D., et al. (Apr. 11, 2007). *MNRAS* 376.3, 1227–1237.
- Kirkman, D., Tytler, D., Suzuki, N., et al. (July 1, 2005). *MNRAS* 360, 1373–1380.
- Kohn, S., Chichura, P. M., Igarashi, A. S., et al. (Feb. 2018). *ArXiv e-prints*, arXiv:1802.04151, arXiv:1802.04151.
- Kollmeier, J. A., Weinberg, D. H., Oppenheimer, B. D., et al. (July 2014). 789, L32, L32.
- Kulkarni, G., Hennawi, J. F., Oñorbe, J., et al. (Oct. 6, 2015). *ApJ* 812.1, 30.
- Lee, K.-G., Suzuki, N., & Spergel, D. N. (Feb. 2012). *AJ* 143, 51.
- Lee, K.-G., Hennawi, J. F., Spergel, D. N., et al. (Jan. 29, 2015). *ApJ* 799.2, 196.
- Lee, K.-G., Hennawi, J. F., Stark, C., et al. (Nov. 2014). 795, L12, L12.
- Lehner, N., O’Meara, J. M., Fox, A. J., et al. (May 29, 2014). *ApJ* 788.2, 119.
- Lemaître, G. (Jan. 1927). *Annales de la Société Scientifique de Bruxelles* 47, 49–59.
- Lidz, A., Heitmann, K., Hui, L., et al. (Feb. 2006). *ApJ* 638, 27–44.
- Lidz, A., Faucher-Giguère, C.-A., Dall’Aglia, A., et al. (July 1, 2010). *ApJ* 718, 199–230.
- Lomb, N. R. (1976). *Ap&SS* 39.2, 447–462.
- López, S., D’Odorico, V., Ellison, S. L., et al. (Oct. 2016). *A&A* 594, A91.
- Lukić, Z., Stark, C. W., Nugent, P., et al. (2015). *MNRAS* 446.4, 3697–3724.
- Lynds, R. (Mar. 1971). *ApJL* 164, L73.
- Madau, P., & Haardt, F. (Nov. 2015). *ApJL* 813, L8.
- Mason, C. A., Trenti, M., & Treu, T. (Nov. 2015). 813, 21, 21.
- Mason, C. A., Treu, T., Dijkstra, M., et al. (Mar. 2018). 856, 2, 2.
- McDonald, P., Miralda-Escudé, J., Rauch, M., et al. (Nov. 2001). *ApJ* 562, 52–75.
- McDonald, P., Seljak, U., Cen, R., et al. (July 2005a). *MNRAS* 360, 1471–1482.
- McDonald, P., Miralda-Escudé, J., Rauch, M., et al. (Nov. 2000). *ApJ* 543, 1–23.
- McDonald, P., Seljak, U., Burles, S., et al. (2006). *ApJS* 163, 80–109.
- McQuinn, M., Lidz, A., Zaldarriaga, M., et al. (Apr. 2009). *ApJ* 694, 842–866.

## All References

- McQuinn, M., & Upton Sanderbeck, P. R. (Feb. 2016). *MNRAS* 456, 47–54.
- Meiksin, A., & White, M. (June 1, 2001). *MNRAS* 324, 141–148.
- Mesinger, A., ed. (Jan. 2016). *Understanding the Epoch of Cosmic Reionization*. Vol. 423.
- Mesinger, A., & Furlanetto, S. (Nov. 2007). 669, 663–675.
- Modigliani, A., Bramich, D., Vernet, J., et al. (May 31, 2017). *X-Shooter Pipeline User Manual Issue 12.15*.
- Nelder, J. A., & Mead, R. (1965). *The Computer Journal* 7.4, 308–313.
- Nicastro, F., Kaastra, J., Krongold, Y., et al. (June 2018). 558, 406–409.
- O’Meara, J. M., Lehner, N., Howk, J. C., et al. (July 2017). *ArXiv e-prints*.
- O’Meara, J. M., Lehner, N., Howk, J. C., et al. (Sept. 14, 2015). *AJ* 150.4, 111.
- Ocvirk, P., Gillet, N., Shapiro, P. R., et al. (Dec. 2016). 463, 1462–1485.
- Oesch, P. A., Bouwens, R. J., Illingworth, G. D., et al. (Apr. 24, 2014). *ApJ* 786.2, 108.
- Oesch, P. A., Brammer, G., van Dokkum, P. G., et al. (Mar. 2016). 819, 129, 129.
- Oñorbe, J., Hennawi, J. F., Lukić, Z., & **Walther, M.** (Sept. 2017a). *ApJ* 847, 63, 63.
- Oñorbe, J., Davies, F. B., Hennawi, J. F., et al. (2018a).
- Oñorbe, J., Hennawi, J. F., & Lukić, Z. (Mar. 8, 2017b). *ApJ* 837.2, 106.
- Onoue, M., Kashikawa, N., Willott, C. J., et al. (Oct. 2017). 847, L15, L15.
- Palanque-Delabrouille, N., Yèche, C., Borde, A., et al. (Nov. 2013). *A&A* 559, A85.
- Palanque-Delabrouille, N., Yèche, C., Baur, J., et al. (Nov. 6, 2015). *JCAP* 2015.11, 011–011.
- Parsa, S., Dunlop, J. S., & McLure, R. J. (Mar. 2018). 474, 2904–2923.
- Peebles, M. S., Weinberg, D. H., Davé, R., et al. (May 2010b). 404, 1281–1294.
- Penzias, A. A., & Wilson, R. W. (July 1965). 142, 419–421.
- Perlmutter, S., Aldering, G., della Valle, M., et al. (Jan. 1998). 391, 51–54.
- Pieri, M. M., Bonoli, S., Chaves-Montero, J., et al. (Dec. 2016). “WEAVE-QSO: A Massive Inter-galactic Medium Survey for the William Herschel Telescope”. *SF2A-2016: Proceedings of the Annual Meeting of the French Society of Astronomy and Astrophysics*, 259–266.
- Planck Collaboration, Adam, R., Aghanim, N., et al. (Dec. 2016a). *A&A* 596, A108.
- Planck Collaboration, Ade, P. A. R., Aghanim, N., et al. (Nov. 2014). *A&A* 571. Ed. by J. Tauber, A16.
- Planck Collaboration, Ade, P. A. R., Aghanim, N., et al. (Oct. 2016b). *A&A* 594, A13.
- Planck Collaboration, Akrami, Y., Arroja, F., et al. (July 1, 2018). *ArXiv e-prints* 1807, arXiv:1807.06205.

## All References

- Pritchard, J. R., & Loeb, A. (Aug. 2012). *Reports on Progress in Physics* 75, 086901, 086901.
- Prochaska, J. X. (Apr. 2017). *Astronomy and Computing* 19, 27–33.
- Puchwein, E., Bolton, J. S., Haehnelt, M. G., et al. (July 2015). *MNRAS* 450, 4081–4097.
- Puchwein, E., Haardt, F., Haehnelt, M. G., et al. (Jan. 2018). *ArXiv e-prints*.
- Puchwein, E., Pfrommer, C., Springel, V., et al. (June 2012). *MNRAS* 423, 149–164.
- Rasmussen, C. E., & Williams, C. K. I. (2005). *Gaussian Processes for Machine Learning (Adaptive Computation and Machine Learning)*. The MIT Press.
- Ricotti, M., Gnedin, N. Y., & Shull, J. M. (May 2000). *ApJ* 534, 41–56.
- Riess, A. G., Filippenko, A. V., Challis, P., et al. (Sept. 1998). 116, 1009–1038.
- Roberge, A., & Moustakas, L. A. (Aug. 2018). *Nature Astronomy* 2, 605–607.
- Robertson, B. E., Furlanetto, S. R., Schneider, E., et al. (May 2013). 768, 71, 71.
- Rorai, A., Becker, G. D., Haehnelt, M. G., et al. (Apr. 21, 2017a). *MNRAS* 466.3, 2690–2709.
- Rorai, A., Carswell, R. F., Haehnelt, M. G., et al. (Mar. 2018). 474, 2871–2883.
- Rorai, A., Hennawi, J. F., Oñorbe, J., White, M., Prochaska, J. X., Kulkarni, G., **Walther, M.**, Lukić, Z., & Lee, K.-G. (Apr. 28, 2017b). *Science* 356.6336, 418–422.
- Rorai, A., Hennawi, J. F., & White, M. (Oct. 1, 2013). *ApJ* 775.2, 81.
- Rossi, G. (Nov. 2017). 233, 12, 12.
- Rubin, V. C., & Ford W. Kent, J. (Feb. 1970). 159, 379.
- Rudie, G. C., Steidel, C. C., & Pettini, M. (Oct. 2012). *ApJL* 757, L30.
- Scargle, J. D. (1982). *ApJ* 263, 835–853.
- Schaye, J., Theuns, T., Rauch, M., et al. (Nov. 2000). *MNRAS* 318, 817–826.
- Schmidt, B. P., Suntzeff, N. B., Phillips, M. M., et al. (Nov. 1998). 507, 46–63.
- Selsing, J., Malesani, D., Goldoni, P., et al. (Feb. 2018). *ArXiv e-prints*.
- Shull, J. M., Moloney, J., Danforth, C. W., et al. (Sept. 2015). 811, 3, 3.
- Shull, J. M., Smith, B. D., & Danforth, C. W. (Nov. 2012). 759, 23, 23.
- Smoot, G. F., Bennett, C. L., Kogut, A., et al. (Sept. 1992). 396, L1.
- Sorini, D., Oñorbe, J., Lukić, Z., et al. (Aug. 11, 2016). *ApJ* 827.2, 97.
- Stanway, E. R., Eldridge, J. J., & Becker, G. D. (Feb. 11, 2016). *MNRAS* 456.1, 485–499.
- Suarez, T., & Pontzen, A. (2017). *arXiv preprint arXiv:1706.02716*.
- Tanimura, H., Hinshaw, G., McCarthy, I. G., et al. (Sept. 2017). *ArXiv e-prints*, arXiv:1709.05024, arXiv:1709.05024.

## All References

- Theuns, T., Zaroubi, S., Kim, T.-S., et al. (May 2002). *MNRAS* 332, 367–382.
- Topping, M. W., & Shull, J. M. (Feb. 17, 2015). *ApJ* 800.2, 97.
- Upton Sanderbeck, P. R., D’Aloisio, A., & McQuinn, M. J. (Aug. 1, 2016). *MNRAS* 460.2, 1885–1897.
- Viel, M., Becker, G. D., Bolton, J. S., et al. (Jan. 29, 2008). *Phys. Rev. Lett.* 100.4.
- Viel, M., Becker, G. D., Bolton, J. S., et al. (Aug. 5, 2013b). *Phys. Rev. D* 88.4.
- Viel, M., Bolton, J. S., & Haehnelt, M. G. (Oct. 11, 2009). *MNRAS* 399.1, L39–L43.
- Vogt, S. S., Allen, S. L., Bigelow, B. C., et al. (1994). “HIRES: The High-Resolution Echelle Spectrometer on the Keck 10-m Telescope”. *1994 Symposium on Astronomical Telescopes & Instrumentation for the 21st Century*. Proc. SPIE. International Society for Optics and Photonics, 362–375.
- Walther, M.**, Hennawi, J. F., Hiss, H., Onorbe, J., Lee, K.-G., Rorai, A., & O’Meara, J. (Nov. 2017). *Zenodo Dataset* 1041022.
- Walther, M.**, Hennawi, J. F., Hiss, H., Oñorbe, J., Lee, K.-G., Rorai, A., & O’Meara, J. (Jan. 2018a). *ApJ* 852.1, 22.
- Walther, M.**, Khaire, V., Hennawi, J. F., & Lukic, Z. (2018b). *in prep.*
- Walther, M.**, Oñorbe, J., Hennawi, J. F., & Lukić, Z. (Aug. 2018c). *submitted to ApJ*, arXiv:1808.04367.
- White, M. (Dec. 2002). *ApJS* 143, 241–255.
- Worseck, G., Prochaska, J. X., McQuinn, M., et al. (June 2011). *ApJL* 733, L24.
- Worseck, G., Davies, F. B., Hennawi, J. F., et al. (2018). *submitted to ApJ*, arXiv:1808.05247.
- Worseck, G., & Prochaska, J. X. (Feb. 10, 2011). *ApJ* 728.1, 23.
- Worseck, G., Prochaska, J. X., Hennawi, J. F., et al. (July 13, 2016). *ApJ* 825.2, 144.
- Yèche, C., Palanque-Delabrouille, N., Baur, J., et al. (June 2017). *JCAP* 2017, 047, 047.
- Zaldarriaga, M., Hui, L., & Tegmark, M. (2001). *ApJ* 557.2, 519.
- Zhu, C., Byrd, R. H., Lu, P., et al. (Dec. 1997). *ACM Trans. Math. Softw.* 23.4, 550–560.
- Zwicky, F. (Jan. 1933). *Helvetica Physica Acta* 6, 110–127.